Structural Behaviour and Failure Analysis of CNT Reinforced Composite Plates in Hygro-Thermal Environment

Thesis

Submitted for the partial fulfilment of requirements of Degree

of

Doctor of Philosophy

By

Lalit Kumar Sharma
(Regd. No: 901708002)

Under the guidance of

Dr. Neeraj Grover
Associate Professor
MED, TIET
Patiala

Dr. Gagandeep Bhardwaj
Associate Professor
MED, TIET
Patiala

THAPAR INSTITUTE
OF ENGINEERING & TECHNOLOGY
(Deemed to be University)

Mechanical Engineering Department
Thapar Institute of Engineering & Technology
Patiala, Punjab, India
February 2023

Dedicated To….

… My Family

&

My Beautiful Little

Daughter

Vedanshi Sharma

Certificate

This is certify that the thesis titled "**Structural Behaviour and Failure Analysis of CNT Reinforced Composite Plates in Hygro-Thermal Environment**" being submitted by Mr. Lalit Kumar Sharma to the Department of Mechanical Engineering, Thapar Institute of Engineering and Technology (Deemed to be University), Patiala for the award of degree of Doctor of Philosophy, is a record of bona fide research work carried out by him under our guidance and supervision and has fulfilled the requirements for the submission of this thesis, which to our knowledge has reached the requisite standard.

The results embodied in the thesis have not been submitted in part or full to any other University or Institute for the award of any degree or diploma.

N Grover 22/9/23.

Dr. Neeraj Grover
Associate Professor
Department of Mechanical Engineering
Thapar Institute of Engineering &
Technology (Deemed to be University)
Patiala, India

22/09/2023

Dr. Gagandeep Bhardwaj
Associate Professor
Department of Mechanical Engineering
Thapar Institute of Engineering &
Technology (Deemed to be University)
Patiala, India

Acknowledgement

I would like to express my sincere gratitude to my supervisor, Dr. Neeraj Grover, Associate Professor and Dr. Gagandeep Bhardwaj, Associate Professor, Department of Mechanical Engineering, Thapar Institute of Engineering & Technology (Deemed to be University), for their guidance, patience, and unwavering support throughout my research journey. Their valuable insights and feedback have significantly contributed to shaping this work and making it possible. I have greatly benefited from their expertise and mentorship, and my association with them throughout this research project has been an enriching and rewarding experience. It has been a great honour to work under their guidance.

I am extremely thankful to Prof. Padmakumar Nair, Director, Thapar Institute of Engineering & Technology (Deemed to be University), Prof. R. Siddique, Dean of Research & Sponsored Projects, Thapar Institute of Engineering & Technology (Deemed to be University) and Dr. T. K. Bera, Head, Department of Mechanical Engineering, Thapar Institute of Engineering & Technology (Deemed to be University) for extending the opportunity to undertake this doctoral research.

I would like to profoundly thank my doctoral committee members, Dr. Kishore Khanna and Dr. J.S Saini, Department of Mechanical Engineering and Dr. Shruti Sharma, Department of Civil Engineering, Thapar Institute of Engineering & Technology (Deemed to be University) for their immense help and guiding me towards the right direction.

My heartfelt appreciation goes out to my family whose unwavering support and patience have been instrumental in making this accomplishment a reality. I am indebted to my mother-in-law, parents, and other family members for their blessings, good wishes, and constant encouragement throughout my research. My sincere thanks to my beloved wife, Anju Sharma, for his exceptional love, understanding, and unwavering support. I am grateful for his continuous assistance, which has been invaluable in achieving this milestone in my life. Without his constant support and cooperation, this study would not have been possible.

I consider myself fortunate to have a supportive group of friends who have provided me with constant encouragement, motivation, and positivity in every situation. I express my gratitude to Mr. Yadwinder Singh Joshan, Dr. Nirmal Singh and Mr. Manu Dev Sharma for their unwavering support and motivation throughout this journey.

I gratefully acknowledge the financial support given by Department of Science and Technology – Science and Engineering Research Board (Sanction order nos. ECR/2016/000459) and institute scholarship.

Finally, I would like to thank all those who have contributed in ways both large and small to the completion of this thesis. From the staff at the library who helped me to locate resources, to the colleagues who offered support and encouragement along the way, I am grateful for the many contributions that have made this work possible.

Lalit Sharma..
22/09/23
Lalit Kumar Sharma

Abstract

The present work deals with the formulation of inverse hyperbolic shear deformation theory (IHSDT) for modeling and analysis of carbon nanotube (CNT) reinforced plates. The theory is developed in the framework of non-polynomial shear strain function in term of shear deformation theory. The displacement field is chosen in such a way that it satisfies the zero transverse shear stress conditions at the top and bottom of the plate in thickness direction and does not require a shear correction factor. The effect of in-plane shear deformation in the displacements is defined using the shear strain shape function in terms of inverse hyperbolic function. The structural response of CNT reinforced plates is examined under the action of mechanical, thermal and moisture conditions. Firstly, the effective material properties are assumed to be temperature dependent and estimated according to the extended rule of mixture. Four types of distributions such as uniformly distributed (UD) and functionally graded (FG-V, FG-O and FG-X) are considered to reinforce the CNT in the matrix material (PmPV and PMMA). The structural responses are computed in analytical form as well as in the numerical so as to enhance the generality of the developed methodology. The closed form solutions are computed for structural response (bending, buckling and free vibration) of simply supported CNT reinforced plates using Navier approach. The validation of obtained results are demonstrated successfully by comparing with the other existing methodologies available in the literature. Further, to enhance the applicability, a C^0 continuous eight noded isoparametric serendipity finite element methodology is developed using IHSDT. The developed finite element methodology is implemented to examine the static, buckling and free vibration behavior of temperature dependent CNT reinforced plates. The influence of the various parameters (volume fraction, span to thickness ratio, aspect ratio, distribution of CNT and boundary conditions) on non-dimensional central deflection, buckling load parameter and fundamental frequency are investigated in different temperature conditions. Furthermore, in order to consider the effect of hygro-thermo-mechanical conditions on the response of CNT reinforced plate, the Navier type and C^0 finite element methodologies are developed. The validation of obtained results is presented by comparing the Navier type closed form solution with the numerical FE solution and it is concluded that the percentage between the closed form solution (CFS) and FE solution is ranging between 0.3-1 % for simply supported boundary conditions (SSSS). The new results are presented for dimensional central deflection of CNT reinforced plate subject to uniformly distributed linear and non-linear temperature and moisture environment. The influence of various parameters such as volume fraction, span to thickness ratio, distribution of CNT and boundary conditions on the dimensional central deflection are examined for CNT reinforced plates in the hygro-thermal environment. Finally, the emphasis has been focused to examine the effect of presence of the crack in FG-CNT reinforced plate using the extended finite element method on the static response. A C^0 continuous eight noded serendipity quadrilateral element with Heaviside function and crack tip enrichment function are used to model the domain and the discontinuity in the CNT reinforced plate. The influence of various parameters such as crack length, volume fraction, span to thickness ratio and boundary condition on the non-dimensional central deflection are also assessed.

Keywords: Carbon nanotube reinforced plate, functionally graded carbon nanotube reinforced plate, shear strain shape function, extended rule of mixture, inverse hyperbolic shear deformation theory, static, buckling, free vibration, hygro-thermo-mechanical, Navier solution, finite element method, extended finite element method, surface crack.

Contents

List of Symbols

a,b : Plate Dimension

h : Total Thickness of the Plate

x, y, z : Cartesian Co-ordinates

η_1, η_2, η_3 : CNT Efficiency Parameters

V_{CNT} : Volume Fraction of CNT

w_{CNT} : Mass Fraction of CNT

ρ_{CNT} : Density of CNT

ρ_m : Density of Matrix Phase

α : Coefficient of Thermal Expansion

β : Coefficient of Hygroscopic Expension

$f(z)$: Shear Strain Shape Function

u, v, w : Displacements in x, y, z direction respectively

u_0, v_0, w_0 : Mid-plane displacements in x, y, z direction respectively

θ_x, θ_y : Mid-plane Rotation about x and y-axis respectively

$\{\sigma\}$: Stress Vector

$\{\varepsilon\}$: Strain Vector

$\{\varepsilon_L\}$: Linear Strain Vector

$\{\varepsilon_{NL}\}$: Non Linear Strain Vector

$[Q]$: Reduced Stiffness Matrix

$\{\varepsilon^{Th}\}$: Thermal Induced Strain Vector

$\{\varepsilon^H\}$: Moisture Induced Strain Vector

E_{11} : Young’s Modulus in Longitudinal Direction

E_{22} : Young’s Modulus in Transverse Direction

G_{12} : In-Plane Shear Modulus

G_{13}, G_{23} : Transverse Shear Modulus

ν_{12}, ν_{21} : Longitudinal and Transverse Poisson's Ratio

ΔT : Change in Temperature

Δc : Change in Moisture Concentration

T, U, V : Kinetic Energy, Strain Energy and Work Done

Δ : Variational Operator

N_{xx}, N_{yy}, N_{xy} : Resultant In-Plane Stresses

M_{xx}, M_{yy}, M_{xy} : Resultant In-plane Moments

P_{xx}, P_{yy}, P_{xy} : Resultant Higher Order Moments

Q_1, Q_2 : Resultant Transverse Shear Stresses

K_1, K_2 : Resultant Transverse Moments

I_i (i = 0 to 5) : Inertial Resultants

$[R]$: Elastic Stiffness Matrix

$[G]$: Geometrical Stiffness Matrix

$[M]$: Mass Matrix

$\{\Delta\}$: Vector Containing Field Variables

φ_x, φ_y : Artificial Degree of Freedom

N_i : Shape Function Corresponding to i^{th} Node

ξ, η : Natural Co-ordinates

$[H]$: Transformation Matrix

$\{\bar{\varepsilon}_l\}$: Generalized Strain Vector

$[L]$: Operator Matrix

U_L : Total Strain Energy Due to Linear Strains

U_{NL} : Total Non-linear Strain Energy Due to Non-linear Strains

U_c : Total Strain Energy Due to Artificial Constraints

$[K]$: Global Elastic Stiffness Matrix

$[K_G]$: Global Geometrical Stiffness Matrix

$[K_c]$: Artificial Stiffness Matrix

W : Total Work Done

F_m : Load Vector Due to External forces

F_{th} : Load Vector Due to Thermal Load

F_c : Load Vector Due to Moisture Change

λ : Buckling Parameter

ω : Frequency Parameter

γ : Penalty Parameter

List of Figures

List of Tables

Abbreviation

CNT : Carbon Nanotube
CNTRC : Carbon Nanotube Reinforced Composite
SWCNT : Single Walled Carbon Nanotube
MWCNT : Multi Walled Carbon Nanotube
FG : Functionally Graded
3D : Three-Dimension
2D : Two-Dimension
ESL : Equivalent Single Layer
ZZ : Zig-Zag
LW : Layerwise
CLPT : Classical Laminated Plate Theory
FSDT : First Order Shear Deformation Theory
HSDT : Higher Order Shear Deformation Theory
FEM : Finite Element Method
XFEM : Extended Finite Element Method
IGA : Isogeometric Analysis
IHSDT : Inverse Hyperbolic Shear Deformation Theory
FG-CNT : Functionally Graded Carbon Nanotube
SSSS : All Edges Simply Supported
CCCC : All Edges Clamped
SSL : Sinusoidal Load
UDL : Uniformly Distributed Load
PMMA : Poly [methyl methacrylate]
PmPV : Poly [(m-phenylene-vinylene)-co-(2,5-dioctoxy-p-phenylenevinylen)]

Chapter 1 INTRODUCTION

1.1. Overview

In this chapter, the concise elucidation of the realms concerning the current research work is presented. Firstly, a motivation supporting the basis of the current research work is presented highlighting the necessity of modeling and analysis of carbon-nano tubes (CNT) reinforced structures. The subsequent sections provide the definition and classification of composite materials and structures, CNT reinforced structures and their application, crack induced failure of such structures, effect of hygro-thermal environment, modelling approaches, solution methodologies, and brief description of structural and hygro-thermal analysis. Further, the aim of the present research work is defined followed by the details of organization of the thesis. The chapter is also summarized in the last section.

1.2. Motivation

The advancement in science and technology, demand for superior infrastructure, need of efficient and lightweight structures, etc. necessitates the development of potential materials for the improved performance of the materials, components, structures, or a system involved. The mankind, in terms of materials, has evolved from stone age (10000 BC) to the age of molecular engineering (currently) following consequential period of bronze age (5000 BC), iron age (1000), age of steel (1900), age of polymers (1960), and age of silicon (1990) [1]. The rate of change for the material development is fast in last three decades than at any other period in the past. The need of high-strength, high-stiffness, lightweight materials, and possessing tailor made attributes (e.g. mechanical properties, thermal properties, electrical properties, etc.) in various sectors in particular aviation, automobile, civil infrastructure, biomedical, energy harvesting, sports equipment, defense, spacecraft, machines and tools, has contributed significantly towards this increment in rate of development of new materials for components and structures. One such advancement is seen in terms of composite materials due to the fact that they exhibit the required attributes. The performance of the composite material depends significantly on its reinforcement and on the basis of type of reinforcement and matrix, the advanced composites have been developed in the past. The fact that the attributes of CNT such as Young's modulus and shear modulus being comparable to diamond make it potential material for utilization in advanced materials and structures [2]. Furthermore, the nanotube parameters e.g., helicity, tube radius don't influence these attributes significantly [3]. The theoretical strength of CNT is about 110 times higher than that of the steel due to which it is one of the strongest material. It is noted that the strength of the composite materials depends significantly on the embedded fiber strength. With the promising properties of the CNT, the same is chosen as a filler material in the matrix material and due to the same, the scientific community conducted theoretical-studies/experiments in this domain, and using them as a reinforcement material in conventional material.

Further, with the knowledge and development of new materials and structures, CNT reinforced composites (CNTRC) are potential materials to be extensively preferred as structural members. Due to the fact that these material differ significantly from the conventional monolithic materials, it becomes important to model and analyze such materials and structures to accurately predict their response. Therefore, it is mandatory to develop an explicit mathematical model for accurate prediction of the structural behavior of CNT reinforced structures. Structural response (i.e. bending, buckling and free vibration) belongs to the analysis of the CNTRC structures corresponding to the mechanical loading. Also, the environmental parameters such as temperature change and moisture change further affect the response of the structures. The interaction of the CNTRC structure with moisture and temperature will lead to a change in the material properties of the CNT reinforced structure and hence affects the overall response of the structure in presence of hygro-thermal loads. Due to application of load in service conditions, manufacturing defect or operating conditions, these materials are prone to crack. To ensure the reliability and accurate prediction of behavior of the CNT reinforced composite structures, it become mandatory to consider the response of structure in the presence of a crack. It is important to model the CNT reinforced composite plate with a crack under loading and examine the structural response. Thus, in the viewpoint of above discussions, the modelling and analysis of CNTRC with or without the presence of crack in presence of hygro-thermal environment is an impending problem and stands as motivation to the current work.

1.3. Composite Structures

The monolithic metals and alloys cannot always meet the requirements (specific strength, specific stiffness, etc.) of advanced structural applications. Therefore, a new material is obtained by combining two or more materials at the macroscopic level which have enhanced properties relative to the conventional material such as high-strength, high-stiffness, tailor-made materials while being light in weight generally owing to low-density continuous phase and is termed as composite material. The composite materials are defined as the materials having strong reinforcements (continuous or non-continuous) surrounded by a weaker matrix (continuous) material. The matrix material may be ceramic, metallic or polymer-based depending upon the concerned application while the reinforcement may be of particles, whiskers, or continuous fibers. Depending upon the matrix and embedded reinforcement, the composites may be classified and this classification in depicted in Fig. 1.1. Further, particulate, whiskers, and fiber-reinforced composites are shown in Fig. 1.2. Matrix, a base material, provides the support to keep the fibers at desired location and orientation during loading condition, present in the continuous form in the composite material and also serves to transfer the load to the fibers. It also protects the fiber material from the physical damage due to change of temperature and humidity. The implementation of the composite materials in the structural design has enhanced the capabilities and trustworthiness of the structural components/system.

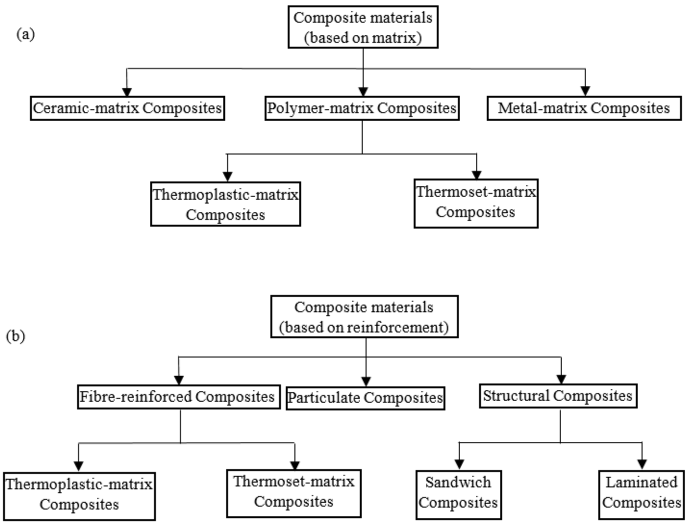

Fig. 1-1: Classification of composites (a) based on matrix material (b) based on reinforcement

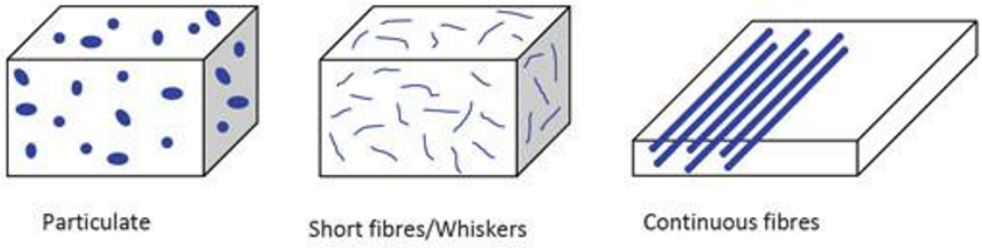

Fig. 1-2: Particulate, whiskers and fiber-reinforced composites

The composite material is no more an isotropic material and possess orthotropic material properties. Various orthotropic layers are bonded together to form a laminated structure. The composites and laminated composite structures are widely used in the form of plate and shell structures in structural applications. The performance of the composite material depends significantly on its reinforcement. Some of the materials used for the reinforcement are boron, silicon carbide, aluminum oxide, glass, carbon, etc.

1.4. Carbon Nanotubes and CNT Reinforced Composites

The fact that the attributes of CNT such as Young's modulus and shear modulus being comparable to diamond make it potential material for utilization in advanced materials and structures [2]. Furthermore, the nanotube parameters e.g. helicity, tube radius don't influence these attributes significantly [3]. The theoretical strength of CNT is about 110 times higher than that of the steel due to which it is one of the strongest material. Since their discovery, CNT fascinated researchers to research on their accurate prediction of material properties and modelling and analysis of in CNT reinforced structures. Noting that the performance of the composite material depends significantly on its reinforcement and CNT being a potential material is deemed as a worthy contender as reinforcement. The properties of the resulting composites such as mechanical properties, thermal properties, electrical properties, etc. can be enhanced remarkable by using CNT into the matrix.

The CNTs are the graphene sheets rolled in the shape of tube-shaped structure with the outer diameter in the nano-scale. On the basis of rolled sheet, the CNTs are generally classified as (a) single walled carbon nano-tubes (SWCNT) and (b) multi walled carbon nano-tubes (MWCNT). The SWCNT are seamless cylinders comprised of a layer of graphene wrapping a one-atom-thick layer of graphene. It is single time rolled carbon tube similar to a regular straw. Mostly, the diameter of SWCNT is close to 1 nanometer while its length is millions of times that of diameter. On the other hand, multi-walled carbon nanotube are also seamless cylinders comprised of many concentric layers of graphene wrapping around. The collection of complex array of concentric tubes of continuously increasing diameters. They have extremely small geometry and high aspect ratio. The diameter varies from 50-80 nm for outer diameter, and 5-15 nm for inner diameter. Fig. 1.3 depicts the rolled sheets of graphene in SWCNT and MWCNT.

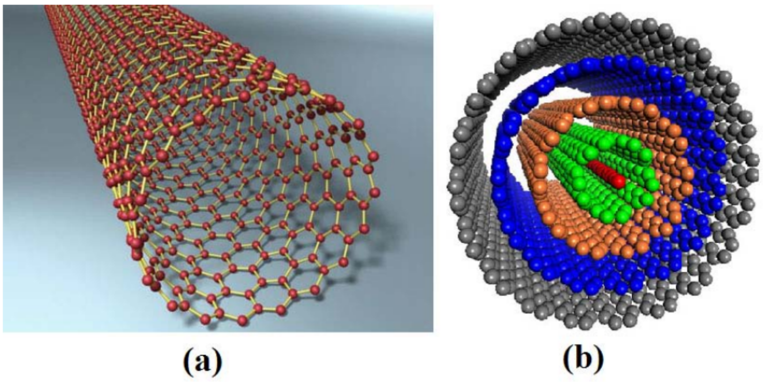

Fig. 1-3: Schematic of (a) SWCNT (b) MWCNT [4]

The experimental determination of properties of CNTs revealed that these exhibit extraordinary electrical properties [5], thermal properties [6] and mechanical properties [7, 8]. The CNT exhibit very high Young's modulus in the range of 0.4 to 4.15 TPa [7] and excellent specific properties such as specific strength, specific stiffness, etc. due to low density [8]. Due to these excellent properties, the CNT have been used as reinforced in the composite [9] and hybrid structures [10] to yield the CNT reinforced structures. The CNT reinforced structures are expected to provide potential application in aircraft materials and structures for lightning-strike applications, improving deicing, and allowing structural health monitoring and many such investigations are underway [11].

1.5. Crack Induced Failure

The structural components under service conditions are subjected to static as well as cyclic loads. These loading conditions may lead to the initiation of the crack or progress of the existing cracks which may have occurred due to composition of the material or during the fabrication. The presence of the cracks in the material components gives rise to stress concentration surrounding the region of the crack and those particular regions are subjected to extreme stresses leading to crack induced failure or fracture. Thus, the presence of the cracks significantly influences the overall structural integrity of the material components and degrades their service life. Moreover, the response of the structures is also influenced due to the presence of the crack. In the CNT reinforced composites, the matrix material may be prone to crack. Therefore, it becomes essential to examine the response of CNT reinforced structures in the presence of the crack and determine the influence of parameters associated with the crack onto the response of the structures.

1.6. Hygro-Thermal Environment

During their service life, CNT reinforced structures are exposed to environmental conditions such as change in temperature and change in moisture. The exposure to these environmental conditions give rise to strains which are temperature induced or moisture induced. In general, the expansion takes place in the material when it is subjected to positive moisture and temperature change. Noting that the constituent materials of CNT reinforced composite possess different properties (coefficient of thermal expansion and hygroscopic expansion), the presence of hygro-thermal environment lowers the strength and stiffness of the structure. Therefore, it is important to examine the response of such structures in hygro-thermal environment.

1.7. Modelling of CNT Reinforced Structures

The CNT reinforced structures are significantly employed in the form of plates and shells for the primary structures and due to which the need of accurate model which can precisely consider the complicating effects of such structures is paramount. There are two aspects in the modeling (a) mathematical models to predict properties of the CNTRC plates (b) mathematical models to predict the response of CNTRC plates. Various micromechanical methods (analytical as well as semi-empirical) such as rule of mixture, Mori-Tanaka Method, extended rule of mixture, etc. exist for the determination of effective properties of the CNTRC plates. In order to predict the response of the CNTRC plates at macroscopic level, the CNTRC plates have been analyzed in the similar manner as composite and functionally graded (FG) plates. Moreover, the shear deformation effects are significant in CNTRC due to high ratio of elastic modulus to shear modulus. The factors which govern the accuracy of the mathematical system are the manner in which the physical system is transformed to the mathematical system followed by the solution procedure implemented for solving the same. In structural mechanics, elasticity based approaches are implemented to yield the exact system in three-dimensional (3D) form. However, the 3D approaches are restricted to simplified cases of geometry and boundary. Therefore, the use of two-dimensional (2D) models is preferred for the modeling and analysis of plates and shells structures. These approaches can be classified as continuum based, asymptotic, and axiomatic type models [12]. In continuum based approach, a 3D continuum of the plate is seen as a surface and the corresponding stress resultants are defined on this surface. The introduction of 2D approximation is done at an appropriate level and the integration with respect to the thickness coordinate is then performed. In the framework of asymptotic approaches, a perturbation parameter (usually the plate-thickness to length ratio) is employed to expand the 3D governing equations and the theories are derived. These theories are relevant to the same order of perturbation parameter employed for the expansion. In the framework of axiomatic approaches, a precise displacement and/or stress field is assumed in the thickness direction, Axiomatic type approaches exhibit the benefit of permitting the establishment of 'intuitive' approximations into the plate behavior. The axiomatic type approaches can further be classified as displacement based, stress based or mixed formulation depending upon the choice of the approximation. The classification of the theories in the framework of composite and FG plates is depicted in Fig. 1.4.

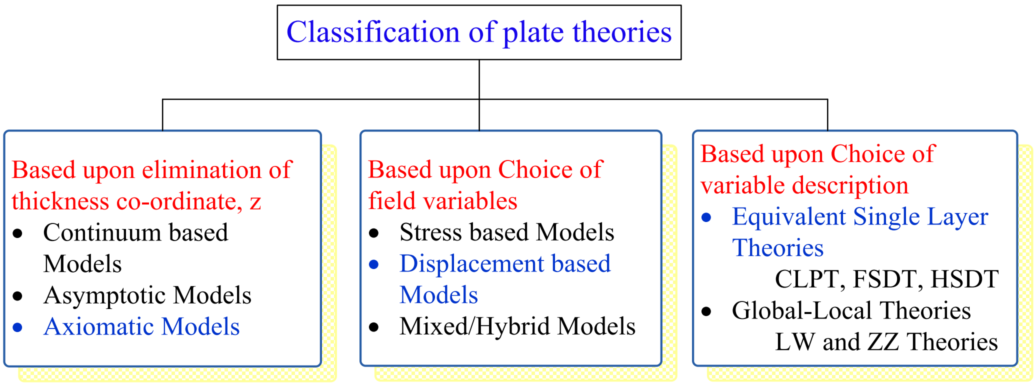

Fig. 1-4: Classification of Plate Theories

Each of these axiomatic approaches can further be categorized as equivalent single layer (ESL), zig-zag (ZZ) and layerwise (LW) approaches depending upon the choice of variable description. It is important to note that the shear deformation effects are prominent in CNTRC plates due to high ratio of Young's modulus to the modulus of rigidity. Therefore, the shear deformation plays a significant role while modeling the CNTRC plates. There exist several plate theories which incorporate the shear deformation effects in a unique manner. These are classified as classical laminated plate theory (CLPT), first order shear deformation theory (FSDT) and higher order shear deformation theory (HSDT). The choice of the mathematical model severely influences its capability to predict the response characteristics of structures. Therefore, a precise decision is essential prior to model and analyze the CNTRC structures.

1.8. Solution Methodologies

For accurate response analysis, the governing mathematical model of the physical system shall be solved using appropriate solution technique. Anisotropy and the couplings between in-plane and out-of-plane strains yield the governing equations which are generally highly coupled differential equations. The solution of these coupled differential equations makes the analysis of CNTRC structure cumbersome in practice. The availability of closed form (analytical) solutions is very few and applicable for particular conditions such as specific boundary and loading conditions. However, the real time applications are, in general, complex and include complex geometry, various boundary and loading conditions and hence the analytical approaches may not be appropriate for such cases. Therefore, the solution technique necessitates the implementation of approximated computational methods for most of the practical problems. Owing to the developments in the computational resources and requirement of analyzing complex engineering systems, there is a demand for the development of effective computational procedures for the solution of complex mathematical system relevant to physical behavior of CNTRC structures. The capabilities of the numerical methods to solve complex engineering problems and hence investigate the effect of system parameters on its response has made these a favorable choice as a solution methodology. The numerical methods such as Ritz method, discrete singular convolution, finite difference, finite element method (FEM), mesh-less methods, finite strip method, extended FEM (XFEM), and isogeometric analysis (IGA) have been widely employed for composite and FG plates and shells like structures. The finite element method plays a predominant role for the structural analysis among the available computational techniques. The research communities involved in the structural analysis in the academic and industrial institutions extensively employ the research oriented and commercial FEM codes such as ANSYS, NASTRAN, ABAQUS, etc.

1.9. Structural Analysis

A structure may be subjected to a variety of loads during its service life. In general, the forces acting on a structure can be broadly classified as conservative and non-conservative. In general, the structures deform when subjected to these forces. The forces may be of various kinds such as static, dynamic, hygro-thermal, aeroelastic, hydro-elastic, etc. In all such cases, the fundamental problem of the structural mechanics isthe evaluation of the deformational behavior of the structure. The response of the structures to these forces is the prime concern for a structural analyst in order to ensure the efficient, safe and reliable usage during their operation. Whenever CNTRC plates are used as a structural member, they are subjected to transverse loads and hence undergo bending. The action of these loads caused the plates to deform excessively, and cause the failure based on the stiffness of the CNTRC plate. Furthermore, the stresses are also induced which must be within the strength parameters of the material to avoid failure. On the other hand, the action of in-plane compressive forces modifies the profile of CNTRC plate in the lateral direction and hence cause the failure owing to buckling. This study is of prime importance in aircraft structures in particular where the skin of the structure, viz. wings, fuselage, etc., carries in-plane compressive loads of considerable magnitude. The structures in their operating conditions are also prone to self-excited vibration due to their inertia. The estimation of the fundamental frequencies is essential so as to avoid the resonance. Thus, the major structural responses of CNTRC plates are: static response, buckling response, and free vibration response, etc.

1.10. Aim of the Current Work

Following the above discussions, note that it is important to mathematically model and examine the structural (bending, buckling and free vibration) responses of the CNTRC plate. The effect of hygro-thermo-mechanical loading and existence of crack are also significant in such structures. Therefore, the aim of the current work is to mathematical model and analyze the structural responses of CNTRC plates with or without crack in the presence of hygro-thermo-mechanical loading.

1.11. Organization of the Thesis

This thesis consists of five chapters which include the introduction (chapter 1) and the conclusion (chapter 5). A detailed literature review is presented in the chapter 2. This chapter includes the various experimental and mathematical approach to synthesize and model the CNT reinforced composite. Further, various approaches to model the CNT reinforced plate and various solution methodologies to examine the response of composite, FG and CNT plates have been discussed. The literature review is also carried out in the framework of environmental conditions such as temperature and moisture on the composite, FG and CNT plates. Moreover, the presence of crack and the methodologies to model the crack geometry existing in the current literature have been reviewed. Based on the available literature, the gaps are recognized and, on those basis, the objectives and the scope of the presented work are framed.

A detailed mathematical formulation of the problem is presented in chapter 3. This chapter discusses the modelling of temperature dependent material properties and distribution of CNT for the FG-CNT reinforced plate. Moreover, the distribution of the CNT within the metallic phase is modelled in the framework of power law. The inverse hyperbolic shear deformation theory (IHSDT) in axiomatic framework is used to define the displacement field. Later, two different approaches are employed to develop the governing equation of motion. In the analytical approach, the strain displacement relation, constitutive relation and displacement field are employed in the principle of virtual work to develop the governing equation of motion for the structural and hygro-thermal-mechanical behavior of CNTRC plate. Further, these governing equations are simplified in the form of algebraic system using the closed form Navier solution for particular boundary constraints. The specific system of equations is presented for static, buckling and free vibration response. In order to enhance the applicability to general loading and boundary conditions, numerical solution in the framework of FEM and XFEM are developed. The principal of minimum potential energy is utilized to formulate the finite element methodology. An eight-node serendipity element with seven degrees of freedom per node is utilized to discretize the plate structure. The corresponding elemental matrices and vectors are obtained through associated energies and work done and these elemental matrices and vectors are assembled over the complete domain. The boundary conditions are then employed to specify the required boundary. Moreover, the discontinuities are modelled using XFEM. Heaviside and crack tip enrichment functions are used to model the crack face and crack tip, respectively. The response of FGCNT plate in presence crack is carried out by considering various loading conditions, volume fraction of CNT, boundary conditions, and crack length.

In chapter 4, the IHSDT is implemented and validated for static, buckling, free vibration and hygro-thermo-mechanical response of the CNTRC plate. Further, the effect of edge crack on the static response of FG-CNT reinforced plate is presented using extended finite element method. This chapter is divided into six sections namely the evaluation of temperature dependent properties of FG-CNT reinforced plate, static analysis of temperature dependent FG-CNT reinforced plate, buckling response of FG-CNT reinforced plate, free vibration of FG-CNT reinforced plate, hygro-thermo-mechanical response of FG-CNT reinforced plate and static analysis of edge cracked FG-CNT reinforced plate. Moreover, every section is divided into two sub section, one sub-section present closed form solution and another sub section present the finite element based numerical solution. It should be noted that the cracked plate has been analysed only in the framework of XFEM.

Further, in chapter 5, the current research work has been summarized and the important findings are listed. The possible scope of the future work is also discussed.

On the basis of the work presented in this thesis, the following papers are prepared.

1. Sharma, L.K., Bhardwaj, G. and Grover, N., 2021. Finite element framework for static analysis of temperature dependent IHSDT based functionally graded CNT reinforced plates. Mechanics Based Design of Structures and Machines, pp.1-22.
2. Sharma, L.K., Grover, N. and Bhardwaj, G., 2023. Buckling and free vibration analysis of temperature-dependent functionally graded CNT-reinforced plates. Journal of Vibration Engineering & Technologies, 11(1), pp.175-192.
3. Sharma, L.K., Bhardwaj, G. and Grover, N. Free vibration and buckling characteristics of temperature dependent FG-CNT reinforced plates in finite element framework of a non-polynomial axiomatic approach. (Communicated)

4. Sharma, L.K., Bhardwaj, G. and Grover, N. Finite element modelling for static response of the FG-CNT reinforced plates in hygro-thermal environment using inverse hyperbolic shear deformation theory (Communicated).

1.12. Summary

A general discussion of the domains considered in this work is carried out in this chapter. The motivation of the work is stated followed by the definition/significance of allied disciplines i.e., composite structures, CNT materials and structures, effect of presence of crack, effect of hygro-thermal environment, modelling approaches, solution methodologies and structural analysis. On the basis of the discussions made, the aim of the present research work is identified.

Chapter 2 LITERATURE REVIEW

2.1. Introduction

In the preceding chapter, it was observed that the modelling and analysis of CNTRC with or without the presence of crack in presence of hygro-thermal environment is an impending problem and stands as motivation to the current work. In view of the same, the extensive literature survey is carried out in the framework of the considered problem and presented categorically in this chapter. The objective of this chapter is to cite the significant work, which are related to the modeling and structural response of the CNTRC structures subjected to mechanical, thermal and moisture loading. The whole review process has been divided into two major sections. The first section deals with the estimation of material properties (experimentally and theoretically) of the CNT reinforced composite. Moreover, the second section is further divided into four subsections as follows:

1. Modeling of CNTRC plate
2. Structural analysis of CNTRC composite
3. Hygro-thermo-mechanical response of the CNTRC plate
4. Structural analysis of CNTRC cracked plate

2.2. CNT Reinforced Composite: Material Properties

In the past two decades, the tremendous efforts have been made towards synthesize of carbon nanotube reinforced composite material. Generally, they are synthesized by both chemical and physical method. There are various techniques to synthesize the CNT named as chemical vapor deposition, powder metallurgy, electrochemical deposition, laser ablation, nano-scale dispersion, carbon-arc discharge, and electric arc discharge. The experimental as well as theoretical approaches had been adopted in the existing literature to examine the effective properties of the CNTRC. These approaches are reviewed as follows.

2.2.1. Material properties: Experimental

Jang and Han [13] fabricated the composite with glass-fiber (GF) mat reinforced in the PMMA (polymethyl methacrylate) matrix with fiber volume fraction varied from 10% to 40%

and four kinds of FGM using a custom-made fiber mat manufacturing machine were manufactured. The effect of volume fraction of the mechanical parameters such as the flexural strength and absorption energy was studied for GF/PMMA composite. It was observed that the fiber content up to 30% vol. significantly improved these mechanical properties of GF/PMMA composite.

Lianxi and Erde [14] proposed a modified squeeze casting process to fabricate a metal matrix composite with ZK51A as a matrix material and SiC whiskers with diameter of 0.3~1.0 μm and length of 15~50 μm as reinforcement material. The tensile test and microscopic test involving scanning electron microscopy and transmission electron microscopy were conducted to examine the mechanical properties, fracture surface, and micro structure of the composite. The experimental results reveal that casting temperature and volume fraction of the whiskers contribute significantly in improving the mechanical properties of the metal matrix composite such as Young's modulus, tensile strength at yield point as well as at ultimate point.

Allaoui *et al.* [15] manufactured the CNT reinforcement composite using chemical vapor deposition by reinforcing CNT in epoxy polymer matrix with aromatic hardener (tri-ethylenetetramine). The effect of multi-walled CNT inclusion on the mechanical and electrical properties of the carbon nanotube/epoxy composite was examined. The results from the tensile test showed that, the elastic modulus doubles by adding 1 wt. % and quadruples with 4 wt. % of the CNT. From the electric properties, it was observed that samples transform from insulator to conductor for a CNT concentration of 0.5 to 1 wt. %.

Fidelus *et al.* [16] performed two different experiments to predict the modulus of elasticity using dynamic mechanical thermal analysis (EPLEXOR 500N) with 50×5×0.8 mm^3 specimen and toughness by using tensile impact notched specimen with specimen thickness of 0.22 mm, width 3 mm and gauge length 20 mm. The weight fraction of CNT used was varied from 0.01 to 0.5% which were randomly oriented in the epoxy resin. The experimental results reveal that substantial enhancement in the impact strength at 0.5 wt. % was observed.

de Villoria *et al.* [17] manufactured the SWCNTs using electric arc-discharge. The purification/ dispersion technique was used to fabricate the SWCNTs reinforced composite plate. Two different curing cycles were implemented to demonstrate the improvement in

Young’s modulus and tensile stress at 0.1 wt. % SWCNT reinforcement. The experimental results reveal that adding 0.1 wt. % of SWNT in the pure epoxy resin, the tensile strength was improved by 2.5% and 5.6% with two different curing cycles.

Sharma and Shukla [18] evaluated the mechanical properties of CNT reinforced composites. They carried out the tensile tests, flexural tests and tests for the inter-lamina shear strength on the manufactured specimens of CNTRC with varying percentage of CNT by weight. It was observed that the addition of 1.5 wt % of MWCNT resulted in increment of tensile strength, flexural modulus, bending strength, and shear strength by approximately 23%, 35%, 5%, and 7% respectively. They also employed the analytical models such as Voight-Reuss model, Halpin-Tsai model which are based on micromechanics for comparison and validations.

2.2.2. Material properties: Theoretical methods

Various micro-mechanical models exist in the literature to predict material properties of the CNTRC employing various approaches including elasticity, empirical and semi-empirical approaches. The effective elastic and mechanical properties of a material are dependent on the properties of the reinforcing material and the matrix phase and volume of fiber defined as volume fraction (V_f). The fiber volume fraction is the ratio of the volume of the fiber to the total volume of the composite. Considering no voids in the composite, the following relations can be established.

$$V_f + V_m = 1 \tag{2.1}$$

where the parameter V_m represents the matrix volume fraction. Various micro-mechanical models are available in the literature for calculation of the properties such as Young's modulus (E), shear modulus (G), Poisson’s ratio (ν), thermal expansion coefficient (α) of CNT reinforced composite. A brief discussion of the micro-mechanical models for fiber reinforced composites is given as follows.

i. Rule of Mixture.
ii. Halpin–Tsai model (H–T model).
iii. Mori-Tanka approach.

iv. Molecular Dynamics Simulation (MD).

Rule of Mixture

Huang *et al.* [19] predicted the effective properties (E_{11}, E_{22}, G_{12}, v_{12} and ρ) of the CNTRC composite using the extended rule of mixture (XROM). The XROM takes into account the scale-dependent parameters of the CNT by employing the efficiency parameters. The static and free vibration response of anti-symmetric CNTRC plate were examined employing four variable shear deformation theory.

Ansari *et al.* [20] used a modified rule of mixture along with finite element (FE) simulation to evaluate the elastic modulus of curved SWCNT/polymer composite. A comparison was made for the ratio of elastic properties of the constituents obtained from FE approach with that obtained from the modified rule of mixture. It was observed that the reinforcement of curved SWCNT in the polymer matrix leads to improve the elastic modules of the SWCNT/polymer composite.

Halpin–Tsai model (H–T model)

Huang and Gong [21] developed a multiscale FE model and an analytical approach to analyze the elastic properties of 3D woven composite with void deflect. The elastic properties E_{11} and v_{12} were computed using rule of mixture. The Halpin-Tsai equations in semi-empirical framework were implemented to compute the E_{22}, G_{12} and v_{34}.

Mori-Tanka approach

Shi *et al.* [22] implemented the Mori-Tanaka method to compute the influence of waviness and agglomeration of the CNT on the modulus due to randomly oriented, aligned and curved CNT. The study revealed that the enhanced material properties were achieved only by reinforcing controlled straight-shape CNT and even dispersion of CNT in the matrix material.

Molecular Dynamics (MD) Simulation

The classical molecular dynamics simulation to determine the properties of CNT based polymer composite were carried out by Han and Elliott [23]. The CNTR composite was modelled by implanting SWCNT in the polymer matrices. The polymers of PMMA and PmPV (poly (m-phenylenevinylene)-co-(2, 5-dioctoxy-p-phenylene) vinylene) were considered with different volume fraction of CNT. The elastic moduli (longitudinal as well as lateral) were evaluated using a method based on minimization of the strain energy. Also, one more micro-mechanical model, rule of mixture was implemented for the validation and comparison of the results evaluated by MD simulation.

Gajbhiye and Singh [24] employed the atomistic FEM with Tersoff-Brenner potential to predict the vibration response of SW carbon nanocones. The eigen value problem for the vibration analysis was solved through ANSYS by employing the Lanczos algorithm. Free vibration behavior as well as dynamic behavior due to impulsive excitation was examined.

Singh *et al.* [25] employed a MD approach to investigate the influence of functionalization on the properties of MWCNT. The interatomic interaction was modelled through condensed phase molecular potential and MD simulations were carried out with diverse densities. The influence of functionalization on the moduli (elastic, shear and bulk) and strength of CNT.

Ravindranath *et al.* [26] investigated the improvement in the material parameters of the MWCNT sheet wrapped around carbon fiber at room temperature. The material properties were estimated according to MD simulation.

2.3. CNT Reinforced Composites: Modelling

With the advancement in science and technology, the carbon nanotube is extensively used as reinforcement in the matrix material over the traditional reinforcement materials. Generally, the reinforced CNT is distributed uniformly, randomly or functionally graded (FG) in the matrix material. In the case of the uniform distribution (UD), the CNT is distributed uniformly throughout the transverse direction of CNT reinforced composite. Whereas in FG distribution, the resulting composite is a multi-phase composite with the smooth variation of CNTs across the thickness. The common distribution of CNTs is FG-V, FG-Λ, FG-O and FG-X. In FG-V distribution, CNT is more on the top plane and decreases gradually from the top to bottom plane across the thickness direction. In the case of FG-Λ distribution, CNT is more on the bottom plane and decreases gradually from the bottom to top plane across the thickness direction. In the case of FG-O distribution, CNT is more at the middle plane and decreases gradually towards the top and bottom plane across the thickness direction. In the case of FG-X distribution, CNT is more at the top and bottom plane and decreases gradually towards the middle plane across the thickness direction.

2.3.1. Modeling of CNT reinforced composite plate

The CNT reinforced structures are significantly employed in the form of plates and shells for the primary structures and due to which the need of accurate model which can precisely consider the complicating effects of such structures is paramount. In order to predict the response of the CNTRC plates at macroscopic level, the CNTRC plates have been analyzed in the similar manner as composite and FG plates. Moreover, the shear deformation effects are significant in CNTRC due to high ratio of elastic modulus to shear modulus. The factors which govern the accuracy of the mathematical system are the manner in which the physical system is transformed to the mathematical system followed by the solution procedure implemented for solving the same. In structural mechanics, elasticity based approaches are implemented to yield the exact system in 3D form. However, the 3D approaches are restricted to simplified cases of geometry and boundary. Therefore, the use of 2D models is preferred for the modeling and analysis of plates and shells structures. These approaches can be classified as continuum based, asymptotic, and axiomatic type models [12]. In continuum based approach, a 3D continuum of the plate is seen as a surface and the corresponding stress resultants are defined on this surface. The introduction of 2D approximation is done at an appropriate level and the integration with respect to the thickness coordinate is then performed. In the framework of asymptotic approaches, a perturbation parameter (usually the plate-thickness to length ratio) is employed to expand the 3D governing equations and the theories are derived. These theories are relevant to the same order of perturbation parameter employed for the expansion. In the framework of axiomatic approaches, a precise displacement and/or stress field is assumed in the thickness direction, Axiomatic type approaches exhibit the benefit of permitting the establishment of 'intuitive' approximations into the plate behavior. The axiomatic type approaches can further be classified as displacement based, stress based or mixed formulation depending upon the choice of the approximation. Each of these axiomatic approaches can further be categorized as ESL, ZZ and LW approaches depending upon the choice of variable description. It is worth mentioning that the shear deformation effects are prominent in CNTRC plates accounting towards high ratio of Young's modulus to the modulus of rigidity. Therefore, the shear deformation plays a significant role while modeling the CNTRC plates. There exist several shear deformation theories (SDT) which incorporate these effects in a unique manner. These are classified as CLPT, FSDT and HSDT. The CLPT doesn't consider the shear deformation while FSDT considers the linear shear deformation but doesn't meet the requirement of zero shear on top and bottom surfaces due to which it requires a correction factor for the evaluation of transverse shear stresses. The HSDTs, on the other hand, satisfy the zero shear conditions on the plate's upper and lower surfaces without the use of shear correction factor. There exist HSDTs wherein the shear conditions are satisfied additionally along with the formulation as well as the HSDTs wherein the shear conditions are satisfied inherently. In both these cases, the shear correction factor is not required. The HSDTs are further categorized as polynomial shear deformation theories (PSDT) and non-polynomial shear deformation theory (NPSDT) depending upon the manner the displacement components are expressed in terms of a function of the transverse coordinate. The choice of the mathematical model severely influences its capability to predict the response characteristics of structures.

2.3.1.1. Polynomial shear deformation theories

In the case when the displacement components are expressed in the higher order terms of thickness coordinates employing the Taylor's series, the PSDTs are formulated. The developed PSDTs in the past have been popularly employed for modelling of composite, FG and advanced composite plates and shells.

Reddy [27] developed a HSDT in particular third order shear deformation theory (TSDT) using the 3rd order terms of thickness coordinate. This theory considered the displacement field in which cubical function is used to define in-plane displacement and transverse deflection remain constant throughout thickness of the plate. Due to the presence of third order terms in the displacement components, the transverse shear strains and hence the corresponding stresses are parabolic along the thickness direction. The bending behavior of cross-ply laminated composite plates was obtained using a closed form solution following Navier solution.

Kant *et al.* [28] formulated a displacement based HSDT in the polynomial framework with 11 independent field variable. The in-plane displacements were assumed to cubic function of thickness coordinate while the transverse displacement was assumed to be parabolic yielding the linear normal strain in the thickness direction. They employed the theory in the FE framework to examine the dynamic analysis of plates which are single-layered isotropic as well as multi-layered orthotropic.

An improved transverse shear deformation theory using displacement approach was presented by Murthy [29]. The in-plane displacements (u, v) were defined in terms of cubic polynomial and transverse deflection was assumed independent of the thickness direction. They performed the bending response of symmetric cross-ply laminated and isotropic plates under uniformly distributed and sinusoidal load.

Swaminathan and Patil [30] presented the static analysis of anti-symmetric composite and sandwich plates with simply supported boundary conditions employing a 12 variable PSDT wherein the in-plane as well as transverse displacements were modelled through cubic polynomial. They implemented the principle of minimum potential energy to yield the governing system and solved the system analytically.

Talha and Singh [31] implemented the HSDT including stretching effect for the behavior of FG plates. The longitudinal displacements were assumed to vary cubically while the transverse displacement varied Parabolically through the plate thickness. The free vibration and static response of FGM plates based on finite element method was investigated. For the FE framework, the iso-parametric quadrilateral elements with 9 nodes and possessing the C^0 continuous were implemented.

2.3.1.2. Non-polynomial shear deformation theories

Contrary to PSDT, the non-polynomial functions of thickness coordinate are employed to depict shear deformation in NPSDTs. The shear strain function employed include trigonometric, exponential, inverse trigonometric, hyperbolic, and inverse hyperbolic, etc. While considering the shear strain shape function, the condition for zero transverse shear stress at top and bottom surface must be satisfied.

Touratier [32] presented a new standard plate theory by considering sinusoidal function as the shear strain function, and analyzed the several significant problems on bending, free vibration, bucking of laminated and sandwich plates. The accuracy of the presented theory was ascertained relative to FSDT.

Shimpi *et al.* [33] developed a HSDT having a trigonometric displacement model. The displacement field was chosen in such a manner that it satisfies the zero transverse shear stress conditions at top and bottom of the composite plate. The results were evaluated for static and free vibration responses of rectangular isotropic, orthotropic and layered plates.

Aydogdu [34] proposed a new HSDT with a displacement field assumed in terms of exponential shear strain shape function with five unknowns. Numerous studies were carried out for bending, free vibration and buckling responses of composite plates.

Meiche *et al.* [35] presented a new four variable refined HSDT which used hyperbolic function to account for the transverse shear deformation. They derived the governing equations using Hamilton's principle for FG sandwich plate. The results were presented for buckling and free vibration response of the thick FG sandwich plate.

Mantari *et al.* [36] developed a new trigonometric SDT to study the static bending analysis of isotropic, laminated composite and sandwich plates. They employed the principle of virtual work (PVW) to develop the governing equations of equilibrium and solved using Navier type closed form solution. Mantari *et al.* [37] presented static behavior of FGM plate modelled with HSDT which was based on a new tangential-exponential displacement model.

Thai *et al.* [38] proposed an inverse trigonometric SDT which includes the inverse tangent function to account the shear deformation in the transverse direction of plate structure. The structural analysis problem (static, buckling and free vibration) was formulated in the weak form for composite and sandwich plates and solved using a numerical approach in the framework of isogeometric analysis (IGA) satisfying C^1 requirement. Numerous studies were conducted to examine the structural responses of the considered plate structures.

Sarangan and Singh [39] proposed new SDT with algebraic, exponential, logarithmic and trigonometric functions. The results were obtained for static, free vibration and buckling responses of laminated and sandwich plates using a Navier type closed form solution. The effect of specifications (span-thickness ratio, modulus ratio, number of layers, orientation of layers and type of loading) on the non-dimensional transverse deflection, buckling load parameter and fundamental frequency were examined for the considered plates.

Grover *et al.* [40-41] developed a new inverse hyperbolic and trigonometric shear strain shape functions to account the transverse shear stress in the displacement field. The theory used inverse hyperbolic ($\sin^{-1}$) and trigonometric ($\cot^{-1}$) displacement models to express the variation of shear strain across the thickness direction.

2.3.2. Structural analysis of CNTRC plates

Whenever CNTRC plates are used as a structural member, they are subjected to transverse loads and hence undergo bending. The action of these loads caused the plates to deform excessively and cause the failure based on the stiffness of the CNTRC plate. Furthermore, the stresses are also induced which must be within the strength parameters of the material in order to avoid failure. On the other hand, the action of in-plane compressive forces modifies the profile of CNTRC plate in the lateral direction and hence cause the failure owing to buckling. This study is of prime importance in aircraft structures in particular where the skin of the structure, viz. wings, fuselage, etc., carries in-plane compressive loads of considerable magnitude. The structures in their operating conditions are also prone to self-excited vibration due to their inertia. The estimation of the fundamental frequencies is essential so as to avoid the resonance. Thus the major structural responses of CNTRC plates are: static response, buckling response, and free vibration response, etc. Over the past few decades, there is an increase in the applications of the CNTRC in the design of aerospace, aeronautics, marine and automobile structures. In order to ensure their efficient use, a good understanding of static, vibration and buckling responses of such structures under various loading conditions is required. The literature review reveals that many solutions have been developed to study the structural response of the CNT reinforced composites. For accurate response analysis, the governing mathematical model of the physical system shall be solved using appropriate solution technique. Anisotropy and the couplings between in-plane and out-of-plane strains yield the governing equations which are generally highly coupled differential equations. The solution of these coupled differential equations makes the analysis of CNTRC structure cumbersome in practice. The availability of closed form (analytical) solutions is very few and applicable for particular conditions such as specific boundary and loading conditions. However, the real time applications are, in general, complex and include complex geometry, various boundary and loading conditions and hence the analytical approaches may not be appropriate for such cases. Therefore, the solution technique necessitates the implementation of approximated computational methods for most of the practical problems. Owing to the developments in the computational resources and requirement of analyzing complex engineering systems, there is a demand for the development of effective computational procedures for the solution of complex mathematical system relevant to physical behavior of CNTRC structures. The capabilities of the numerical methods to solve complex engineering problems and hence investigate the effect of system parameters on its response has made these a favorable choice as a solution methodology. The numerical methods such as Ritz method, discrete singular convolution, finite difference, finite element method (FEM), mesh-less methods, finite strip method, extended FEM (XFEM), and isogeometric analysis (IGA) have been widely employed for composite and FG plates and shells like structures. The finite element method plays a predominant role for the structural analysis among the available computational techniques. In the following paragraphs, the response of the CNTRC plates carried out in the framework of analytical and numerical approaches has been classified and reviewed.

2.3.2.1. Analytical solutions

In the analytical solutions, the governing equations obtained through principles of structural mechanics (PVW, structural kinematics, displacement field, and constitutive relations) are solved in the exact manner, generally for the specific cases. The solutions in closed form always ascertain the accuracy due to the fact that these solutions are exempted from any computational/numerical error. In general, the analytical approaches available for composite ad FG plates had been employed for CNTRC plates.

Shen [42] modelled the CNTRC plate with Reddy's HSDT and obtained the mathematical system of equations for the non-linear bending response in the thermal environment. They employed the XROM for the determination of properties of the CNTRC. The mathematical system so obtained was solved in the closed form for the specific set of boundary conditions i.e. simply supported. They considered two sets of simply supported boundary conditions. In the first case, the edges were assumed to translate freely in x and y direction while being constrained in the transverse direction. On the other hand, in second case, all the displacements were restricted along the edges.

Alibeigloo [43] used the theory of elasticity to predict the bending response of the simply supported CNTRC plate along with the piezoelectric layers. They used a Fourier series expansion for stress components as well as for the displacement components. The state space approach was used across the thickness to derive the solution in the closed form. It was noted that the voltage was induced across the thickness of the sensor due to the application of the mechanical load which increases linearly due to increase in load. Moreover, the influence of the applied voltage was observed to be more on the transverse parameters relative to the in-plane parameters.

Zhang *et al.* [44] modelled the CNTRC plate with Reddy's HSDT and developed the mathematical system for vibration response of the considered plates in presence of in-plane forces. For solution of the developed mathematical system, they employed a closed form approach based on Levy's method in conjunction with the state space method. Due to usage of Levy solutions, the boundary conditions of simply supported type, clamped type, and free type were used in the specific combinations for the analysis. They also examined the influence of in-plane loads on the vibration behaviors of the considered plates.

Huang *et al.* [45] carried out the investigation for the static response as well as for the free vibration response of anti-symmetrically laminated CNTRC plate based on four-variable SDT and presented the analytical solutions using Navier type closed form solution. They developed governing equations using Hamilton's principle and implemented XROM for evaluating the equivalent properties.

Wang *et al.* [46] carried out the studies pertaining to the vibration and static analysis of nanoplatelets reinforced composite doubly-curved shallow shell. The governing equations were developed on the bases of Hamilton principle and HSDT. The fundamental frequency and central deflections were obtained using Navier type solution. The effect of different parameters (distribution of nanoplatelets, span-thickness ratio, shallowness ratio, curvature radius ratio, weight fraction, etc.) on the mechanical behaviour were examined for the nanoplatelets reinforced composite doubly-curved shallow shell.

Soni *et al.* [47] formulated the inverse hyperbolic shear deformation theory for static response of the CNTRC plate subjected to transverse loads. The governing equations of motion were formulated using PVW and solved by implementing Navier's type closed form solution. The transverse loads considered were point load, uniformly distributed load, and sinusoidal loads. The effect of various specifications such as CNT volume fraction, span-thickness ratio, distribution of CNT, and different mechanical load, etc. on the transverse deflection and stresses were examined for the CNTRC plates.

Singh and Sahoo [48] formulated the trigonometric SDT for the modelling the CNTRC plate and carried out the static analysis and free vibration characteristics. For the static analysis, the plates were subjected to transverse loads of uniform as well as sinusoidal. The effective properties were evaluated using the XROM. The Hamilton's principle was used to develop the mathematical system of equations which was solved in the closed form following Navier approach. Numerous studies were conducted to examine the influence of specifications on the non-dimensional transverse displacement and stresses.

Bousahla *et al.* [49] evaluated the buckling and dynamic behaviour of the CNTRC beam resting on Winkler-Pasternak foundation using integral type FSDT. The theory involves only three variables but uses a shear correction factor due to consideration of FSDT. The mathematical system was developed and solved using Hamilton's principle and Navier solution, respectively.

There exist several studies wherein the CNTRC plates have been modeled in the framework of SDT and solved in the closed form for the analysis of such structures [50-52].

2.3.2.2. Numerical solutions

Despite the fact that analytical solution is free from any computational error and easy to implement, they are, in general, restricted to specific cases of boundary conditions and loading conditions. On the other hand, the capabilities of the numerical methods to solve complex engineering problems and hence investigate the effect of system parameters on its response has made these a favorable choice as a solution methodology. The numerical methods such as Ritz method, discrete singular convolution, finite difference, finite element method (FEM), mesh-less methods, finite strip method, extended FEM (XFEM), and isogeometric analysis (IGA) have been widely employed for composite and FG plates and shells like structures. The response of the CNTRC plates carried out in the framework of numerical approaches is reviewed as follows.

Zhu *et al.* [53] analyzed the CNTRC plates in the framework of finite element analysis by employing the Lagrangian interpolation functions and carried out the bending and free vibration responses. They also validated the results using ANSYS by modeling the CNTRC plates with SHELL 181 and SHELL 99 element from the element library of the ANSYS. The plate structure was modelled using the FSDT while the material properties were obtained through XROM. The material properties were determined employing XROM. The influence of plate specifications on the considered response were evaluated.

Sharma *et al.* [54] employed 3-D generated shell element to examine the vibration characteristics of FG porous plates. The displacement field was expressed on the basis of Reissner-Mindlin assumptions. A degenerated 3D element with eight nodes and five field variables defined at each node is considered and on those basis, FE matrices are obtained and solved for the considered response.

Lei *et al.* [55] employed element-free kp-Ritz method to determine the buckling behavior of CNTRC plates. They implemented Eshelby-M-T approach as well as XROM to predict the properties and obtained the total potential energy function using FSDT. The shape function in the considered approach were assumed as combination of the kernel function and the correction function and the latter was further assumed as linear combination of the quadratic basis function and the coefficient function.

Kiani [56] examined the shear buckling behaviour of CNTRC plate in a thermal environment using two-dimensional Ritz method with Chebyshev polynomial. They employed a modified ROM for evaluating the properties. The set of governing equations were obtained using the FSDT. In the adopted methodology, the field variables (5 in number) were expressed in terms of Chebyshev polynomials and auxiliary functions which correspond to the essential constraints due to boundary.

Lei *et al.* [57] examined the free vibration behavior of the CNTRC straight-side quadrilateral plates resting on elastic foundation. They employed FSDT and IMLS-Ritz method to model the mathematical system of the considered plate and hence solved the same for the vibration characteristics. In the considered solution methodology, they employed basis functions and the functions of spatial coordinates. The weight functions were expressed using the cubic splines.

Bhagat *et al.* [58] carried out the analyses of CNTRC cylindrical panels using ANSYS based FE tool buckling. In particular, they carried out free vibration and buckling behavior by considering the temperature dependent properties and in presence of thermal field. They adopted the element from element library of ANSYS as SHELL 281 which is an eight-noded element with six degree of freedom at each node.

Mehar *et al.* [59] computed the buckling load parameter of the CNTRC sandwich shell subjected to uniform thermal loading in the framework of PSDT using FEM. An isoparametric element with nine nodes and having nine degree of freedom per node is used to discretize the panel.

Liu *et al.* [60] proposed C^1 continuous refined plate theory (RPT) to investigate the static and free vibration behavior of CNTRC plate. A NURBS-based isogeometric analysis (IGA) was implemented to solve the problem.

Xiang *et al.* [61] employed element-free kp-Ritz method and carried out the free vibration response of CNTRC conical shell panels modelled in the framework of FSDT. Two-dimensional kernel particle shape function is considered to approximate the function.

There exist several studies wherein the CNTRC plates have been modeled in the framework of SDT and solved in the approximate manner for the analysis of such structures [62-67].

2.3.3. Hygro-thermo-mechanical response of the CNT reinforced plate

During their service life, the CNTRC structure is subjected to different environmental conditions. They are exposed to thermal and moisture environment. Due to high-temperature and moisture working condition, it affects the stiffness and strength of the composite structures. Therefore, it is important to investigate the hygro-thermo-mechanical response of the CNTRC structures. In this subsection, a concise literature review is presented on the response of composite and CNTRC plate in the hygro-thermo-mechanical loading conditions.

Wu and Tauchert [68] studied the response of anti-symmetric rectangular laminated plates with simply supported boundary condition in the framework of CLPT. The plates were assumed to be subjected to constant temperature as well as linearly variation in temperature. They concluded that the various parameters (aspect ratio, number of ply and orientation) have a significant effect on the non-dimensional central deflection subjected to constant and linear temperature variation.

Reddy and Hsu [69] investigated the anisotropic composite plate subjected to mechanical and thermal loading in the framework of FEM. The governing equation were developed on the basis of FSDT. On the other hand, to ensure the accuracy of FE solution, the analytical solution was also obtained for specific case (simply supported cross-ply plate). The studies pertaining to the response of plates (cross-ply as well as angle ply) under sinusoidal and uniform mechanical, thermal and combined load were carried out.

Khdeir and Reddy [70] presented the thermo-elastic analysis of cross-ply composite plate with different boundary conditions based on HSDT and compared with the obtained CLPT and FSDT results. The obtained mathematical system was solved following the Levy solution. Numerous studies were performed to examine the impact of span-thickness ratio, stacking sequence, boundary constraints on the non-dimensional deflection and stresses arising due to sinusoidal distributed temperature load.

Khare *et al.* [71] formulated various HSDTs to investigate the doubly curved laminated and sandwich shallow shells under thermo-mechanical loading conditions. The results for the simply supported boundary constraints were presented for the non-dimensional central deflection of cylindrical as well as spherical shells exposed to sinusoidal thermal load.

Based upon sinusoidal plate theory (SPT), Zenkour [72] presented the bending analysis of the composite plate under sinusoidal mechanical and non-linear sinusoidal thermal load. The analytical solutions were presented for simply supported laminated plate by using Navier type solution. The influence of diverse parameters including the aspect ratio, span-thickness ratio, stacking sequence and material anisotropy on the transverse central deflection exposed to thermal load and combined thermo-mechanical loads were presented.

Mechab *et al.* [73] studied the orthotropic multilayered plates exposed to thermo-mechanical load based on HSDT. In this theory, trigonometric shear strain functions were used to represent the shear deformation in transverse direction. The mathematical system was yielded and solved through PVW and the series solution based on Navier method, respectively. The results were presented for non-dimensional central deflection of the plates exposed to constant, linear and non-linear sinusoidal temperature distribution.

Cetkovic [74] utilized the generalized LW approach to model the multilayered composite and sandwich plates and carried out the thermo-mechanical bending response. The finite element and close-form results were computed. Numerous examples were considered to show the impact of diverse specification including span to thickness ratio, aspect ratio, orientation and stacking sequence on the response characteristics of the considered plates.

Biswal *et al.* [75] examined the vibration response of woven fiber glass/Epoxy laminated composite shell subjected to hygro-thermal environment using numerical and experimental methods. The governing equations were developed using FSDT and FEM modeling.

Shen [76] investigated the thermal post-buckling for CNTRC cylindrical shells subjected to uniform temperature field. They modelled the plate structure in the multi-scale framework under the assumptions of HSDT and von-Karman type nonlinearity. They found that mid-plane symmetric distributed CNTs enhances the buckling temperature and the thermal postbuckling strength of the shells.

Wang *et al.* [77] studied buckling and vibration response of the CNTRC quadrilateral plates in thermal environment based on the mesh-less method modelled in the framework of FSDT. The associated shape functions were formed using moving least-square approximation. The effective properties were evaluated using ROM and the impact of diverse specifications like volume fraction, distribution of CNT and span-thickness ratio on the natural frequency and buckling load parameter were discussed for the considered plates.

Ansari *et al.* [78] analyzed buckling and vibration of CNTRC annular sector plates resting on elastic foundation using FSDT. The material parameters were evaluated using extended rule of mixture. Hamilton's principle and variational differential quadrature were implemented to develop the reduced form of the governing equations.

Duc *et al.* [79] presented the thermal and mechanical behavior of CNTRC truncated conical shell exposed to thermal environment surrounded by elastic foundations. The authors implemented the Galerkin method to solve the governing equations.

Chavan and Lal [80] investigated the dynamic bending of CNTRC plate exposed to hygro-thermo-mechanical loading conditions. The governing equations were formulated using dynamic version of the HSDT. A C^0 continuous nine noded isoparametric element having seven field variables per node were considered for finite element modeling.

Biswal *et al.* [81] studied the free vibration response of woven fiber glass/epoxy laminated composite cylindrical shallow shells using experimentally and numerically in the effect of hygrothermal conditions. In the numerical studies, the governing equations were formulated and solved using FSDT and finite element method. However, in an experimental study, the vibration response of the square woven fiber glass/epoxy composite cylindrical shell panel was subjected to CFFF boundary conditions and different temperature and moisture concentrations using the Bruel and Kjaer FFT analyzer. It is observed that there is a good agreement between numerical and experimental results.

Patel *et al.* [82] investigated the free vibration behaviour of multiwall carbon nanotube composite plate with random distribution and different weight percentage (0.1, 0.2, 0.3, 0.4 and 0.5) using experimentally and numerically methods. The MWCNT was prepared using conventional hand lay-up technique for different weight percentage. In experimental study, the natural frequency of vibration of MWCNT was obtained using Burel and Kjaer fast Fourier transformation.

Panda *et al.* [83] presented the buckling analysis of bidirectional glass/epoxy composite panels with delamination under the hygothermal effect. Firstly, numerical results were obtained using finite element method in the framework of FSDT and compared with experimental results. It is concluded that the numerical results were in good agreement with the experimental results.

Biswal *et al.* [84] studied the buckling response of woven fiber glass/epoxy laminated composite cylindrical shell panels using numerical and experimental methods under the effects of moisture and temperature. In the numerical study, the governing equations were developed using FSDT, and solutions were presented using the finite element method. It is concluded that the numerical results computed using FEM were in good agreement with the experimental buckling test results.

Rath and Sahu [85] presented the free vibration response of the laminated composite plate in the influence of hygrothermal conditions. The studies were carried out numerically and experimentally under uniform temperature and moisture conditions. It is concluded that the numerical results were in good agreement with the experiment's results. Moreover, the natural frequency decreases with increasing of temperature and moisture concentrations.

Panda *et al.* [86] investigated the free vibration analysis of woven fiber glass/epoxy composite plates with delamination subjected to temperature and moisture conditions based on numerical and experimental methods. The numerical study was carried out using the finite element method in the framework of FSDT. However, the experimental studies had been carried out using Bruel and Kjaer first Fourier transformation analyzer. It is concluded that the FEM based numerical results were in good agreement with the experimental results.

2.3.4. Structural analysis of CNT reinforced cracked composite

The structural components under service conditions are subjected to static as well as cyclic loads. These loading conditions may lead to the initiation of the crack or progress of the existing cracks which may have occurred due to composition of the material or during the fabrication. The presence of the cracks in the material components gives rise to stress concentration surrounding the region of the crack and those particular regions are subjected to extreme stresses leading to crack induced failure or fracture. Thus, the presence of the cracks significantly influences the overall structural integrity of the material components and degrades their service life. Moreover, the response of the structures is also influenced in the presence of the crack. In the considered CNT reinforced composites, the matrix material may be prone to crack. Therefore, it becomes essential to examine the response of CNT reinforced structures in the presence of the crack and determine the influence of parameters associated with the crack onto the response of the structures. Moreover, to simulate the response of cracked structures, various methods such as meshfree method, finite element method, finite difference method and extended finite element method are available in the literature. Among these XFEM is most suitable and widely used method among research community. This method allows the modeling of crack geometry independent of mesh and completely avoid the re-meshing of the crack growth. In the following paragraph, the mathematical approaches concerning the modelling of crack, discontinuities, and dislocations for isotropic, composite, and FG plates are reviewed.

Singh *et al.* [87] employed extended finite element method (XFEM) to analyze an FGM plate with multiple discontinuities such as major crack, minor crack, holes and inclusions under cyclic loading. A C^0 continuous nine noded Lagrangian quadrilateral element was chosen for domain discretization. The results were obtained for stress intensity factor (SIF) and Von-mises stress in the present of multiple discontinuities.

Singh *et al.* [88] examined the fatigue life of a cracked plate with multiple discontinuities such as holes, inclusions and minor cracks using XFEM. The discontinuities were modeled using enrichment function and nine noded lagrangian quadrilateral element. The results were obtained for the fatigue life and SIF for the considered problem.

Bhattacharya *et al.* [89] formulated the fatigue crack growth using XFEM for bi-layered material subjected to thermo-mechanical loads using XFEM. The Paris law was implemented to evaluate the rate of crack growth in the bi-layered material. The results were obtained for SIF in the presence of a left edge crack, a right edge crack and a central crack.

Bhi and Zhang [90] examined the cracked homogeneous and linear magnetoelectroelastic solid for dynamic intensity factor using XFEM.

Kumar and Bhardwaj [91] implied the new enrichment scheme combined with XFEM. The crack was modeled using a Heaviside function along with a ramp function. The developed methodology was implemented to examine the stable crack growth for the materials which are ductile in nature.

Duhan *et al.* [92] implemented XFEM to model the dislocations across the edges and hence analyse the thermo-mechanical response. The influence of temperature change is considered in the domain form of J-integral and on those basis, Peach-Koehler force is determined. Various studies involving dislocations are presented.

Nasirmanesh and Mohammadi [93] investigated the buckling analysis for uni-layer composite plate using XFEM. An eight noded degenerated shell elements were used to discretize the plate geometry. Numerous examples were solved to study the influence of parameters such as orientation of fiber, crack angle and crack length on the critical buckling parameter.

Lal *et al.* [94] implemented XFEM to evaluate the mixed mode SIF and carried out the propagation of crack for the composite plate with center crack. Reliability analysis was also conducted in the framework of Monte Carlo simulation and perturbation technique. The effect of diverse parameters including the crack length, orientation of the laminate, and the crack angle on the reliability analysis were presented.

Yu and Bui [95] presented a local adaptive XFEM to precisely model the strong as well as weak discontinuities in the plate. The modified level set and variable node elements were adopted to model the discontinuities in the plate. The comparison was made between XFEM and new adaptive local mesh refined XFEM results for the plate with various discontinuities.

Li *et al.* [96] examined the fracture in graphene and cross-linked epoxy using continuum and molecular dynamic scale. The results were presented for crack propagation in graphene sheets and cross-linked polymers.

Sahu and Das [97] studied the vibration response of laminated cracked composite beam using numerical and experimental methods. In the numerical study, the governing equations were developed using FSDT, and solutions were presented based on the finite element method. In an experimental study, the woven roving glass/epoxy composite specimens with pre-defined cracks were prepared using the hand layup technique. It had been concluded that the numerical results were in good agreement with the experimental results.

2.4. Observations from Literature Survey

A detailed review considering the various aspects of evaluating the material properties of CNT reinforced composite using experimental and mathematical techniques, along with modelling and response of CNT reinforced composite structures in hygro-thermal environment is carried out. The presence of crack is also considered. The observations on the basis of the literature review are as follows:

- The implementation of non-polynomial shear deformation theory is limited to structural response of composite structures. However, the CNT reinforced composites are not modelled in the framework of NPSDTs as evident from the literature review.
- The implementation of NPSDTs in the framework of analytical and numerical (FEM) is limited to laminated composite material.
- The responses of CNT reinforced composite are generally examined under linear structural kinematics. The implementation of non-linear strain-displacement relations may help in prediction of non-linear response.
- The material properties of constituent materials are considered to be temperature independent. However, in external environments, these properties vary due to change in the temperature. The consideration of the temperature dependent material properties shall assist in accurate prediction of response.
- The implementation of fracture mechanics to study the reliability of structure in the condition of crack and void growth possess substantial utility. The CNT reinforced composite structures in the presence of cracks and voids may behave differently and effect of these racks and voids needs to be considered.

2.5. Objective and Scope of Present Work

From the observations made in the previous section, it is observed that several research gaps exist for the modelling and structural response of CNTRC plates. Meanwhile, recent research work focused on the structural behavior of CNTRC plate, very few actually work on the effect of the temperature dependent material properties, hygro-thermo-mechanical environment conditions and crack on the structural behaviour of the CNT reinforced plate.

Hence there is a need for such studies to be carried out. With these points in view, the objective is defined as:

To mathematically model and examine the structural (bending, buckling and free vibration) responses of the functionally graded carbon nanotube (FG-CNT) reinforced composite plate. The effect of hygro-thermo-mechanical loading and existence of crack are also significant. The objectives of the present work are defined as follows.

- Modelling and analysis of CNT reinforced composite plate and comparison with laminated composite.
- Hygro-thermal analysis of CNT reinforced composite plate.
- Hygro-thermal analysis of cracked CNT reinforced composite plate.
- Failure analysis of CNT reinforced composite plates using XFEM.

2.6. Methodology to Achieve the Objectives

The following methodology is followed to achieve the research objectives:

- To achieve the first objective, a displacement field is assumed in the framework of IHSDT. By implementing the stain-displacement relation and constitutive relation in the PVW, the governing differential equations are obtained for analytical solution. Similarly, for numerical solution, finite element methodology is developed by implementing the global elastic stiffness matrix, global geometrical stiffness matrix, force matrix and mass matrix in the principle of minimization of total potential energy. The effective elastic properties of CNTRC are evaluated using XROM. Further, the closed form and finite element solutions are used to study the structural behavior of CNT reinforced plate and comparison is made between the CNT reinforced plate and isotropic plate.
- To achieve the second objective, the mathematical modelling is developed using analytical (Navier type closed form solution) and numerical (Finite element solution) solution for FG-CNT reinforced plate based on the IHSDT. The material properties are considered as temperature dependent. The load vector corresponding to thermal and moisture terms are evaluated and considered in the algorithm. Further, the results are obtained for static behavior on the FG-CNT reinforced plate in the present of thermal

and moisture conditions. The response of FGCNT plate is carried out by considering various loading conditions, volume fraction of CNT, boundary conditions, etc. A general procedure to model and analyze the CNTRC plates is outlined in Fig. 2.1.

- To achieve third and four objectives, the FGCNT plate is assumed with a re-existing crack. Due to the presence of the crack, the conventional FEM fails to predict the response due to discontinuity. Therefore, extended FEM (XFEM) is employed to model the crack face and crack tip. The crack geometry defined in terms of crack face and crack tip is modeled with the help of the Heaviside functions and crack tip functions, respectively. The response of FGCNT plate in presence of the crack is carried out by considering various loading conditions, volume fraction of CNT, boundary conditions, and crack length.

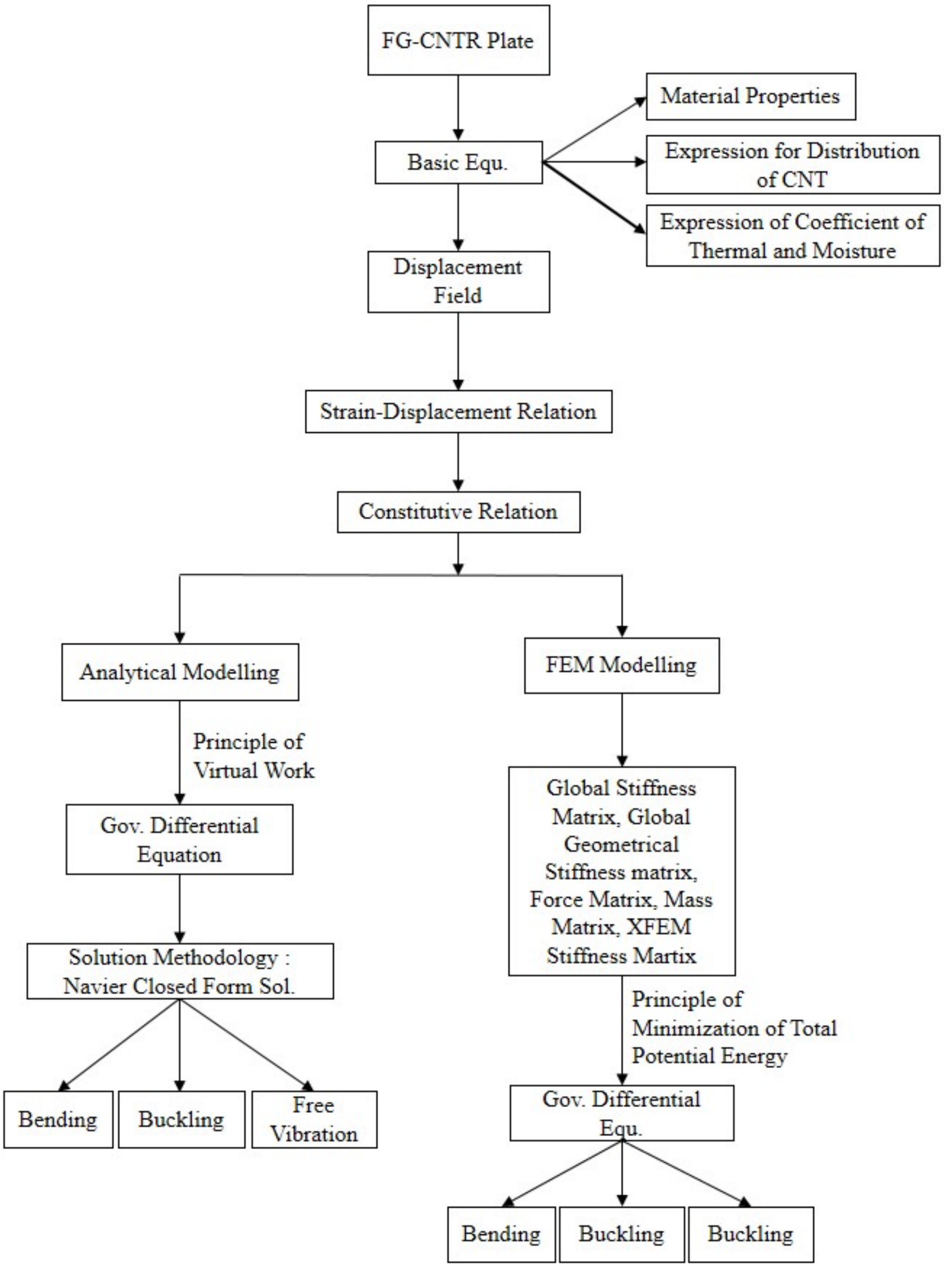

Fig. 2-1: Flow chart to model and analyze the FGCNT plates

2.7. Summary

A study has been carried out on the various Micro-mechanical models, structural analysis, hygro-thermal effect and fracture analysis for the carbon nanotube reinforced composite materials. Some of the more interesting works were listed and on those basis, the observation from the review are identified. With the help of these observations from the literature as well as motivation of the work, a suitable research gap is selected and the objectives for the current study are framed. The methodology adopted to achieve these objectives along with the guidance and required basic knowledge as to how the present study should be conducted is also presented.

Chapter 3 MATHEMATICAL FORMULATION

3.1. Introduction

This chapter presents the detailed mathematical formulation which is developed in the framework of inverse hyperbolic shear deformation theory. The assumptions made for the modeling and analysis of CNT reinforced composites are presented. The micromechanical model to predict the properties of CNTRC is presented for the variety of distributions of CNTs. These are presented by utilizing the extended rule of mixture and power. The strain-displacement relations, displacement field, and constitutive relationship are presented to represent the structural kinematics, deformation behavior, and material behavior. The system of differential equations is first obtained in the form of Euler-Lagrange equations by employing the principle of virtual work. These governing differential equations are further simplified in the form of primary field variables. The governing differential equations are solved in the closed form by implementing the Navier solution for simply supported boundary conditions. The mathematical system in algebraic form is then obtained for structural analysis (static, buckling and free vibration) of CNTRC plates. Further, the finite element methodology is presented in order to ensure the generality of the developed formulation for more complex boundary and loading conditions. The finite element framework is developed in the framework of principal of minimum potential energy i.e. Lagrange equations. The discretization of the plate domain is done using quadrilateral serendipity elements with eight nodes. The associated elemental matrices and vectors are derived for the considered problem and these are assembled over the plate domain. Following the use of appropriate boundary conditions, the governing system of equations is classified for the specific analysis. Furthermore, the failure in the plate is considered in the form of a pre-existing crack. The modeling of the crack is done utilizing the concept of extended finite element method. The Heaviside function and crack tip enrichment function is used to model the discontinuity and the crack tip. The detailed formulation for extended finite element method is presented. A brief description of the implementation of the developed formulation into the computer codes is also presented along and the chapter description is summarized.

3.2. Assumptions

The mathematical development made in the present work is based upon the following assumptions:

1. The reference plane for defining the displacement and rotation-based field variables is considered to be the middle plane (at $z = 0$).
2. The distribution of CNT within the continuous phase is assumed to be uniformly distributed and functionally graded based on the power law.
3. The material is linearly elastic, uniform and homogenous.
4. The transverse normal is inextensible i.e., the transverse deflection is small relative to thickness of the CNTRC plate.
5. The structural kinematics is based on the assumption that the rotations and displacements are small.
6. The normal strain in the transverse direction is negligible implying that the corresponding normal stress is not an independent variable and hence neglected.
7. An axiomatic based displacement field approach is used to define the variables.
8. The non-linear variation of in-plane displacements across thickness is considered while the transverse displacement is assumed to be constant across thickness of CNTRC plate.

3.3. Basic Equations

In the present work, a rectangular CNTRC plate is considered in a Cartesian coordinate system with dimensions as a, b and h in x, y, and z directions respectively. A schematic of the plate is shown in Fig. 3.1 along with the considered distributions of CNT along the thickness direction. The CNT is assumed to be uniformly distributed (UD) as well as functionally graded (FG). Further, these FG distributions are considered as FG-V (maximum distribution of CNT at the top surface), FG-Λ (maximum distribution of CNT at the bottom surface), FG-X (maximum distribution of CNT at top and bottom surfaces while minimum at the center), and FG-O (maximum distribution of CNT at the center while the minimum at top and bottom surfaces). The middle plane (at $z = 0$) is considered as the reference plane.

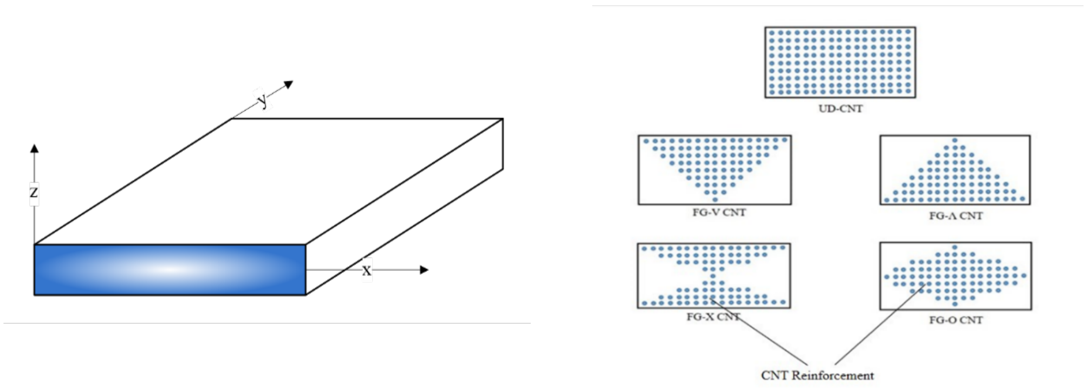

Fig. 3-1: Schematic of the CNTRC plate with CNT distributions

3.3.1. Rule of mixture

The CNT is reinforced with the matrix phase and therefore, it is important to predict the effective material properties of the resulting CNTRC plates. Generally, the effective material properties of CNT reinforced plates are evaluated by using the Mori-Tanaka scheme [98] or rule of mixture [16]. In the present study the extended rule of mixture is employed to predict the overall material properties for the FG-CNT reinforced plate. Also, the accuracy of the extended rule of mixture was discussed and compared with the Mori-Tanaka scheme for functionally graded beam as reported in Librescu *et al.* [99]. The extended rule of mixture to evaluate the homogeneous material properties is as follows [100]

$$
\begin{aligned}
E_1 &= \eta_1 V_{CNT} E_{11}^{CNT} + V_m E_m \\
\frac{\eta_2}{E_2} &= \frac{V_{CNT}}{E_{22}^{CNT}} + \frac{V_m}{E_m} \\
\frac{\eta_3}{G_{12}} &= \frac{V_{CNT}}{G_{12}^{CNT}} + \frac{V_m}{G_m} \\
\nu_{12} &= V_{CNT}^{*} \nu_{12}^{CNT} + V_m \nu^{m}
\end{aligned}
\tag{3.1}
$$

where E_1, E_2, G_{12}, and ν_{12} are the Young's modulus in longitudinal direction (x), Young's modulus in lateral direction (y), in-plane shear modulus (G_{12}) and Poisson's ratio (ν_{12}) of the resulting CNT reinforced composite. The terms E_{11}^{CNT} and E_{22}^{CNT} are the Young's moduli of CNT in longitudinal (x) and transverse (y) directions respectively, G_{12}^{CNT} is the in-plane shear modulus of the CNT, V_{CNT}^{*} is the volume fraction parameter defined in Eq. (3.2) and Eq. (3.3), and ν_{12}^{CNT} is the Poisson's ratio of CNT reinforcement. Young's modulus, shear modulus, and

Poisson's ratio of the isotropic matrix phase are designated as E_m, G_m and ν^m respectively. The volume fraction of reinforcement and matrix phase are represented by V_{CNT} and V_m respectively. The efficiency parameters η_1, η_2, and η_3 are incorporated in the extended rule of mixture to take into account the scale dependent material properties of CNTs. These efficiency parameters are dependent on the volume fraction of the CNT and are evaluated by molecular dynamics simulations [53]. The volume fraction of CNT (V_{CNT}) depends upon the choice of distribution within the matrix phase. The volume fraction of CNT is assumed to be based on the power law and given in Eq. (3.2) for considered UD configuration and FG configurations of CNT. The volume fraction is constant for UD configuration while it is a function of thickness coordinate for FG distributions. Therefore, the resulting properties for the FG-CNT reinforced composite are also a function of thickness coordinate.

$$\begin{array}{ll} V_{CNT} = V^*_{CNT} & \text{UD} \\ V_{CNT}(z) = \left(1 + 2\dfrac{z}{h}\right)V^*_{CNT} & \text{FG-V} \\ V_{CNT}(z) = \left(1 - 2\dfrac{z}{h}\right)V^*_{CNT} & \text{FG-}\Lambda \\ V_{CNT}(z) = 2\left(1 - 2\dfrac{|z|}{h}\right)V^*_{CNT} & \text{FG-O} \\ V_{CNT}(z) = 2\left(2\dfrac{|z|}{h}\right)V^*_{CNT} & \text{FG-X} \end{array} \tag{3.2}$$

Also, note that the volume fraction parameter of CNT $\left(V^*_{CNT}\right)$ in Eq. (3.2) is expressed in terms of mass fraction of CNT (w_{CNT}), density of CNT (ρ_{CNT}) and density of the matrix phase (ρ_{m}) as shown in Eq. (3.3).

$$V^*_{CNT} = \frac{w_{CNT}}{w_{CNT} + \left(\rho_{CNT}/\rho_m\right) - \left(\rho_{CNT}/\rho_m\right) w_{CNT}} \tag{3.3}$$

In the similar manner, the coefficient of thermal expansion of the resulting CNT reinforced composite in longitudinal direction (α_{11}) and transverse direction (α_{22}) is obtained using the rule of mixture and expression in the form of constituents' (reinforcement and matrix) properties. The coefficient of thermal expansions (α_{11} and α_{22}) for the CNT reinforced composite is given in Eq. (3.4)

$$\begin{aligned}\alpha_{11} &= V_{CNT}\alpha_{11}^{CNT} + V_m\alpha^m \\ \alpha_{22} &= \left(1+\nu_{12}^{CNT}\right)V_{CNT}\alpha_{22}^{CNT} + \left(1+\nu_m\right)V_m\alpha^m - \nu_{12}\alpha_{11}\end{aligned} \tag{3.4}$$

where α_{11}^{CNT}, α_{22}^{CNT} and α^m are the coefficient of thermal expansion of CNT in longitudinal and transverse direction and matrix phase, respectively. Similarly, the longitudinal (β_{11}) and transverse (β_{22}) coefficient of hygroscopic expansion of the FG-CNT reinforced plate are expressed in the form of corresponding properties of its constituents and are expressed as [95]

$$\begin{aligned}\beta_{11} &= \frac{V_{CNT}E_{11}^{CNT}C_{CNTm}\beta_{11}^{CNT} + V_m E^m \beta^m}{E_{11}\left(V_{CNT}\rho^{CNT}C_{CNTm} + V_m\rho^m\right)}\rho \\ \beta_{22} &= \frac{V_{CNT}\left(1+\nu^{CNT}\right)C_{CNTm}\beta_{22}^{CNT} + V_m\left(1+\nu^m\right)\beta^m}{V_{CNT}\rho^{CNT}C_{CNTm} + V_m\rho^m}\rho - \nu_{12}\beta_{11}\end{aligned} \tag{3.5}$$

where C_{CNTm} is the moisture concentration ratio, the terms β_{11}^{CNT} and β_{22}^{CNT} are the swelling coefficients (coefficients of hygroscopic expansion) of the CNT in longitudinal and transverse directions respectively and β^m is the coefficient of the hygroscopic expansion of the matrix phase.

3.3.2. Displacement field

The displacement based axiomatic approach is employed in the present work to depict the field variables. In this approach, the displacements are the primary variables while the strains and stresses are secondary variables. An inverse hyperbolic shear deformation theory (IHSDT) is implemented to define the displacement variables (u, v, w) in the plate domain. The in-plane displacements (u and v in x and y directions respectively) are assumed to vary non-linear across the thickness coordinate while the transverse displacement (w in z direction) is assumed to be constant across thickness accounting for the condition of plane stress. These displacement variables are defined as follows [40].

$$
\begin{aligned}
u(x,y,z,t) &= u_0(x,y,t) - z\frac{\partial w_0}{\partial x} + \left(\sinh^{-1}\left(\frac{rz}{h}\right) - z\frac{2r}{h\sqrt{r^2+4}}\right)\theta_x(x,y,t) \\
v(x,y,z,t) &= v_0(x,y,t) - z\frac{\partial w_0}{\partial y} + \left(\sinh^{-1}\left(\frac{rz}{h}\right) - z\frac{2r}{h\sqrt{r^2+4}}\right)\theta_y(x,y,t) \\
w(x,y,z,t) &= w_0(x,y,t)
\end{aligned}
\tag{3.6}
$$

where $(u_{\circ}, v_{\circ}, w_{\circ})$ are the displacements at a point on the middle plane in *x*, *y*, and *z* direction respectively and (θ_x, θ_y) are the shear rotations at the mid-plane. The parameter "*r*" is an optimization parameter and its value is assumed to be 3. By introducing a function $f(z) = g(z) + \Omega z$ such that $g(z) = \sinh^{-1}(rz/h)$ and $\Omega = -2r\big/\left(h\sqrt{r^2+4}\right)$, the present theory can be written in generalized form as indicated in Eq. (3.7).

$$
\begin{aligned}
u &= u_0 - z\frac{\partial w_0}{\partial x} + f(z)\theta_x \\
v &= v_0 - z\frac{\partial w_0}{\partial y} + f(z)\theta_y \\
w &= w_0
\end{aligned}
\tag{3.7}
$$

The function $f(z)$ is the shear strain function which is expressed as inverse hyperbolic function of thickness coordinate and chosen in such a way that it inherently satisfies the zero transverse shear conditions at top and bottom surfaces of the plate without the use of shear correction factor as required in FSDT.

3.3.3. Strain-displacement relationship

Based on small deformations, the displacement field given in Eq. (3.7) is implemented in the strains-displacement relations. The linear strain-displacement relations for normal strains $(\varepsilon_{xx}, \varepsilon_{yy})$ in-plane shear strain (γ_{xy}) and transverse shear strains $(\gamma_{xz}, \gamma_{yz})$ are expressed as follows:

$$
\{\varepsilon\}_{5\times1} = \{\varepsilon_L\}_{5\times1} + \{\varepsilon_{NL}\}_{5\times1}
\tag{3.8}
$$

$$\begin{aligned}
\varepsilon_{xx} &= \frac{\partial u}{\partial x} = \frac{\partial u_{\circ}}{\partial x} - z\frac{\partial \phi_x}{\partial x} + \left[g(z) + \Omega z\right]\frac{\partial \theta_x}{\partial x} \\
\varepsilon_{yy} &= \frac{\partial v}{\partial y} = \frac{\partial v_{\circ}}{\partial y} - z\frac{\partial \phi_y}{\partial y} + \left[g(z) + \Omega z\right]\frac{\partial \theta_y}{\partial y} \\
\gamma_{xy} &= \frac{\partial u}{\partial y} + \frac{\partial v}{\partial x} = \left(\frac{\partial u_{\circ}}{\partial y} + \frac{\partial v_{\circ}}{\partial x}\right) - z\left(\frac{\partial \phi_x}{\partial y} + \frac{\partial \phi_y}{\partial x}\right) + \left[g(z) + \Omega z\right]\left(\frac{\partial \theta_x}{\partial y} + \frac{\partial \theta_y}{\partial x}\right) \\
\gamma_{xz} &= \frac{\partial u}{\partial z} + \frac{\partial w}{\partial x} = f'(z)\theta_x \\
\gamma_{yz} &= \frac{\partial v}{\partial z} + \frac{\partial w}{\partial y} = f'(z)\theta_y
\end{aligned} \tag{3.9}$$

where $f'(z) = g'(z) + \Omega$

$$\{\varepsilon_{NL}\} = \begin{bmatrix} \frac{1}{2}\left(\frac{\partial w}{\partial x}\right)^2 & \frac{1}{2}\left(\frac{\partial w}{\partial y}\right)^2 & \frac{1}{2}\left(\frac{\partial w}{\partial x}\right)\left(\frac{\partial w}{\partial x}\right) & 0 & 0 \end{bmatrix}^T \tag{3.10}$$

It is to be noted that the linear strains are considered for static analysis; however due to the fact that buckling is essentially a non-linear phenomenon; von-Karman nonlinear strains are considered for deriving the geometric stiffness matrix in the finite element framework as given in subsection 3.5.3.

3.3.4. Constitutive relation

The matrix phase is isotropic; however, the reinforced i.e. CNT behaves orthotropic. The resulting CNT reinforced composite is therefore orthotropic in nature. Further, the material properties also vary across thickness due to the gradient of CNT distributed. The material behavior of the CNT reinforced composite is depicted by representing the constitutive relations in the framework of Generalized Hooke's law. The constitutive relation representing the stress vector $\{\sigma\}$, elastic strain vector $\{\varepsilon\}$, thermal induced strain vector $\{\varepsilon^{TH}\}$, and moisture induced strain vector $\{\varepsilon^{H}\}$ is given in Eq. (3.11).

$$\{\sigma\} = \left[Q_{ij}\right]\left(\{\varepsilon\} - \{\varepsilon^{Th}\} - \{\varepsilon^{H}\}\right) \tag{3.11}$$

The explicit form of Eq. (3.11) is presented in Eq. (3.12). The matrix $[Q_{ij}]$ is material stiffness matrix and it is depending upon the material properties of CNT reinforced composite such as Young's moduli (E_{11}, E_{22}), shear moduli (G_{12}, G_{23}, G_{23}) and Poisson's ratio (ν_{12}, ν_{21})

which vary along the thickness direction. The stress vector $\{\sigma\} = \{\sigma_{xx} \quad \sigma_{yy} \quad \tau_{xy} \quad \tau_{xz} \quad \tau_{yz}\}^T$ includes the normal stresses (σ_{xx} and σ_{yy}) in x and y direction respectively, the in-plane shear stress (τ_{xy}) and the transverse shear stresses (τ_{xz} and τ_{yz}). Similarly, the strain vector $\{\varepsilon\} = \{\varepsilon_{xx} \quad \varepsilon_{yy} \quad \gamma_{xy} \quad \gamma_{xz} \quad \gamma_{yz}\}^T$ includes the normal strains (ε_{xx} and ε_{yy}) in x and y direction respectively, the in-plane shear strain (γ_{xy}) and the transverse shear strains (γ_{xz} and γ_{yz}). The parameters ΔT and Δc represent the change in temperature and moisture concentration respectively.

$$\begin{Bmatrix} \sigma_{xx} \\ \sigma_{yy} \\ \tau_{xy} \\ \tau_{xz} \\ \tau_{yz} \end{Bmatrix} = \begin{bmatrix} Q_{11} & Q_{12} & 0 & 0 & 0 \\ Q_{12} & Q_{22} & 0 & 0 & 0 \\ 0 & 0 & Q_{66} & 0 & 0 \\ 0 & 0 & 0 & Q_{44} & 0 \\ 0 & 0 & 0 & 0 & Q_{55} \end{bmatrix} \begin{Bmatrix} \varepsilon_{xx} \\ \varepsilon_{yy} \\ \gamma_{xy} \\ \gamma_{xz} \\ \gamma_{yz} \end{Bmatrix} - \begin{Bmatrix} \alpha_{11}\Delta T \\ \alpha_{22}\Delta T \\ \alpha_{12}\Delta T \\ 0 \\ 0 \end{Bmatrix} - \begin{Bmatrix} \beta_{11}\Delta c \\ \beta_{22}\Delta c \\ \beta_{12}\Delta c \\ 0 \\ 0 \end{Bmatrix} \tag{3.12}$$

The coefficients of the material stiffness matrix are represented as follows:

$$\begin{gathered} Q_{11} = \frac{E_{11}(z)}{1-\nu_{12}\nu_{21}}, \quad Q_{22} = \frac{E_{22}(z)}{1-\nu_{12}\nu_{21}}, \quad Q_{12} = Q_{21} = \frac{\nu_{12}E_{22}(z)}{1-\nu_{12}\nu_{21}}, \\ Q_{44} = G_{12}, \qquad Q_{44} = G_{13}, \qquad Q_{44} = G_{23}. \end{gathered} \tag{3.13}$$

The temperature induced strain is the function of coefficients of thermal expansion (α_{11}, α_{22}, and α_{12}) and the change in temperature field (ΔT). Similarly, the moisture induced strain is the function of coefficients of moisture expansion (β_{11}, β_{22}, and β_{12}) and change in moisture concentration (Δc). The temperature field is defined in Eq. (3.14) in terms of constant temperature (T_1), linearly varying temperature (T_2) and non-linearly varying temperature (T_3). In the similar manner, c_1, c_2, and c_3 represent the constant, linearly and non-linearly varying moisture concentration across the thickness of the FG-CNTR plate and given in Eq. (3.15). The nonlinear dependency of the temperature and moisture concentration is considered in consistency with the displacement field.

$$\Delta T = T_1 + \frac{z}{h}T_2 + \frac{g(z)}{h}T_3 \tag{3.14}$$

$$\Delta c = c_1 + \frac{z}{h}c_2 + \frac{g(z)}{h}c_3 \tag{3.15}$$

3.4. Analytical Formulation: Static, Buckling and Free vibration

The governing differential equations are derived by employing the principle of virtual work in this section. These differential equations are solved in the exact manner for specific boundary conditions and the algebraic system of equations is then obtained for static, buckling and free vibration response of CNT reinforced composite plates.

3.4.1. Governing differential equations

In order to obtain the governing differential equation for the structural analysis of CNT reinforced composite plates, the principle of virtual work is followed. The principle is stated in terms of virtual kinetic energy (δT), virtual strain energy (δU), and virtual work done due to applied forces (δV) as presented in Eq. (3.16).

$$\int_{t_1}^{t_2} \delta\left(T-U\right)dt+\int_{t_1}^{t_2} \delta V dt=0 \tag{3.16}$$

The respective virtual energy and virtual work terms are obtained as follows.

$$\delta T=\int_{\Omega_0}\left(\int_{-\frac{h}{2}}^{\frac{h}{2}} \rho\left[\ddot{u}\delta u+\ddot{v}\delta v+\ddot{w}\delta w\right]dz\right)dxdy \tag{3.17}$$

$$\delta U=\int_{\Omega_0}\left\{\int_{-\frac{h}{2}}^{\frac{h}{2}}\left[\sigma_{xx}\delta\varepsilon_{xx}+\sigma_{yy}\delta\varepsilon_{yy}+\tau_{xy}\delta\gamma_{xy}+\tau_{yz}\delta\gamma_{yz}+\tau_{xz}\delta\gamma_{xz}\right]dz\right\}dxdy \tag{3.18}$$

$$\delta V=\int_{S}\left(q\delta w_0+N_{11}\frac{\delta w_0}{\delta x}\frac{\delta w_0}{\delta x}+N_{22}\frac{\delta w_0}{\delta y}\frac{\delta w_0}{\delta y}\right)dxdy \tag{3.19}$$

The virtual terms in Eq. (3.17) to (3.19) are expressed in the form of virtual displacement by employing the strain displacement relations (Eq. (3.9)) and these terms are solved following the principles of variational calculus. The expression of virtual kinetic energy (δT), virtual strain energy (δU) and virtual work done (δV) are substituted in the principle of virtual work statement in Eq. (3.16). The fundamental lemma of calculus of variation is applied and the coefficients of variations of primary variables are obtained and equated to zero following the condition of principle of virtual work. In this process, the Euler-Lagrange differential equations are obtained in the form of stress resultants, moment resultants, and higher order moment results. These Euler-Lagrange differential equations are given in Eq. (3.20). Since there are five primary variables (u_0, v_0, w_0, θ_x, and θ_y), five differential equations are obtained.

$$
\begin{aligned}
&\frac{\partial N_{xx}}{\partial x}+\frac{\partial N_{xy}}{\partial y}=\frac{\partial N_{xx}^{T}}{\partial x}+\frac{\partial N_{xy}^{T}}{\partial y}+\frac{\partial N_{xx}^{c}}{\partial x}+\frac{\partial N_{xy}^{c}}{\partial y}+I_0\ddot{u}_0-I_1\frac{\partial \ddot{w}_0}{\partial x}+I_3\ddot{\theta}_x\\
&\frac{\partial N_{xy}}{\partial x}+\frac{\partial N_{yy}}{\partial y}=\frac{\partial N_{yy}^{T}}{\partial y}+\frac{\partial N_{xy}^{T}}{\partial x}+\frac{\partial N_{yy}^{c}}{\partial y}+\frac{\partial N_{xy}^{c}}{\partial x}+I_0\ddot{v}_0-I_1\frac{\partial \ddot{w}_0}{\partial y}+I_3\ddot{\theta}_y\\
&\frac{\partial^2 M_{xx}}{\partial x^2}+2\frac{\partial^2 M_{xy}}{\partial x\partial y}+\frac{\partial^2 M_{yy}}{\partial y^2}+q+N_{11}\frac{\partial^2 w_0}{\partial x^2}+N_{22}\frac{\partial^2 w_0}{\partial y^2}=\frac{\partial^2 M_{xx}^{T}}{\partial x^2}\\
&\qquad+\frac{\partial^2 M_{yy}^{T}}{\partial y^2}+2\frac{\partial^2 M_{xy}^{T}}{\partial x\partial y}+\frac{\partial^2 M_{xx}^{c}}{\partial x^2}+\frac{\partial^2 M_{yy}^{c}}{\partial y^2}+2\frac{\partial^2 M_{xy}^{c}}{\partial x\partial y}\\
&\qquad\qquad+I_1\left(\frac{\partial \ddot{u}_0}{\partial x}+\frac{\partial \ddot{v}_0}{\partial y}\right)-I_2\left(\frac{\partial^2 \ddot{w}_0}{\partial x^2}+\frac{\partial^2 \ddot{w}_0}{\partial y^2}\right)+I_4\left(\frac{\partial \ddot{\theta}_x}{\partial x}+\frac{\partial \ddot{\theta}_y}{\partial y}\right)+I_0\ddot{w}_0\\
&\Omega\frac{\partial M_{xx}}{\partial x}+\frac{\partial P_{xx}}{\partial x}+\Omega\frac{\partial M_{xy}}{\partial y}+\frac{\partial P_{xy}}{\partial y}-\Omega Q_1-K_1=\Omega\frac{\partial M_{xx}^{T}}{\partial x}+\frac{\partial P_{xx}^{T}}{\partial x}+\Omega\frac{\partial M_{xy}^{T}}{\partial y}\\
&\qquad+\frac{\partial P_{xy}^{T}}{\partial y}+\Omega\frac{\partial M_{xx}^{c}}{\partial x}+\frac{\partial P_{xx}^{c}}{\partial x}+\Omega\frac{\partial M_{xy}^{c}}{\partial y}+\frac{\partial P_{xy}^{c}}{\partial y}+I_3\ddot{u}_0-I_4\frac{\partial \ddot{w}_0}{\partial x}+I_5\ddot{\theta}_x\\
&\Omega\frac{\partial M_{xy}}{\partial x}+\frac{\partial P_{xy}}{\partial x}+\Omega\frac{\partial M_{yy}}{\partial y}+\frac{\partial P_{yy}}{\partial y}-\Omega Q_2-K_2=\Omega\frac{\partial M_{yy}^{T}}{\partial y}+\frac{\partial P_{yy}^{T}}{\partial y}+\Omega\frac{\partial M_{xy}^{T}}{\partial x}\\
&\qquad+\frac{\partial P_{xy}^{T}}{\partial x}+\Omega\frac{\partial M_{yy}^{c}}{\partial y}+\frac{\partial P_{yy}^{c}}{\partial y}+\Omega\frac{\partial M_{xy}^{c}}{\partial x}+\frac{\partial P_{xy}^{c}}{\partial x}+I_3\ddot{v}_0-I_4\frac{\partial \ddot{w}_0}{\partial y}+I_5\ddot{\theta}_y
\end{aligned}
\tag{3.20}
$$

where N, M and P are the resultants of in-plane stresses, moments, and higher order moments. The parameters Q and K represent the resultants of transverse shear stresses and corresponding moments. These stress and moment resultant terms also appear due the effect of temperature as well as due to moisture concentration. The superscript 'T' and 'c' are indicated on the corresponding stress and moment resultant terms due to thermal effect and moisture effect respectively. Also, the terms appearing as I_0, I_1, I_2, I_3, I_4, and I_5 are inertia terms. The stresses and moment resultants and inertia terms mentioned in the Eq. (3.20) are expressed as integrals across thickness of CNTRC plate and defined as follows.

$$\begin{bmatrix} N_{xx} & M_{xx} & P_{xx} \\ N_{yy} & M_{yy} & P_{yy} \\ N_{xy} & M_{xy} & P_{xy} \end{bmatrix} = \int_{-\frac{h}{2}}^{\frac{h}{2}} \begin{Bmatrix} \sigma_{xx} \\ \sigma_{yy} \\ \tau_{xy} \end{Bmatrix} \begin{bmatrix} 1 & z & g(z) \end{bmatrix} dz$$

$$\begin{bmatrix} Q_2 & K_2 \\ Q_1 & K_1 \end{bmatrix} = \int_{-\frac{h}{2}}^{\frac{h}{2}} \begin{Bmatrix} \tau_{yz} \\ \tau_{xz} \end{Bmatrix} \begin{bmatrix} 1 & g'(z) \end{bmatrix} dz \tag{3.21}$$

$$\begin{bmatrix} I_0 & I_1 & I_2 & I_3 & I_4 & I_5 \end{bmatrix} = \int_{-\frac{h}{2}}^{\frac{h}{2}} \rho \begin{bmatrix} 1 & z & z^2 & f(z) & z.f(z) & \left(f(z)\right)^2 \end{bmatrix} dz \tag{3.22}$$

$$\begin{bmatrix} N^T_{xx} & M^T_{xx} & P^T_{xx} \\ N^T_{yy} & M^T_{yy} & P^T_{yy} \\ N^T_{xy} & M^T_{xy} & P^T_{xy} \end{bmatrix} = \int_{-\frac{h}{2}}^{\frac{h}{2}} [Q] \begin{Bmatrix} \alpha_{xx} \\ \alpha_{yy} \\ \alpha_{xy} \\ 0 \\ 0 \end{Bmatrix} \begin{bmatrix} 1 & z & f(z) \end{bmatrix} \Delta T dz \tag{3.23}$$

$$\begin{bmatrix} N^c_{xx} & M^c_{xx} & P^c_{xx} \\ N^c_{yy} & M^c_{yy} & P^c_{yy} \\ N^c_{xy} & M^c_{xy} & P^c_{xy} \end{bmatrix} = \int_{-\frac{h}{2}}^{\frac{h}{2}} [Q] \begin{Bmatrix} \beta_{xx} \\ \beta_{yy} \\ \beta_{xy} \\ 0 \\ 0 \end{Bmatrix} \begin{bmatrix} 1 & z & f(z) \end{bmatrix} \Delta c dz \tag{3.24}$$

The equations obtained so far are in the form of resultant stress, moments and higher order moments; however, since the primary variables are displacements, it is required to obtain the governing equations in terms of primary variables. For this purpose, the stress-strain relations (Eq. (3.7)) and strain-displacement relations (Eq. (3.9)) are employed in Eq. (3.21) to Eq. (3.24). Further, the integral terms are defined as matrices such as extensional stiffness matrix, bending stiffness matrix, etc. These matrices are defined as [***A***], [***B***], [***D***], [***E***], [***F***], [***H***], [***K***], and [***L***] and obtained by performing the integration as mentioned in Eq. (3.22) and Eq. (3.23).

$$\begin{bmatrix} A_{ij} & B_{ij} & D_{ij} & E_{ij} & F_{ij} & H_{ij} \end{bmatrix} = \int_{-\frac{h}{2}}^{\frac{h}{2}} \begin{bmatrix} Q_{ij} \end{bmatrix} \begin{bmatrix} 1 & z & z^2 & g(z) & zg(z) & \left(g(z)\right)^2 \end{bmatrix} dz \tag{3.25}$$

where i and j are 1, 2, 4, 5, 6.

$$\begin{bmatrix} K_{ij} & L_{ij} \end{bmatrix} = \int_{-\frac{h}{2}}^{\frac{h}{2}} [Q]\begin{bmatrix} g'(z) & \left(g'(z)\right)^2 \end{bmatrix} dz \quad \text{for } i,j = 4,5 \tag{3.26}$$

Also, the stress and moment resultant terms due to thermal effect (N^T, M^T, and P^T) and due to moisture concentration (N^T, M^T, and P^T) are simplified with the help of stiffness integrals defined in Eq. (3.25) and Eq. (3.26). The superscript '*T*' and '*c*' indicate the corresponding terms due to thermal effect and moisture effect respectively.

$$\begin{bmatrix} A_i^T & B_i^T & D_i^T & B_i^{AT} & D_i^{AT} & F_i^{AT} \end{bmatrix} = \int_{\frac{-h}{2}}^{\frac{h}{2}} [Q] \begin{Bmatrix} \alpha_{11} \\ \alpha_{22} \\ \alpha_{12} \\ 0 \\ 0 \end{Bmatrix} \times \begin{Bmatrix} 1 & z & z^2 & f(z) & z.f(z) & (f(z))^2 \end{Bmatrix} dz \tag{3.27}$$

$$\begin{bmatrix} A_i^C & B_i^C & D_i^C & B_i^{AC} & D_i^{AC} & F_i^{AC} \end{bmatrix} = \int_{\frac{-h}{2}}^{\frac{h}{2}} [Q] \begin{Bmatrix} \beta_{11} \\ \beta_{22} \\ \beta_{12} \\ 0 \\ 0 \end{Bmatrix} \times \begin{Bmatrix} 1 & z & z^2 & f(z) & z.f(z) & (f(z))^2 \end{Bmatrix} dz \tag{3.28}$$

The stress and moment resultant terms are simplified by implementing the stress-strain relations (Eq. (3.7)), strain-displacement relations (Eq. (3.9)), and the integrals as defined in Eq. (3.21) to Eq. (3.28) and these terms are substituted in Eq. (3.20). In this process, governing differential equations are obtained in the form of primary displacement variables and given in Eq. (3.29).

$$
\begin{aligned}
&A_{11}\left(\frac{\partial^2 u_0}{\partial x^2}\right)+B_{11}\left(\Omega\frac{\partial^2\theta_x}{\partial x^2}-\frac{\partial^3 w_0}{\partial x^3}\right)+E_{11}\left(\frac{\partial^2\theta_x}{\partial x^2}\right)+A_{12}\left(\frac{\partial^2 v_0}{\partial x\partial y}\right)\\
&+B_{12}\left(\Omega\frac{\partial^2\theta_y}{\partial x\partial y}-\frac{\partial^3 w_0}{\partial x\partial y^2}\right)+E_{12}\left(\frac{\partial^2\theta_y}{\partial x\partial y}\right)+A_{66}\left(\frac{\partial^2 u_0}{\partial y^2}+\frac{\partial^2 v_0}{\partial x\partial y}\right)+\\
&B_{66}\left(\Omega\left(\frac{\partial^2\theta_x}{\partial x^2}+\frac{\partial^2\theta_y}{\partial x\partial y}\right)-2\left(\frac{\partial^3 w_0}{\partial x\partial y^2}\right)\right)+E_{66}\left(\frac{\partial^2\theta_x}{\partial x^2}+\frac{\partial^2\theta_y}{\partial x\partial y}\right)=\\
&A_1^T\left(\frac{\partial T_1}{\partial x}\right)+B_1^T\left(\frac{\partial T_2}{\partial x}\right)+B_1^{AT}\left(\frac{\partial T_3}{\partial x}\right)+\Omega B_1^T\left(\frac{\partial T_3}{\partial x}\right)
\end{aligned}
$$

$$
\begin{aligned}
&A_{22}\left(\frac{\partial^2 v_0}{\partial x^2}\right)+B_{22}\left(\Omega\frac{\partial^2\theta_y}{\partial y^2}-\frac{\partial^3 w_0}{\partial y^3}\right)+E_{22}\left(\frac{\partial^2\theta_y}{\partial y^2}\right)+A_{12}\left(\frac{\partial^2 u_0}{\partial x\partial y}\right)+B_{12}\left(\Omega\frac{\partial^2\theta_x}{\partial x\partial y}-\frac{\partial^3 w_0}{\partial x^2\partial y}\right)\\
&+E_{12}\left(\frac{\partial^2\theta_x}{\partial x\partial y}\right)+A_{66}\left(\frac{\partial^2 u_0}{\partial x\partial y}+\frac{\partial^2 v_0}{\partial x^2}\right)+B_{66}\left(\Omega\left(\frac{\partial^2\theta_x}{\partial x\partial y}+\frac{\partial^2\theta_y}{\partial x^2}\right)-2\left(\frac{\partial^3 w_0}{\partial x^2\partial y}\right)\right)\\
&+E_{66}\left(\frac{\partial^2\theta_x}{\partial x\partial y}+\frac{\partial^2\theta_y}{\partial x^2}\right)=A_2^T\left(\frac{\partial T_1}{\partial y}\right)+B_2^T\left(\frac{\partial T_2}{\partial y}\right)+B_2^{AT}\left(\frac{\partial T_3}{\partial y}\right)+\Omega B_2^T\left(\frac{\partial T_3}{\partial y}\right)
\end{aligned}
$$

$$
\begin{aligned}
&B_{11}\left(\frac{\partial^3 u_0}{\partial x^3}\right)+D_{11}\left(\Omega\frac{\partial^3\theta_x}{\partial x^3}-\frac{\partial^4 w_0}{\partial x^4}\right)+F_{11}\left(\frac{\partial^3\theta_x}{\partial x^3}\right)+B_{12}\left(\frac{\partial^3 u_0}{\partial x\partial y^2}+\frac{\partial^3 v_0}{\partial x^2\partial y}\right)\\
&+D_{12}\left(\Omega\left(\frac{\partial^3\theta_y}{\partial x^2\partial y}+\frac{\partial^3\theta_x}{\partial x\partial y^2}\right)-2\frac{\partial^4 w_0}{\partial x^2\partial y^2}\right)+F_{12}\left(\frac{\partial^3\theta_y}{\partial x^2\partial y}+\frac{\partial^3\theta_x}{\partial x\partial y^2}\right)+B_{22}\left(\frac{\partial^3 v_0}{\partial y^3}\right)\\
&D_{22}\left(\Omega\frac{\partial^3\theta_y}{\partial y^3}-\frac{\partial^4 w_0}{\partial y^4}\right)+F_{22}\left(\frac{\partial^3\theta_y}{\partial y^3}\right)+2B_{66}\left(\frac{\partial^3 u_0}{\partial x\partial y^2}+\frac{\partial^3 v_0}{\partial x^2\partial y}\right)\\
&+2D_{66}\left(\Omega\left(\frac{\partial^3\theta_y}{\partial x^2\partial y}+\frac{\partial^3\theta_x}{\partial x\partial y^2}\right)-2\frac{\partial^4 w_0}{\partial x^2\partial y^2}\right)+2F_{66}\left(\frac{\partial^3\theta_y}{\partial x^2\partial y}+\frac{\partial^3\theta_x}{\partial x\partial y^2}\right)+q\\
&=B_1^T\left(\frac{\partial^2 T_1}{\partial x^2}\right)+D_1^T\left(\frac{\partial^2 T_2}{\partial x^2}\right)+D_1^{AT}\left(\frac{\partial^2 T_3}{\partial^2 x}\right)+\Omega D_1^T\left(\frac{\partial^2 T_3}{\partial^2 x}\right)\\
&+B_2^T\left(\frac{\partial^2 T_1}{\partial y^2}\right)+D_2^T\left(\frac{\partial^2 T_2}{\partial y^2}\right)+D_2^{AT}\left(\frac{\partial^2 T_3}{\partial y^2}\right)+\Omega D_2^T\left(\frac{\partial^2 T_3}{\partial y^2}\right)
\end{aligned}
$$

$$
\begin{aligned}
&\left(\Omega B_{11}+E_{11}\right)\left(\frac{\partial^2 u_0}{\partial x^2}\right)+\left(\Omega D_{11}+F_{11}\right)\left(\Omega\frac{\partial^2\theta_x}{\partial x^2}-\frac{\partial^3 w_0}{\partial x^3}\right)+\left(\Omega F_{11}+H_{11}\right)\left(\frac{\partial^2\theta_x}{\partial x^2}\right)\\
&+\left(\Omega B_{12}+E_{12}\right)\left(\frac{\partial^2 v_0}{\partial x\partial y}\right)+\left(\Omega D_{12}+F_{12}\right)\left(\Omega\frac{\partial^2\theta_y}{\partial x\partial y}-\frac{\partial^3 w_0}{\partial x\partial y^2}\right)+\left(\Omega F_{12}+H_{12}\right)\left(\frac{\partial^2\theta_y}{\partial x\partial y}\right)\\
&+\left(\Omega B_{66}+E_{66}\right)\left(\frac{\partial^2 u_0}{\partial y^2}+\frac{\partial^2 v_0}{\partial x\partial y}\right)+\left(\Omega D_{66}+F_{66}\right)\left(\Omega\left(\frac{\partial^2\theta_x}{\partial x^2}+\frac{\partial^2\theta_y}{\partial x\partial y}\right)-2\left(\frac{\partial^3 w_0}{\partial x\partial y^2}\right)\right)\\
&+\left(\Omega F_{66}+H_{66}\right)\left(\frac{\partial^2\theta_x}{\partial x^2}+\frac{\partial^2\theta_y}{\partial x\partial y}\right)-\left(\Omega^2 A_{55}+2\Omega K_{55}+L_{55}\right)\theta_x=\left(\Omega B_1^T+B_1^{AT}\right)\left(\frac{\partial T_1}{\partial x}\right)\\
&+\left(\Omega D_1^T+D_1^{AT}\right)\left(\frac{\partial T_2}{\partial x}\right)+\left(\Omega D_1^{AT}+F_1^{AT}\right)\left(\frac{\partial T_3}{\partial x}\right)+\Omega\left(\Omega D_1^T+D_1^{AT}\right)\left(\frac{\partial T_3}{\partial x}\right)
\end{aligned}
$$

$$
\begin{aligned}
&\left(\Omega B_{22}+E_{22}\right)\left(\frac{\partial^2 v_0}{\partial x^2}\right)+\left(\Omega D_{22}+F_{22}\right)\left(\Omega\frac{\partial^2\theta_y}{\partial y^2}-\frac{\partial^3 w_0}{\partial y^3}\right)+\left(\Omega F_{22}+H_{22}\right)\left(\frac{\partial^2\theta_y}{\partial y^2}\right)\\
&+\left(\Omega B_{12}+E_{12}\right)\left(\frac{\partial^2 u_0}{\partial x\partial y}\right)+\left(\Omega D_{12}+F_{12}\right)\left(\Omega\frac{\partial^2\theta_x}{\partial x\partial y}-\frac{\partial^3 w_0}{\partial x^2\partial y}\right)+\left(\Omega F_{12}+H_{12}\right)\left(\frac{\partial^2\theta_x}{\partial x\partial y}\right)\\
&+\left(\Omega B_{66}+E_{66}\right)\left(\frac{\partial^2 u_0}{\partial x\partial y}+\frac{\partial^2 v_0}{\partial x^2}\right)+\left(\Omega D_{66}+F_{66}\right)\left(\Omega\left(\frac{\partial^2\theta_x}{\partial x\partial y}+\frac{\partial^2\theta_y}{\partial x^2}\right)-2\left(\frac{\partial^3 w_0}{\partial x^2\partial y}\right)\right)\\
&+\left(\Omega F_{66}+H_{66}\right)\left(\frac{\partial^2\theta_x}{\partial x\partial y}+\frac{\partial^2\theta_y}{\partial x^2}\right)-\left(\Omega^2 A_{44}+2\Omega K_{44}+L_{44}\right)\theta_y=\left(\Omega B_2^T+B_2^{AT}\right)\left(\frac{\partial T_1}{\partial y}\right)\\
&+\left(\Omega D_2^T+D_2^{AT}\right)\left(\frac{\partial T_2}{\partial y}\right)+\left(\Omega D_2^{AT}+F_2^{AT}\right)\left(\frac{\partial T_3}{\partial y}\right)+\Omega\left(\Omega D_2^T+D_2^{AT}\right)\left(\frac{\partial T_3}{\partial y}\right)
\end{aligned}
\tag{3.29}
$$

The above equations are higher order coupled partial differential equations and govern the structural response of CNTRC plates in a hygro-thermal environment.

3.4.2. Solution Methodology: Navier solution

In order to obtain the response of the structure and ensure the accuracy and applicability of the IHSDT for CNTRC plates, it is important that the governing system be solved in the exact manner. It is noted that the governing equations are higher order coupled differential equations whose solution will require the satisfaction of boundary conditions. However, these equations cannot be solved in the closed form for arbitrary boundary conditions. Therefore, a simplified case of boundary conditions i.e. all edges simply supported (SSSS) is considered. The boundary conditions associated with SSSS conditions are given in Eq. (3.30).

$$
\begin{aligned}
&v_0 = w_0 = \theta_y = N_{xx} = M_{xx} = 0 \ \text{ at edges } x = 0,\ a \\
&u_0 = w_0 = \theta_x = N_{yy} = M_{yy} = 0 \ \text{ at edges } y = 0,\ b
\end{aligned}
\tag{3.30}
$$

The analytical solution of Navier type is assumed which inherently satisfies the boundary conditions for SSSS configuration. The utility of the analytical solution restricts its applicability to only SSSS conditions; however, provides the solution which is free from any computational error. The assumed solution is given in Eq. (3.31)

$$
\begin{aligned}
u_0 &= \sum_{m=1}^{\infty}\sum_{n=1}^{\infty} U_{mn} e^{i\omega t} \cos(\alpha x)\sin(\beta y) \\
v_0 &= \sum_{m=1}^{\infty}\sum_{n=1}^{\infty} V_{mn} e^{i\omega t} \sin(\alpha x)\cos(\beta y) \\
w_0 &= \sum_{m=1}^{\infty}\sum_{n=1}^{\infty} W_{mn} e^{i\omega t} \sin(\alpha x)\sin(\beta y) \\
\theta_x &= \sum_{m=1}^{\infty}\sum_{n=1}^{\infty} X_{mn} e^{i\omega t} \cos(\alpha x)\sin(\beta y) \\
\theta_y &= \sum_{m=1}^{\infty}\sum_{n=1}^{\infty} Y_{mn} e^{i\omega t} \sin(\alpha x)\cos(\beta y) \\
\alpha &= \frac{m\pi}{a}, \beta = \frac{n\pi}{b}
\end{aligned}
\tag{3.31}
$$

where U_{mn}, V_{mn}, W_{mn}, X_{mn}, and Y_{mn} are the constant coefficients to be determined. In the similar manner, the transverse mechanical load, thermal load and moisture concentration are represented in terms of series solution as follows:

$$
\begin{aligned}
q &= \sum_{m=1}^{\infty}\sum_{n=1}^{\infty} q_{mn}\sin(\alpha x)\sin(\beta y)\\
T_1 &= \sum_{m=1}^{\infty}\sum_{n=1}^{\infty} \overline{T}_{1mn}\sin(\alpha x)\sin(\beta y)\\
T_2 &= \sum_{m=1}^{\infty}\sum_{n=1}^{\infty} \overline{T}_{2mn}\sin(\alpha x)\sin(\beta y)\\
T_3 &= \sum_{m=1}^{\infty}\sum_{n=1}^{\infty} \overline{T}_{3mn}\sin(\alpha x)\sin(\beta y)\\
c_1 &= \sum_{m=1}^{\infty}\sum_{n=1}^{\infty} \overline{c}_{1mn}\sin(\alpha x)\sin(\beta y)\\
c_2 &= \sum_{m=1}^{\infty}\sum_{n=1}^{\infty} \overline{c}_{2mn}\sin(\alpha x)\sin(\beta y)\\
c_3 &= \sum_{m=1}^{\infty}\sum_{n=1}^{\infty} \overline{c}_{3mn}\sin(\alpha x)\sin(\beta y)
\end{aligned}
\tag{3.32}
$$

where $qmn, \overline{T}_{1mn}, \overline{T}_{2mn}, \overline{T}_{3mn}, \overline{c}_{1mn}, \overline{c}_{2mn}$, and $\overline{c}_{3mn}$ are the applied mechanical loading, temperature and moisture concentration. For sinusoidal (SSL) mechanical load, $q_{mn} = q_0$ while for uniformly distributed load, $q_{mn} = 16q_0\pi^2/mn$. The assumed solution (Eq. (3.31)) in the governing differential equations (Eq. (3.29)). Note that the assumed solution possesses trigonometric terms and while differentiating partially as required, these terms vanish and a set of five algebraic equations is obtained in the process. The general system of algebraic equation may be written as:

$$
\left[R - \lambda G - \omega^2 M\right]\{\Delta\} = \{F_C\} \tag{3.32}
$$

The above system of equation contains stiffness matrix (***R***), geometric stiffness matrix (***G***), mass matrix (***M***), buckling parameter (λ), natural frequency (ω), vector of unknown coefficients $\{\Delta\} = \{U_{mn} \quad V_{mn} \quad W_{mn} \quad X_{mn} \quad Y_{mn}\}^T$ and combined load vector (mechanical, thermal and moisture concentration), $\{F_c\}$. These matrices and vectors are defined in Appendix A. The above system is classified for particular structural analysis such as static analysis, buckling analysis and free vibration analysis.

Static analysis: In the context of static analysis, the CNTRC plate is assumed to be subjected to transverse mechanical loads (SSL as well as UDL) along with the hygro-thermal loads.

Therefore, for such analyses, the geometric stiffness matrix and mass matrix in Eq. (3.32) will vanish and the algebraic system for such analysis is reduced and shown in Eq. (3.33).

$$[R]\{\Delta\}=\{F_C\} \tag{3.33}$$

The above system is solved by performing the matrix inversion and hence the constant coefficients $\{\Delta\}=\{U_{mn} \quad V_{mn} \quad W_{mn} \quad X_{mn} \quad Y_{mn}\}^T$ are thus obtained. These constant coefficients are substituted in the assumed solution to yield the primary variables defined at the middle plane (u_0, v_0, w_0, θ_x, and θ_y). The displacement at any point in the CNTRC plate domain is obtained using the IHSDT. Further, use of strain-displacement relations provides the strains which are employed in the constitutive relation to yield the corresponding stresses. The transverse deflection and the stresses are obtained at the critical points.

Buckling analysis: The CNTRC plate is assumed to be subjected to axial compressive forces alone. Therefore, in this context, the mass matrix and the load vector in Eq. (3.32) will vanish. The simplified system of equations is represented in Eq. (3.34).

$$[R-\lambda G]\{\Delta\}=0 \tag{3.34}$$

It should be noted that the above system is mathematically an eigen-value problem wherein the eigenvalues represent the buckling load parameters with minimum eigen-value representing the critical buckling load. The buckling analysis is carried out with uniaxial compression as well as biaxial compression.

Free vibration analysis: In the context of free vibration analysis, the CNTRC plate is assumed to be under the effect of its own inertia and hence the other forces are neglected implying that geometric stiffness matrix and the load vector appearing in Eq. (3.32) will vanish. The mathematical system in the framework of free vibration analysis will thus reduce to Eq. (3.35)

$$\left[R-\omega^2 M\right]\{\Delta\}=0 \tag{3.35}$$

Similar to the buckling analysis problem, it should be noted that the above system is mathematically an eigen-value problem wherein the eigenvalues represent the frequency parameters with minimum eigen-value representing the fundamental frequency.

3.5. Finite Element Formulation: Static, Buckling and Free vibration

The formulation presented in the preceding section and the employed solution methodology is restricted to simply supported boundary conditions of the CNT reinforced composite plate. Though the developed formulation is applicable for the specific case, it provides a solution in the analytical form and hence unconfined to any computational error. This is also paramount from the viewpoint of confirming the rationality of the IHSDT for FG-CNTRC plates. Nonetheless, the numerical solutions are predominant with the rise in computational resources as well as complex geometry and boundary conditions. Consequently, in the present work, numerical solutions for the propounded IHSDT for FG-CNTRC plates are established in the context of generalized finite element analysis and hence the pertinence of the model is perceived for general boundary conditions.

3.5.1. Continuity requirement

The displacement field defined in Eq. (3.7) requires C^1 continuity in order to model in the framework of the finite element method (FEM) due to presence of first order derivatives of the mid-plane transverse displacement in the displacement field. However, the C^1 continuity needs more computation power at the expense of computational time. Therefore, it becomes favorable to opt for C^0 continuity. In order to opt for the C^0 continuous element, separate primary variables (additional two new degrees of freedom) are introduced in the displacement field. Therefore, the displacement field is redefined and modified as:

$$\begin{aligned} u &= u_\circ - z\phi_x + f(z)\theta_x \\ v &= v_\circ - z\phi_y + f(z)\theta_y \\ w &= w_\circ \end{aligned} \tag{3.36}$$

The additional variables φ_x and φ_y are defined as follows.

$$\phi_x = \frac{\partial w_0}{\partial x} \text{ and } \phi_y = \frac{\partial w_0}{\partial y} \tag{3.37}$$

It is to be noted that these additional variables will not contribute towards the overall energy of the system and hence the following conditions are imposed in the energy formulation of the forthcoming section with the help of a penalty parameter.

$$\phi_x - \frac{\partial w_0}{\partial x} = 0 \text{ and } \phi_y - \frac{\partial w_0}{\partial y} = 0 \tag{3.38}$$

As a consequence of introducing the variables, the number of primary degrees of freedom are now revised to 7 which are represented in the vector as given in Eq. (3.39)

$$\{q\} = \{u_0 \quad v_0 \quad w_0 \quad \theta_x \quad \theta_y \quad \phi_x \quad \phi_y\}^T \tag{3.39}$$

3.5.2. *Selection of element*

In the context of finite element method, the plate is discretized with elements which have nodes at which the field variables or degrees of freedom are defined. The CNTRC plate is discretized with the eight noded iso-parametric serendipity element. The element considered is biquadratic quadrilateral. The element considered along with its nodal information is shown in Fig. 3.2. Since the number of field variables in the viewpoint of C^0 requirement is 7, the nodal degrees of freedom is 7; thus making the elemental degrees of freedom as 56. The chosen element belongs to the Lagrange elements and the shape functions for i^{th} node of the considered element are given in Eq. (3.40).

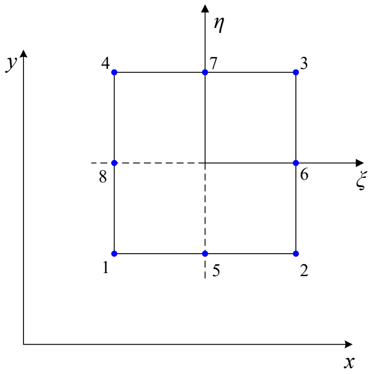

Fig. 3-2: The configuration of eight-noded finite element

It is to be noted that the element is considered in ξ-η coordinate system as shown in Fig. 3.2 while the CNTRC plate is in the *x*-*y* coordinate system. Therefore, the shape functions are also defined in ξ-η coordinates.

$$N_i = \begin{cases} \frac{1}{4}(1+\xi\xi_i)(1+\eta\eta_i)(\xi\xi_i+\eta\eta_i-1) & \text{for} \quad i=1,2,3,4 \\ \frac{1}{2}(1-\xi^2)(1+\eta\eta_i) & \text{for} \quad i=5,7 \\ \frac{1}{2}(1-\eta^2)(1+\xi\xi_i) & \text{for} \quad i=6,8 \end{cases} \tag{3.40}$$

where N_i represents the shape function at the i^{th} node. Due to consideration of the serendipity element, the field variables and geometry are defined by the same shape function. Accordingly, the field variable, q and the geometry of the element are defined in terms of eight noded shape function of each node of the element as:

$$q = \sum_{i=1}^{8} N_i q_i \text{ and } \varsigma = \sum_{i=1}^{8} N_i \varsigma_i \tag{3.41}$$

where q denotes the generalized field variable, q_i denotes the corresponding value of the field variable at i^{th} node of the element. Similarly ς denotes the generalized geometrical coordinate and ς_i denotes the corresponding value of geometrical coordinate at i^{th} node of the element.

3.5.3. Derivations of associated strain energies and work done

In the framework of finite element analysis, the elemental strain energy due to linear strains contributing towards elastic stiffness matrix [$\boldsymbol{K}^{(e)}$], elemental strain energy due to non-linear strains contributing towards geometric stiffness matrix [$\boldsymbol{K_G}^{(e)}$], elemental strain energy due to artificial variables contributing towards artificial stiffness matrix [$\boldsymbol{K_c}^{(e)}$], elemental kinetic energy contributing towards mass matrix [$\boldsymbol{M}^{(e)}$], elemental work done due to hygro-thermo-mechanical loads contributing towards load vector {$\boldsymbol{F}^{(e)}$} are derived. These elemental matrices and vectors are then assembled over the CNTRC plate domain to yield the corresponding global matrices and vectors $\left([K],\ [K_G],\ [K_c],\ [M], \text{ and } [F]\right)$.

Strain energy due to linear strains: The linear strains as in Eq. (3.9) are employed and the strain components $\{\varepsilon\} = \begin{bmatrix} \varepsilon_{xx} & \varepsilon_{yy} & \gamma_{xy} & \gamma_{yz} & \gamma_{xz} \end{bmatrix}^T$ are expressed in the form of generalized strains $\{\bar{\varepsilon}\}$ as follows:

$$\{\varepsilon\}_{5\times1} = [H]_{5\times13}\{\bar{\varepsilon}\}_{13\times1} \tag{3.42}$$

The generalized strains and the matrix [***H***] are given as follows:

$$\{\overline{\varepsilon_l}\} = \{\varepsilon_1^0 \quad \varepsilon_2^0 \quad \varepsilon_6^0 \quad \kappa_1^0 \quad \kappa_2^0 \quad \kappa_6^0 \quad \kappa_1 \quad \kappa_2 \quad \kappa_6 \quad \varepsilon_4^0 \quad \varepsilon_5^0 \quad \kappa_4^2 \quad \kappa_5^2\}^T \tag{3.43}$$

where

$$\begin{array}{lll}
\varepsilon_1^0 = \dfrac{\partial u_\circ}{\partial x}; & \varepsilon_2^0 = \dfrac{\partial v_\circ}{\partial y}; & \varepsilon_6^0 = \dfrac{\partial u_\circ}{\partial y} + \dfrac{\partial v_\circ}{\partial x}; \\
\varepsilon_4^0 = \dfrac{\partial w_\circ}{\partial y} - \phi_y; & \varepsilon_5^0 = \dfrac{\partial w_\circ}{\partial x} - \phi_x; & \kappa_1^0 = \Omega\dfrac{\partial \theta_x}{\partial x} - \dfrac{\partial \phi_x}{\partial x}; \\
\kappa_2^0 = \Omega\dfrac{\partial \theta_y}{\partial y} - \dfrac{\partial \phi_y}{\partial y}; & \kappa_6^0 = \Omega\left(\dfrac{\partial \theta_x}{\partial y} + \dfrac{\partial \theta_y}{\partial x}\right) - \left(\dfrac{\partial \phi_x}{\partial y} + \dfrac{\partial \phi_y}{\partial x}\right); & \kappa_1^1 = \dfrac{\partial \theta_x}{\partial x}; \\
\kappa_2^1 = \dfrac{\partial \theta_y}{\partial y} & \kappa_6^1 = \left(\dfrac{\partial \theta_x}{\partial y} + \dfrac{\partial \theta_y}{\partial x}\right) & \kappa_4^2 = \theta_y \text{ and } \kappa_5^2 = \theta_x
\end{array} \tag{3.44}$$

$$[H] = \begin{bmatrix}
1 & 0 & 0 & z & 0 & 0 & g(z) & 0 & 0 & 0 & 0 & 0 & 0 \\
0 & 1 & 0 & 0 & z & 0 & 0 & g(z) & 0 & 0 & 0 & 0 & 0 \\
0 & 0 & 1 & 0 & 0 & z & 0 & 0 & g(z) & 0 & 0 & 0 & 0 \\
0 & 0 & 0 & 0 & 0 & 0 & 0 & 0 & 0 & 1 & 0 & g'(z) & 0 \\
0 & 0 & 0 & 0 & 0 & 0 & 0 & 0 & 0 & 0 & 1 & 0 & g'(z)
\end{bmatrix} \tag{3.45}$$

It is to be noted that [***H***] is a function of thickness coordinate alone and will be employed for integrating properties along the thickness. The generalized strain vector $\{\bar{\varepsilon}\}$ is defined in terms of field variable {***q***} by using the generalized strain components (defined in Eq. (3.44)). Note that these generalized strains are derivative terms of field variables and hence an operator matrix [***L***] is implemented to define the relationship between generalized strains and the field variables {q} as mentioned in Eq. (3.46).

$$\{\bar{\varepsilon}\}_{13\times1} = [L]_{13\times7}\{q\}_{7\times1} \tag{3.46}$$

The strain energy of the k^{th} element is given by Eq. (3.47)

$$U_L^k = \frac{1}{2}\int_V \{\varepsilon\}_k^T \{\sigma\} dV \tag{3.47}$$

The stress terms are converted to the strain terms by using the constitutive relations (Eq. (3.11)) and the resulting strain energy is as follows.

$$U_L^k = \frac{1}{2}\int_V \{\varepsilon\}_{(k)}^T \{\sigma\} dV = \frac{1}{2}\int_V \{\varepsilon\}_{(k)}^T [Q]\{\varepsilon\}_{(k)} dV \tag{3.48}$$

Furthermore, the strain energy expression is simplified in the form of field variables. This is achieved by implementing Eq. (3.42), Eq. (3.46), Eq. (3.41) in Eq. (3.48).

$$U_L^{(k)} = \frac{1}{2}\int_V \left\{\bar{\varepsilon}_i\right\}_{(k)}^T [H]^T [Q][H]\left\{\bar{\varepsilon}_i\right\}_{(k)} dV = \int_S \{q\}_{(k)}^T \left\{B^{(k)}\right\}^T [D]\left\{B^{(k)}\right\}\{q\}_{(k)} dxdy \tag{3.49}$$

where $\left[D\right] = \int_{-h/2}^{h/2} \left[H\right]^T \left[Q\right]\left[H\right] dz$ and the elemental stiffness matrix of *k*th element is given by $\left[K^{(k)}\right] = \iint \left[B^{(k)}\right]^T \left[D\right]\left[B^{(k)}\right] dxdy$. Note that [***D***] is the function of the thickness coordinate alone while [$\boldsymbol{K^{(k)}}$] is the function of *x* and *y* coordinate. Therefore, the volume integration appearing in the strain energy expression can be considered in the form of thickness integral (as defined in [***D***]) and area integral (as defined in [$\boldsymbol{K^{(k)}}$]). The Gauss Quadrature method is used to solve the element stiffness matrix employing the Jacobian as $\left[K^{(k)}\right] = \int_{-1}^{1}\int_{-1}^{1} \left[B^{(k)}\right]^T \left[D\right]\left[B^{(k)}\right] \left|J\right| d\zeta\, d\eta$ to facilitate the transformation between *ξ*-*η* coordinate and *x*-*y* coordinate. In order to overcome the shear locking, selective integration scheme is employed wherein the full integration of order 3x3 is used for the bending terms while the reduced integration of the order 2x2 is used for the shear terms. The total linear strain energy is obtained by assembling linear strain energies of all elements as shown below.

$$U_L = \sum_{k=1}^{nel} U_L^{(k)} = \frac{1}{2}\{q\}^T [K]\{q\} \tag{3.50}$$

where **{*q*}** is the global displacement vector and **[*K*]** is the global elastic stiffness matrix.

Strain energy due to non-linear strains: The non-linear strain contributes to the geometrical stiffness of the FG-CNT reinforced plate. Similar to the procedure followed for strain energy due to linear strains, the strain energy of k^{th} element due to non-linear strain is obtained by implementing the Eqs. (3.10), Eq. (3.11) and the definition of strain energy and is given in Eq. (3.51).

$$U_{NL}^{(k)} = \frac{1}{2}\int_V \{\varepsilon_{NL}\}_{(k)}^T \{\sigma\}_{(k)} dV = \frac{1}{2}\{\varepsilon_{NL}\}_{(k)}^T [S]\{\varepsilon_{NL}\}_{(k)} dV \tag{3.51}$$

Further, Eq. (3.51) is simplified in the form of field variables by employing strain displacement relationship and Eq. (3.41) as follows.

$$U_{NL}^{(k)} = \frac{1}{2}\int_V \{\bar{\varepsilon}_{NL}\}_{(k)}^T \left[H_g\right]^T [S]\left[H_g\right]\{\bar{\varepsilon}\}_{(k)} dV \tag{3.52}$$

$$U_{NL}^{(k)} = \frac{1}{2}\int_s \{q\}_{(k)}^T \left[B_G^{(k)}\right]^T [G]\left[B_G^{(k)}\right]\{q\}_{(k)} dxdy = \frac{1}{2}\{q\}_{(k)}^T \left[K_G^{(k)}\right]\{q\}_{(k)} \tag{3.53}$$

where $[S] = \begin{bmatrix} S_{xx} & 0 \\ 0 & S_{yy} \end{bmatrix}$ S_{xx} and S_{yy} represent the axial compressive loads along the x axis and y axis respectively. Also, it is considered that $S_{xx} = k_1 N_0$ and $S_{yy} = k_2 N_0$ where N_0 is the magnitude of the compressive load. The elemental geometric stiffness matrix [$\boldsymbol{K_G}^{(k)}$] and [$\boldsymbol{G}$] matrix is obtained in the similar manner as [$\boldsymbol{K}^{(k)}$] and [$\boldsymbol{D}$] in the preceding section. The total non-linear strain energy is obtained by assembling the corresponding strain energies of all elements over the CNTRC plate domain as shown below.

$$U_{NL} = \sum_{k=1}^{nel} U_{NL}^{(k)} = \frac{1}{2}\{q\}^T [K_G]\{q\} \tag{3.54}$$

where **{*q*}** is the global displacement vector and **[*K_G*]** is the global geometric stiffness matrix.

Strain energy due to non-linear strains: The additional constraints are imposed because of imposing independent field variables (Eq. (3.38)) and these constraints are satisfied by employing the penalty parameter (γ, taken as 1×10^6) and these constraints also lead to contribution towards the strain energy. The strain energy due to these constraints is obtained for k^{th} element and is given as follows.

$$U_c^{(k)}=\frac{\gamma}{2}\int_V\left[\left(\frac{\partial w_0}{\partial x}-\phi_x\right)_{(k)}^T\left(\frac{\partial w_0}{\partial x}-\phi_x\right)_{(k)}+\left(\frac{\partial w_0}{\partial y}-\phi_y\right)_{(k)}^T\left(\frac{\partial w_0}{\partial y}-\phi_y\right)_{(k)}\right]dV \tag{3.55}$$

The total strain energy due to the artificial constraints is obtained by assembling the corresponding strain energies of all the elements over the CNTRC plate domain as shown below.

$$U_c=\sum_{j=1}^{nel}U_c^{(j)}=\frac{\gamma}{2}\{q\}^T\left[K_c\right]\{q\} \tag{3.56}$$

where **{*q*}** is the global displacement vector and **[*K_G*]** is the global stiffness matrix due to artificial constraints.

Kinetic energy: The inertia of the CNTRC plate contributes towards the kinetic energy. The elemental kinetic energy [$\boldsymbol{T}^{(\mathbf{k})}$] of the CNTRC plate is defined as given in Eq. (3.57)

$$\left[T^{(k)}\right]=\frac{1}{2}\iint\left[\sum_{k=1}^{nl}\int_{-h/2}^{h/2}\left\{\dot{f}\right\}^T\rho(z)\left\{\dot{f}\right\}dz\right]dxdy \tag{3.57}$$

where $\left\{\dot{f}_k\right\}=\left\{\dot{u}\quad\dot{v}\quad\dot{w}\right\}^T$ is the vector representing the velocities at a point in the CNTRC plate domain at which the displacements are u, v, and w and $\rho(z)$ is the density which varies across the thickness due to gradient of CNT across thickness of CNTRC plate. The elemental kinetic energy expression is simplified in the form of field variables and by employing Eq. (3.41), the modified form of kinetic energy expression is as follows.

$$\left[T^{(k)}\right]=\frac{1}{2}\iint\left[\int_{-h/2}^{h/2}\left[\left[N^{(k)}\right]\{\dot{q}\}_{(k)}\right]^T\rho(z)\left[\left[N^{(k)}\right]\{\dot{q}\}_{(k)}\right]dz\right]dxdy \tag{3.58}$$

$$\left[T^{(k)}\right]=\frac{1}{2}\{\dot{q}\}_{(k)}^T\left[M^{(k)}\right]\{\dot{q}\}_{(k)} \tag{3.59}$$

where $\left[M^{(k)}\right]=\int\int\left[N^{(k)}\right]^T\left[R\right]\left[N^{(k)}\right]dxdy \qquad (3.60)$

and $$[R]=\begin{bmatrix} I_0 & 0 & 0 & -I_1 & 0 & I_3 & 0 \\ 0 & I_0 & 0 & 0 & -I_1 & 0 & I_3 \\ 0 & 0 & I_0 & 0 & 0 & 0 & 0 \\ -I_1 & 0 & 0 & I_2 & 0 & -I_4 & 0 \\ 0 & -I_1 & 0 & 0 & I_2 & 0 & -I_4 \\ I_3 & 0 & 0 & -I_4 & 0 & I_5 & 0 \\ 0 & I_3 & 0 & 0 & -I_4 & 0 & I_5 \end{bmatrix} \tag{3.61}$$

The inertia terms appearing in Eq. (3.61) are obtained by performing the integration over the thickness of the FG-CNTRC plate as follows.

$$\begin{bmatrix} I_0 & I_1 & I_2 & I_3 & I_4 & I_5 \end{bmatrix} = \int_{-h/2}^{h/2} \rho(z)\begin{bmatrix} 1 & z & z^2 & f(z) & zf(z) & \left(f(z)\right)^2 \end{bmatrix} dz \tag{3.62}$$

The Gauss Quadrature method is used to solve the element mass matrix employing the Jacobian as $\left[M^{(k)}\right]_j = \int_{-1}^{1}\int_{-1}^{1}\left[N^{(k)}\right]^T[R]\left[N^{(k)}\right]|J|\,d\zeta\, d\eta$ to facilitate the transformation between ξ-η coordinate and *x*-*y* coordinate. The total kinetic energy due to the inertia is obtained by assembling the corresponding kinetic energies of all elements over the CNTRC plate domain as given in Eq. (3.63).

$$[T]=\frac{1}{2}\{\dot{q}\}^T[M]\{\dot{q}\} \tag{3.63}$$

Work done due to hygro-thermo-mechanical load: The work done due to external mechanical load, thermal load, and due to hygroscopic expansion on the k^{th} element is obtained as follows:

$$W^{(k)} = \int_S p(x,y)w\,dxdy + \iint_S \left[\{\varepsilon\}^T_{(k)}[Q]\{\varepsilon_{th}\}_{(k)}\right]dxdy + \iint_S \left[\{\varepsilon\}^T_{(k)}[Q]\{\varepsilon_c\}_{(k)}\right]dxdy \tag{3.64}$$

where $p(x,y)$ is the applied transverse load, $p(x,y) = q_0$ for uniformly distributed load (UDL) and $p(x,y) = q_0 \sin\left(\frac{\pi x}{a}\right)\sin\left(\frac{\pi y}{b}\right)$ for sinusoidal load (SSL). The action of these loads on the FG-CNTRC plate is shown in Fig. 3.3. The strain components arising due to temperature change and moisture change are indicated as ε_{th} and ε_c respectively.

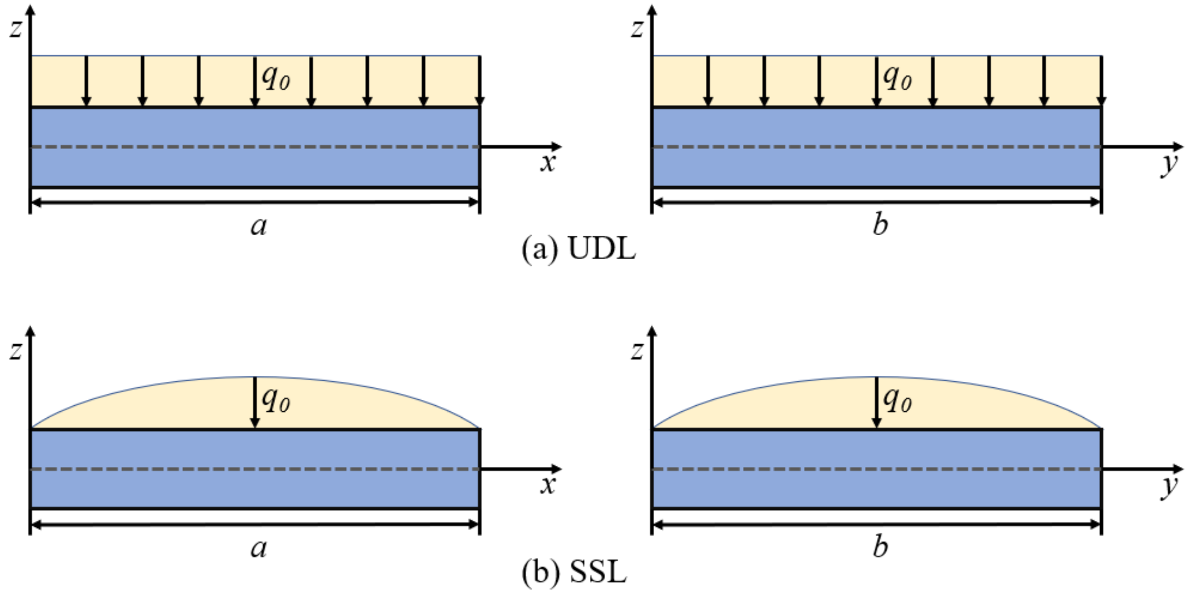

Fig. 3-3: The CNTRC plate subjected to transverse loads (a) UDL and (b) SSL

Following the integration using Gauss Quadrature, the work associated with hygro-thermo-mechanical loads is simplified as follows.

$$W^{(k)} = \{q\}_{(k)}^{T}\left\{F_m^{(k)}\right\} + \{q\}_{(k)}^{T}\left\{F_{th}^{(k)}\right\} + \{q\}_{(k)}^{T}\left\{F_c^{(k)}\right\} \tag{3.65}$$

where $\left\{F_m^{(k)}\right\}, \left\{F_{th}^{(k)}\right\}$, and $\left\{F_c^{(k)}\right\}$ are the elemental load vectors due to mechanical load, thermal load, and moisture change. The total work done due to the mechanical load, thermal load, and moisture change is obtained by assembling the corresponding work done of all elements over the CNTRC plate domain as given in Eq. (3.66).

$$W = \sum_{k=1}^{nel} W^{(k)} = \{q\}^{T}\{F_m\} + \{q\}^{T}\{F_{th}\} + \{q\}^{T}\{F_c\} \tag{3.66}$$

where $\{F_m\}, \{F_{th}\}$, and $\{F_c\}$ are the global load vectors due to mechanical load, thermal load, and moisture change.

3.5.4. Derivation of governing system for finite element analysis

The associated energy terms and the associated work done for the structural analysis of FG-CNTRC plates in the hygro-thermal environment derived in the preceding section are employed in the principle of minimum potential energy to develop the governing system for the required structural analysis. The principle of minimum potential energy is given in Eq. (3.67).

$$\frac{d}{dt}\left(\frac{\partial T}{\partial\{\dot{q}_i\}}\right)+\frac{\partial U_L}{\partial\{q_i\}}+\frac{\partial U_{NL}}{\partial\{q_i\}}+\frac{\partial U_c}{\partial\{q_i\}}+\frac{\partial W}{\partial\{q_i\}}=0 \tag{3.67}$$

The terms appearing in Eq. (3.67) have been defined and obtained in the preceding section in terms of corresponding matrices and vectors. The terms [***T***], [***U_L***], [***U_{NL}***], [***U_c***], and [***W***] from Eqs. (3.50), (3.54), (3.56), (3.63), and (3.66) are employed in Eq. (3.67) to yield the following governing system for the general structural analysis of FG-CNTRC plates.

$$[M]\{\ddot{q}\}+[K+\gamma K_C]\{q\}+\lambda[K_G]\{q\}=\{F_m\}+\{F_{th}\}+\{F_c\} \tag{3.68}$$

The above equation is the generalized governing algebraic equation which is solved to obtain the desired structural response of the FG-CNTRC plate. Further, necessary boundary conditions are imposed on the mathematical system to consider the effect of the constraint edges of FG-CNTRC plates. The simply supported, clamped and their combination are considered as boundary conditions in the framework of finite element analysis. The associated boundary conditions with respect to simply supported edge (designated as 'S') and clamped edge (designated as 'C') are as follows

- Clamped condition (C): $u_0=v_0=w_0=\theta_x=\theta_y=\phi_x=\phi_y=0$
- Simply supported condition (S):
    - Edge parallel to *x*-axis: $u_0=w_0=\theta_x=\phi_x=0$
    - Edge parallel to *y*-axis: $v_0=w_0=\theta_y=\phi_y=0$

After imposing the necessary boundary conditions, the above system (Eq. (3.68)) is classified for particular structural analysis such as hygro-thermo-mechanical analysis, buckling analysis and free vibration analysis.

Hygro-thermo-mechanical analysis: In the context of hygro-thermo-mechanical analysis, the CNTRC plate is assumed to be subjected to transverse mechanical loads (SSL as well as UDL) along with the hygro-thermal loads. Therefore, for such analyses, the geometric stiffness matrix and mass matrix in Eq. (3.68) will vanish and the algebraic system for such analysis is reduced and shown in Eq. (3.69)

$$\left[K+\gamma K_C\right]\{q\}=\{F_m\}+\{F_{th}\}+\{F_c\} \tag{3.69}$$

The above system is solved by performing the matrix inversion and hence the field variables $\{q\}=\{u_0 \quad v_0 \quad w_0 \quad \theta_x \quad \theta_y \quad \phi_x \quad \phi_y\}^T$ are thus obtained. The displacement at any point in the CNTRC plate domain is obtained using the IHSDT. Further, use of strain-displacement relations provides the strains which are employed in the constitutive relation to yield the corresponding stresses. The transverse deflection and the stresses are obtained at the critical points. It should be noted that the stresses are derived quantities and these are evaluated at the Gauss points rather than the node points. Further, the extrapolation and nodal averaging is done to obtain the stress values at the node points.

Buckling analysis: The CNTRC plate is assumed to be subjected to axial compressive forces alone. Therefore, in this context, the mass matrix and the load vector in Eq. (3.68) will vanish. The simplified system of equations is represented in Eq. (3.70).

$$\left[K+\gamma K_C\right]\{q\}+\lambda\left[K_G\right]\{q\}=0 \tag{3.70}$$

It should be noted that the above system is mathematically an eigen-value problem wherein the eigenvalues represent the buckling load parameters with minimum eigen-value representing the critical buckling load. The buckling analysis is carried out with uniaxial compression as well as biaxial compression. Moreover, the eigen-vectors represent the buckling mode shapes.

Free vibration analysis: In the context of free vibration analysis, the CNTRC plate is assumed to be under the effect of its own inertia and hence the other forces are neglected implying that geometric stiffness matrix and the load vector appearing in Eq. (3.68) will vanish. The mathematical system in the framework of free vibration analysis will thus reduce to Eq. (3.71)

$$[M]\{\ddot{q}\}+\left[K+\gamma K_C\right]\{q\}+\lambda\left[K_G\right]\{q\}=\{F_m\}+\{F_{th}\}+\{F_c\} \tag{3.71}$$

Similar to the buckling analysis problem, it should be noted that the above system is mathematically an eigen-value problem wherein the eigenvalues represent the frequency parameters with minimum eigen-value representing the fundamental frequency and eigen-vectors represent the free vibration mode shapes.

3.6. Extended FEM

In order to examine the response of a cracked CNTRC plate, extended FEM is employed. The conventional finite element analysis fails to predict the response of the cracked plate due to discontinuity arising because of the crack. Therefore, it becomes important to model and formulate the discontinuity independent of the finite element mesh. In the context of XFEM, the discontinuities due to pre-existing crack are formulated on the basis of Mohammadi [101] wherein specific local enrichment functions are employed to model the discontinuity.

3.6.1. Crack approximation

While modeling the crack surfaces and crack tip, the field variables $\{q_c\}$ are approximated by a combination of field variables for continuous domain $\{q\}$, field variable for crack-split $\{q_{\text{split}}\}$ and field variables for crack tip $\{q_{\text{tip}}\}$as given in Eq. (3.72)

$$\{q_c(x,y)\} = \{q(x,y)\} + \{q_{split}(x,y)\} + \{q_{tip}(x,y)\} \tag{3.72}$$

In the framework of XFEM, the conventional shape function (Eq. (3.40)) are used for the continuous domain while Heaviside functions along with conventional shape function are used for modeling crack face and enrichment functions along with conventional shape function are used to model the crack tip. The field variable as specified in Eq. (3.72) are written in the explicit form in Eq. (3.73) by making use of the appropriate function of each segment of the CNTRC plate.

$$\begin{aligned}\{q_c(x,y)\} = \sum_{i=1}^{n_n} N_i(x,y) q_i + \sum_{i=1}^{n_s} N_i(x,y)\left(H(x) - H(x_i)\right) a_i \\ + \sum_{i=1}^{n_t} N_i(x,y) \sum_{l=1}^{4} \left(T_l(x) - T_l(x_i)\right) t_i^l\end{aligned} \tag{3.73}$$

where n_n is the total number of nodes, n_s is the number of nodes on the crack surface and n_t is the number of nodes on the crack tip. The field variables associated with the crack surface are designated as a_i while the field variables associated with crack tip are designated as t_I^J. The Heaviside function for modeling crack face is identified as H while T is the enrichment function used for modeling the crack tip. A general representation of standard elements, crack-face or split elements, crack-tip elements and blending elements is shown in Fig. 3.4. It should be noted that the displacements are different at both the sides of the crack face and therefore Heaviside functions are used to model crack face. The crack tip is modeled by crack-tip enrichment functions which are based on the stress and displacements fields around the crack tip and calculated with the help of their analytical solution [102].

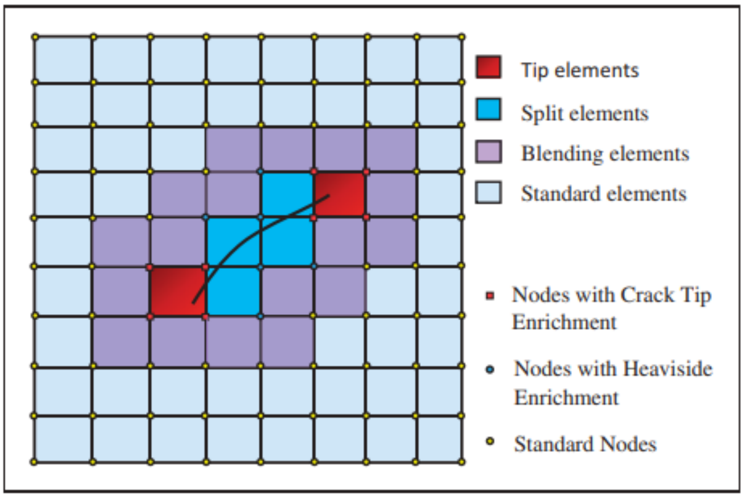

Fig. 3-4: General representation of standard, crack-face or split, crack-tip and blending elements

3.6.2. Crack formulation

The elemental stiffness matrices and load vectors in Eq. (3.69) are now revised based on the approximation presented in Eq. (3.73). The crack growth is simulated on the basis of level Set method in which two orthogonal functions are employed to track the normal and tangential crack growth. The orthogonal functions used in this methods are normal level set function (ψ) and tangential level set function (φ) to track the crack-tip and crack-split, respectively. These orthogonal functions are first defined at nodes of the standard finite element mesh around the corresponding face/tip and with every step of propagation of the crack, these functions are revised. The conditions of the location of node around the crack face/crack tip is depicted in Fig. 3.5 in terms of orthogonal set functions employed in the level set method.

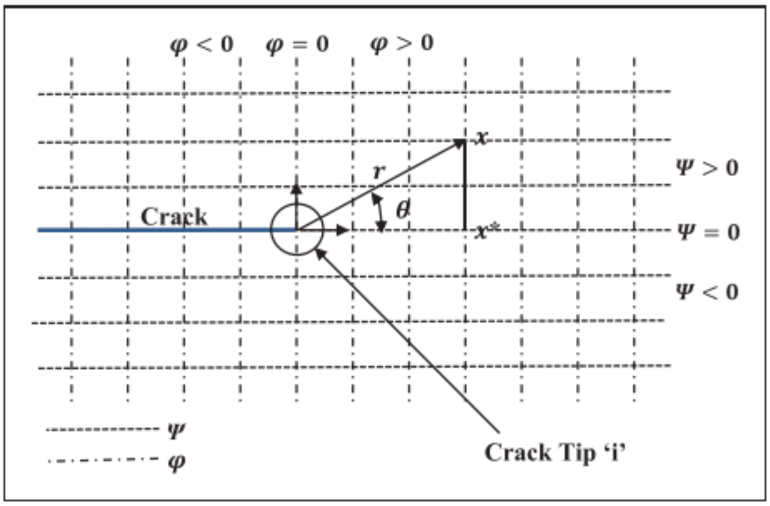

Fig. 3-5: Representation of orthogonal functions employed in level set method and tracking operation

3.7. Implementation of Developed Formulation into the Computer Codes

The developed mathematical formulation in the preceding sections is encoded in the form of computer codes in MATLAB platform. The developed computer codes are capable to (a) predict the temperature dependent and temperature independent material properties of FG-CNTRC plates following the methodology of extended rule of mixture (b) predict the structural responses of CNT reinforced composite plates with SSSS conditions in hygro-thermal environment using analytical approach (c) model, mesh, and analyze the FG-CNT reinforced plate with different boundary conditions using finite element analysis and predict the structural responses in hygro-thermal environment (d) model the cracked plate in the framework of XFEM (e) examine the structural response of cracked plate and hence examine the effect of presence of crack onto the structural response of FG-CNT plates. The developed algorithms consider variety of parameters for the parametric studies such as span-thickness ratio (*a/h*), loading conditions, volume fraction of CNT, distribution of CNT, material models, aspect ratio (*a*/*b*), boundary conditions, crack length, etc. wherever applicable. A meshed FG-CNT reinforced composite in FE framework is depicted in Fig. 3.6 highlighting the nodes and elements. The finite element mesh is created using (8×8) mesh implying that the number of elements are 64 (element numbers marked in red at the center of the elements) and number of nodes are 225 (node numbers are marked blue at the node locations marked as 'o').

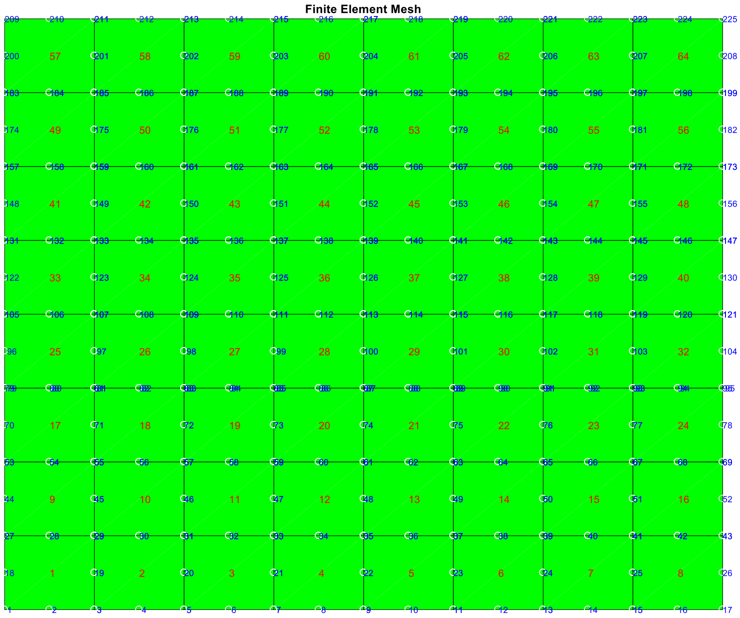

Fig. 3-6: CNTRC plate mesh using eight node finite element indicating the node numbers and element numbers

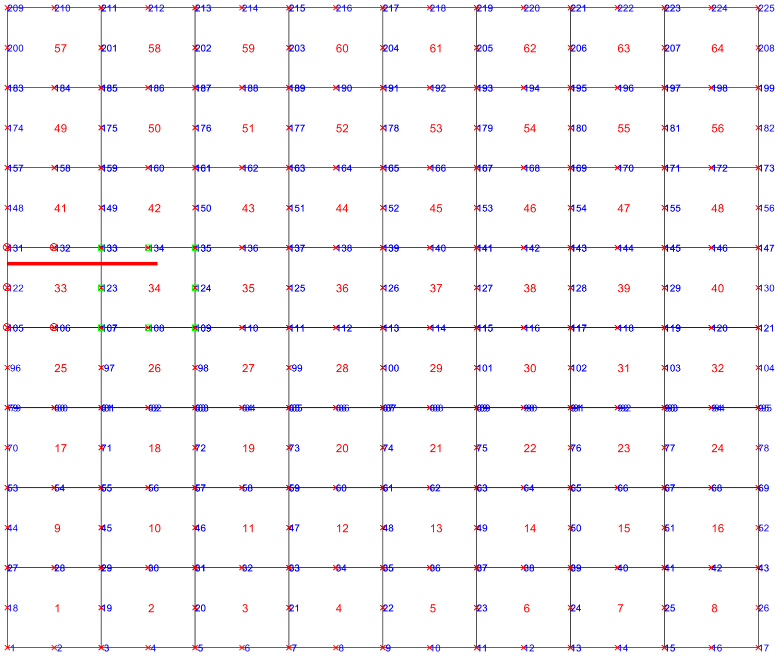

Fig. 3-7: FG-CNTRC plate with pre-existing crack modelled in the framework of XFEM indicating standard element, split element, and tip elements

Also, a cracked FG-CNTRC plate with pre-existing crack modelled in the framework of XFEM is presented in Fig. 3.7 along with the information of split elements and tip elements. The meshed model is created using (8×8) elements. The standard nodes are marked red in color with '×' along with the node numbers at the node locations, the elements numbers are marked red in color at the center of the element's node, the crack is indicated using the solid red line, the nodes of the split elements and tip elements are marked as circles around the ‘×’ in red and green color respectively.

3.8. Summary

In this chapter, the detailed mathematical formation for predicting the structural response characteristics of CNT reinforced composite plates in hygro-thermal environment is presented. The effective material properties of CNTRC plates with a variety of distribution of CNT are obtained using extended rule of mixture. The CNTRC plates are modelled using IHSDT which ensures realistic consideration of shear deformation. Under the assumption of linear structural kinematics and linear-elastic material behavior, the governing differential equations are obtained using principle of virtual work. Analytical solutions (Navier type) of these governing differential equations are obtained for simply supported boundary conditions as a specific case for validating the accuracy of IHSDT for CNTRC plates. Further, the finite element procedures are established in order to ensure the generality of the suggested IHSDT for CNTRC plates. To predict the effect of pre-existing crack onto the structural response of CNTRC plate, XFEM is employed wherein the crack approximation and formulation is discussed. A brief detail of implementation of the developed mathematical formulation into the computer codes is also presented.

Chapter 4

NUMERICAL RESULTS AND DISCUSSIONS

4.1. Introduction

The focus of the present chapter is to examine the static, buckling and free vibration response of FG-CNT reinforced plate under hygro-thermo-mechanical loading condition. The plate is modeled using inverse hyperbolic shear deformation theory. The FG-CNT material constitutes PmPV matrix and single walled carbon nanotubes (SWCNT) reinforcement. Further, the material properties of the constituents (PmPV matrix and SWCNT) are assumed to be temperature dependent. The extended rule of mixture is implemented to evaluate the temperature dependent material properties. The various types of distributions of SWCNTs across the thickness of the plate are considered in the present work (FG-O, FG-X, FG-V and UD). Firstly, the static response of FG-CNT reinforced plate is performed using analytical method and finite element method under the uniformly distributed and sinusoidal loading conditions. The comparison between the CNT reinforced and isotropic plate is made to see the effect of CNT reinforcement on the non-dimensional central deflection. Then, the buckling and free vibration characteristics of temperature dependent FG-CNT reinforced plate are carried out using the analytical method and finite element method. Moreover, the static response of FG-CNT reinforced plate is predicted in the hygro-thermo-mechanical loading condition subjected to uniform distributed loading conditions. Further, the static analysis of temperature dependent FG-CNT reinforced plate in the presence of surface crack is performed using extended finite element method. Thereafter, the static analysis of temperature dependent FG-CNT reinforced plate in the presence of surface crack is examined using the extended finite element method.

4.2. Evaluation of Temperature Dependent Properties of FG-CNTRC Plate

In this section, the temperature dependent material properties of FG-CNT reinforced plate are computed using extended rule of mixture. Since the material properties of both the constituents are temperature dependent. Therefore, the computed properties (Longitudinal Young’s modulus, transverse Young’s modulus and In-plane shear modulus) of FG-CNT reinforced plate are also temperature dependent. The computed equivalent properties along the thickness for the different distributions of CNT are presented in Figs. 4.1- 4.3.

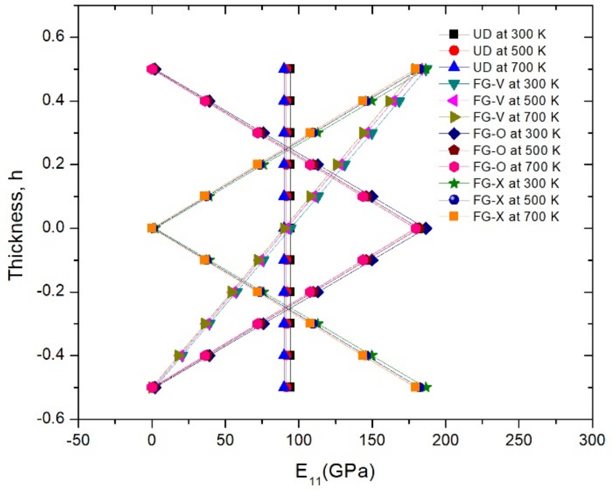

Fig. 4-1: Distribution of Longitudinal Young's modulus along the thickness for different distributions of CNT at different temperatures i.e. 300 K, 500 K and 700 K

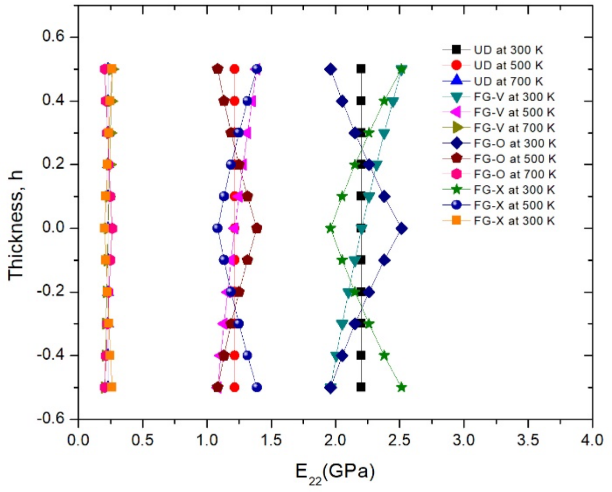

Fig. 4-2: Distribution of Transverse Young's modulus along the thickness for different distributions of CNT at different temperatures i.e. 300 K, 500 K and 700 K

From the figures, it is observed that the material properties (E_{11}, E_{22} and G_{12}) decreases due to increase in temperature. However, the rate of decrement for material propoerties E_{22} and G_{12} is higher in comaprsion to E_{11}. This is due to the fact that transverse Young's modulus and in-plane shear modulus are matrix dependent properties and longitudinal Young's modulus is reinforcement dominated property.

Moreover, the trends for various distributions of CNT are also depicted and it is observed that UD CNT possess the uniform properties throughout. The FG-V distribution possess the maximum properties at the top, while the minimum value at the bottom. The FG-O distribution possess the symmetrical distribution of properties attaining maximum value at the center while minimum value at top and bottom. The FG-X distribution possess the symmetrical distribution however attaining maximum value at the top and bottom surface and minimum value at the center.

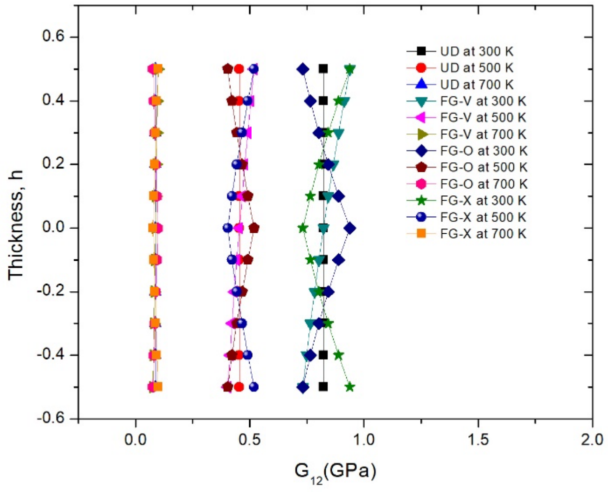

Fig. 4-3: Distribution of In-plane shear modulus along the thickness for different distributions of CNT at different temperatures i.e. 300 K, 500 K and 700 K

4.3. Static Analysis of Temperature Dependent FG-CNTRC Plate

In this section, the static analysis of the temperature dependent FG-CNT reinforced plate is investigated subjected to different transverse loading conditions. The material properties are considered as temperature dependent (temperature is taken as 300 K, 500 K and 700 K) to see its effect on the static response of FG-CNT reinforced plate. Two different approaches (analytical approach and finite element methodology) have been implemented to solve the set of governing equations to study the static response of the FG-CNT reinforced plate. For the analytical approach, a Navier-type closed-form solution is implemented. It is free from computational error and only restricted to simply supported boundary condition. To overcome the restriction of boundary condition, the finite element solution methodology (discussed in Chapter 3) is implemented to solve the set of governing equation subjected to different boundary conditions. A generalized MATLAB code is developed to predict the static response of FG-CNT reinforced plate using analytical approach and FE solution based on IHSDT.

The PmPV (Poly [(m-phenylene-vinylene)-co-(2,5-dioctoxy-p-phenylenevinylen)]) is considered as matrix material. The material properties of the matrix are assumed to be $E_m = (3.51-0.0047T)$ GPa, Poisson's ratio, $\nu_m = 0.34$. The CNT efficiency parameters η_i for the various volume fractions of CNTs as follows [96]

$\eta_1 = 0.149$ and $\eta_2 = 0.934$ for the case $V^*_{CNT} = 0.11$,

$\eta_1 = 0.150$ and $\eta_2 = 0.941$ for the case $V^*_{CNT} = 0.14$,

$\eta_1 = 0.194$ and $\eta_2 = 1.381$ for the case $V^*_{CNT} = 0.17$

Also, it is assumed that efficiency parameters $\eta_3 = \eta_2$. The material properties of CNTs are listed in Table 4.1.

Table 4.1: Temperature dependent material properties of FG-CNT reinforced plate of (10, 10) SWCNT (tube length =9.26 nm, tube mean radius= 0.68 nm, tube thickness= 0.067 nm) Shen and Xiang [103]

Temperature (in K)	E_{11}^{CNT} (Tpa)	E_{22}^{CNT} (Tpa)	G_{12}^{CNT} (Tpa)
300	5.6466	7.0800	1.9445
500	5.5308	6.9348	1.9643
700	5.4744	6.8641	1.9644

4.3.1. Analytical solution

In this subsection, Navier-type closed-form solution is implemented to investigate the static response of FG-CNT reinforced plate under uniform distributed and sinusoidal loading condition with simply supported boundary condition (SSSS). The different span to thickness ratio (*a/h*) i.e., 10, 20 and 50 and different types of CNT distributions are considered i.e., UD, FG-V, FG-K, FG-O and FG-X for the analysis. A square FG-CNT reinforced plate with SSSS boundary condition is considered to investigate the influence of temperature dependent material properties (temperature is taken as 300 K, 500 K and 700 K) on the static behavior. For the validation of results, the computed results are compared with the existing results in the literature at 300 K temperature condition.

In the first case, the static response of FG-CNT reinforced plate subjected to uniform distributed load is presented in Table 4.2 for SSSS boundary condition. The temperature dependent material properties are considered at 300 K temperature. The volume fraction of

CNT is taken as 0.11, 0.14 and 0.17 and corresponding to each volume fraction of CNT three different span to thickness ratios are considered (*a/h* = 10, 20 and 50) for the analysis.

Table 4.2: Non-dimensional central deflection of the square FG-CNTRC plate for different V_{CNT}^*, *a/h* ratio under the action of UDL with SSSS boundary condition

V_{CNT}^*	*a/h*	Type of CNT distribution	Non-dimensional central deflection		
			Present	Soni *et al.* [47]	Zhu *et. al* [53]
0.11	10	Isotropic	8.340×10^{-3}	-	-
		UD	3.649×10^{-3}	3.649×10^{-3}	3.739×10^{-3}
		FG-V	4.384×10^{-3}	4.384×10^{-3}	4.466×10^{-3}
		FG-O	5.442×10^{-3}	5.443×10^{-3}	5.230×10^{-3}
		FG-X	3.046×10^{-3}	3.046×10^{-3}	3.177×10^{-3}
	20	Isotropic	0.1291	-	-
		UD	3.608×10^{-2}	3.608×10^{-2}	3.628×10^{-2}
		FG-V	4.862×10^{-2}	4.862×10^{-2}	4.879×10^{-2}
		FG-O	6.253×10^{-2}	6.253×10^{-2}	6.155×10^{-2}
		FG-X	2.665×10^{-2}	2.665×10^{-2}	2.701×10^{-2}
	50	Isotropic	4.9951	-	-
		UD	1.1553	1.1554	1.155
		FG-V	1.6532	1.6536	1.653
		FG-O	2.1636	2.1637	2.157
		FG-X	0.7898	0.7899	0.7900
0.14	10	UD	3.201×10^{-3}	3.201×10^{-3}	3.306×10^{-3}
		FG-V	3.800×10^{-3}	3.801×10^{-3}	3.894×10^{-3}
		FG-O	4.689×10^{-3}	4.689×10^{-3}	4.525×10^{-3}
		FG-X	2.736×10^{-3}	2.736×10^{-3}	2.844×10^{-3}
	20	UD	2.971×10^{-2}	2.971×10^{-2}	3.001×10^{-2}
		FG-V	3.995×10^{-2}	3.995×10^{-2}	4.025×10^{-2}
		FG-O	5.137×10^{-2}	5.137×10^{-2}	5.070×10^{-2}
		FG-X	2.229×10^{-2}	2.229×10^{-2}	2.256×10^{-2}
	50	UD	0.9147	0.914	0.9175
		FG-V	1.3210	1.321	1.326
		FG-O	1.7374	1.7375	1.738
		FG-X	0.6251	0.6252	0.6271
0.17	10	UD	2.338×10^{-3}	2.338×10^{-3}	2.394×10^{-3}
		FG-V	2.821×10^{-3}	2.822×10^{-3}	2.864×10^{-3}
		FG-O	3.466×10^{-3}	3.466×10^{-3}	3.378×10^{-3}
		FG-X	1.981×10^{-3}	1.981×10^{-3}	2.012×10^{-3}
	20	UD	2.336×10^{-2}	2.336×10^{-2}	2.348×10^{-2}
		FG-V	3.166×10^{-2}	3.166×10^{-2}	3.174×10^{-2}
		FG-O	4.061×10^{-2}	4.061×10^{-2}	4.020×10^{-2}
		FG-X	1.737×10^{-2}	1.714×10^{-2}	1.737×10^{-2}
	50	UD	0.7526	0.7526	0.7515
		FG-V	1.0827	1.0829	1.082
		FG-O	1.4181	1.4182	1.416
		FG-X	0.5149	0.5150	0.5132

The CNTs are assumed to be distributed as uniformly (UD), and functional graded as V, O and X. The computed results (for non-dimensional central deflection) are compared with the analytical solution based on IHSDT presented by Soni *et al.* [47] and FSDT based FEM solution presented by Zhu *et al.* [53].

It is observed that the computed results agree with the results available in the literature i.e. Soni *et al.* [47] (Analytical solution) and Zhu *et al.* [53] (FEM solution). Moreover, a comparison is presented between the FG-CNT reinforced plate and isotropic plate under 300 K temperature condition to show the effect of the CNT reinforcement on the stiffness of matrix material (PmPV). It has been observed that with CNT reinforcement as uniformly, the non-dimensional central deflection decreases by 56%.

After validating the results for the non-dimensional central deflection considering material properties at 300 K temperature. Further, the parametric studies are performed by considering the temperature dependent material properties at 500 K and 700 K. The effect of volume fraction of CNT, span to thickness ratio and distribution of CNT on the non-dimensional central deflection of FG-CNT reinforced plate subjected to uniformly distributed load at different temperature conditions are tabulated in Table 4.3. The effect of temperature dependent material properties is seen on the non-dimensional deflection FG-CNT reinforced plate. For the comparison, the following parameters are considered i.e. volume fraction 0.11, a/h = 10 and uniform distribution of CNT. It is observed that non-dimensional deflection increases by 43% with an increase in temperature from 300 K to 500 K. Whereas, non-dimensional deflection increases by 364% with an increase in temperature from 300 K to 700 K.

In the second case, the static response of FG-CNT reinforced plate subjected to sinusoidal loading condition is presented in Table 4.4 for SSSS boundary condition. For the validation, the temperature dependent material properties are taken at 300 K. Further, to ensure the accuracy of obtained results based on the IHSDT, a comparison is presented in Table 4.4 with the results available in the literature (Soni *et al.* [47]) for FG-CNT reinforced plate. It has been observed (from Table 4.4) that the obtained results exactly replicate the results available in the literature. It is concluded that FG-X possess the least value of deflection as compared to other three type of distributions (UD, FG-O and FG-V). Moreover, with the increase in the volume fraction of the CNT, the non-dimensional central deflection is decreased by 36% in the case of UD distribution of CNT. It has been predicted that with increase in the volume fraction of CNT, significantly decreases the non-dimensional deflection of FG-CNT reinforced plate.

Table 4.3: Non-dimensional central deflection of the square temperature dependent FG-CNTRC plate for different V_{CNT}^{*}, *a/h* ratio under the action of UDL

V_{CNT}^{*}	*a/h*	Type of CNT distribution	Non-dimensional central deflection	
			500 K	700 K
0.11	10	UD	5.230×10^{-3}	1.693×10^{-2}
		FG-V	6.065×10^{-3}	1.787×10^{-2}
		FG-O	7.548×10^{-3}	2.363×10^{-2}
		FG-X	4.531×10^{-3}	1.546×10^{-2}
	20	UD	4.312×10^{-2}	9.629×10^{-2}
		FG-V	5.724×10^{-2}	0.1114
		FG-O	7.390×10^{-2}	0.1417
		FG-X	3.292×10^{-2}	8.406×10^{-2}
	50	UD	1.2187	1.5164
		FG-V	1.7758	2.0804
		FG-O	2.3505	2.7333
		FG-X	0.8329	1.1353
0.14	10	UD	4.670×10^{-3}	1.525×10^{-2}
		FG-V	5.335×10^{-3}	1.597×10^{-2}
		FG-O	6.578×10^{-3}	2.119×10^{-2}
		FG-X	4.144×10^{-3}	1.408×10^{-2}
	20	UD	3.605×10^{-2}	8.610×10^{-2}
		FG-V	4.732×10^{-2}	9.781×10^{-2}
		FG-O	6.072×10^{-2}	0.1226
		FG-X	2.821×10^{-2}	7.718×10^{-2}
	50	UD	0.9626	1.2542
		FG-V	1.4056	1.6905
		FG-O	1.8626	2.1982
		FG-X	0.6626	0.9636
0.17	10	UD	3.337×10^{-3}	1.076×10^{-2}
		FG-V	3.878×10^{-3}	1.135×10^{-2}
		FG-O	4.736×10^{-3}	1.446×10^{-2}
		FG-X	2.951×10^{-3}	1.009×10^{-2}
	20	UD	2.778×10^{-2}	6.131×10^{-2}
		FG-V	3.704×10^{-2}	7.104×10^{-2}
		FG-O	4.742×10^{-2}	8.783×10^{-2}
		FG-X	2.148×10^{-2}	5.497×10^{-2}
	50	UD	0.7913	0.9755
		FG-V	1.1576	1.3418
		FG-O	1.5293	1.7462
		FG-X	0.5428	0.7384

Table 4.4: Non-dimensional central deflection of square TD FG-CNT reinforced plate for different V^*_{CNT}, *a/h* ratio under the action of SSL

V^*_{CNT}	*a/h*	Type of CNT distribution	Non-dimensional central deflection	
			Present	Soni *et al.* [47]
0.11	10	UD	2.461×10^{-3}	2.461×10^{-3}
		FG-V	2.920×10^{-3}	2.919×10^{-3}
		FG-O	3.596×10^{-3}	3.596×10^{-3}
		FG-X	2.075×10^{-3}	2.075×10^{-3}
	20	UD	2.461×10^{-2}	2.461×10^{-2}
		FG-V	3.250×10^{-2}	3.250×10^{-2}
		FG-O	4.138×10^{-2}	4.138×10^{-2}
		FG-X	1.851×10^{-2}	1.851×10^{-2}
	50	UD	0.7910	0.7910
		FG-V	1.1060	1.1060
		FG-O	1.4318	1.4318
		FG-X	0.5529	0.5530
0.14	10	UD	2.172×10^{-3}	2.175×10^{-3}
		FG-V	2.546×10^{-3}	2.546×10^{-3}
		FG-O	3.118×10^{-3}	3.117×10^{-3}
		FG-X	1.870×10^{-3}	1.870×10^{-3}
	20	UD	2.048×10^{-2}	2.048×10^{-2}
		FG-V	2.695×10^{-2}	2.695×10^{-2}
		FG-O	3.431×10^{-2}	3.431×10^{-2}
		FG-X	1.562×10^{-2}	1.562×10^{-2}
	50	UD	0.6345	0.6345
		FG-V	0.8932	0.8932
		FG-O	1.1618	1.1618
		FG-X	0.4431	0.4431
0.17	10	UD	1.576×10^{-3}	1.576×10^{-3}
		FG-V	1.876×10^{-3}	1.876×10^{-3}
		FG-O	2.290×10^{-3}	2.290×10^{-3}
		FG-X	1.345×10^{-3}	1.345×10^{-3}
	20	UD	1.591×10^{-2}	1.591×10^{-2}
		FG-V	2.112×10^{-2}	2.112×10^{-2}
		FG-O	2.686×10^{-2}	2.686×10^{-2}
		FG-X	1.200×10^{-2}	1.200×10^{-2}
	50	UD	0.5142	0.5142
		FG-V	0.7225	0.7225
		FG-O	0.9381	0.9381
		FG-X	0.3585	0.3585

To predict the influence of the temperature dependent material properties on the non-dimensional transverse deflection of the FG-CNT reinforced plate subjected to sinusoidal loading condition (with simply supported boundary condition). The static response of FG-CNT reinforced plate at different temperature conditions (i.e. 500 K and 700 K) is tabulated in Table 4.5. It has been observed that with increase in temperature, the non-dimensional transverse deflection of FG-CNT reinforced plate increases. It is concluded that with an increase in temperature from 300 K to 500 K, the non-dimensional transverse deflection increases by 45 % in comparison to material properties at 300 K temperature (Volume fraction 0.11, *a/h* = 10 and uniform distribution of CNT). Similarly, the non-dimensional deflection of FG-CNT reinforced plate (at 700 K temperature) increases by 385 % in comparison to temperature dependent material properties at 300 K temperature (volume fraction 0.11, *a/h* = 10 and uniform distribution of CNT). Moreover, the effect of FG-X distribution is least on the transverse non-dimensional deflection in comparison to other types (UD, FG-V, FG-O).

Table 4.5: Non-dimensional central deflection of the square TD FG-CNTRC plate for different V_{CNT}^{*} and *a/h* ratio under the action of SSL

V_{CNT}^{*}	a/h	Type of CNT distribution	Non-dimensional central deflection	
			500 K	700 K
0.11	10	UD	3.582×10^{-3}	1.195×10^{-2}
		FG-V	4.106×10^{-3}	1.254×10^{-2}
		FG-O	5.065×10^{-3}	1.638×10^{-2}
		FG-X	3.127×10^{-3}	1.094×10^{-2}
	20	UD	3.033×10^{-2}	7.259×10^{-2}
		FG-V	3.936×10^{-2}	8.290×10^{-2}
		FG-O	5.016×10^{-2}	0.1042
		FG-X	2.357×10^{-2}	6.378×10^{-2}
	50	UD	0.8669	1.1861
		FG-V	1.2279	1.5997
		FG-O	1.6023	2.0767
		FG-X	0.6068	0.8968
0.14	10	UD	3.214×10^{-3}	1.080×10^{-2}
		FG-V	3.631×10^{-3}	1.126×10^{-2}
		FG-O	4.443×10^{-3}	1.475×10^{-2}
		FG-X	2.866×10^{-3}	9.984×10^{-3}
	20	UD	2.564×10^{-2}	6.522×10^{-2}
		FG-V	3.289×10^{-2}	7.326×10^{-2}
		FG-O	4.169×10^{-2}	9.100×10^{-2}
		FG-X	2.037×10^{-2}	5.864×10^{-2}
	50	UD	0.6948	0.9871
		FG-V	0.9851	1.3115
		FG-O	1.2874	1.6897
		FG-X	0.4888	0.7640
0.17	10	UD	2.284×10^{-3}	7.590×10^{-3}
		FG-V	2.622×10^{-3}	7.963×10^{-3}
		FG-O	3.181×10^{-3}	1.006×10^{-2}
		FG-X	2.029×10^{-3}	7.105×10^{-3}
	20	UD	1.951×10^{-2}	4.619×10^{-2}
		FG-V	2.541×10^{-2}	5.280×10^{-2}
		FG-O	3.220×10^{-2}	6.478×10^{-2}
		FG-X	1.529×10^{-2}	4.149×10^{-2}
	50	UD	0.5617	0.7623
		FG-V	0.7983	1.0301
		FG-O	1.0425	1.3278
		FG-X	0.3933	0.5820

4.3.2. Finite element solution

In this section, the finite element (FE) based model for the inverse hyperbolic shear deformation theory is developed to analyze the static response of FG-CNT reinforced plate (considering temperature dependent material properties) subjected to transverse sinusoidal and uniform distributed loading condition. Also, the influence of the boundary conditions, span to thickness ratio, volume fraction of CNTs, pattern of CNTs distribution on the flexural behavior of FG-CNT reinforced plate is investigated. For the comparison, the temperature dependent material properties are considered at 300 K. The computed results are compared with the existing literature in order to validate the effectiveness and accuracy of the presented model. A generalized MATLAB code developed in order to formulate stiffness matrix and force vector for the FG-CNT reinforced plate. The boundary constraints associated with clamped and simply supported boundary edge are given as follows:

Clamped conditions (C): $u_\circ = v_\circ = w_\circ = \theta_x = \theta_y = \phi_x = \phi_y = 0$

Simply-supported conditions (S):

$$\begin{aligned} u_\circ = w_\circ = \theta_x = \phi_x = 0 \quad & \text{at } y = 0 \text{ and } y = b \\ v_\circ = w_\circ = \theta_y = \phi_y = 0 \quad & \text{at } x = 0 \text{ and } x = a \end{aligned}$$

4.3.2.1. Convergence study

Firstly, the convergence study of FG-CNTRC plate is carried out using the finite element method. The FG-CNT reinforced plate having a fixed span to thickness ratio (*a/h* = 10), uniformly distributed CNTs and material properties at 300 K temperature is considered for the convergence study. The considered plate is subjected to uniformly distributed load with simply supported boundary conditions (SSSS). The effect of volume fraction and mesh size on the non-dimensional central deflection is presented in Fig. 4.4. Moreover, validation for convergence test along with the close form solution (Soni *et al.* [47]) is included. The non-dimensional central deflection is calculated using the following relationship $\overline{w} = w/h$. It has been observed (from the Fig. 4.4) that the deflection shows the fast convergence rate and excellently converge between the mesh sizes (*6* × *6*) to (*12* × *12*) for different volume fractions. Moreover, mesh size (*12* × *12*) has been adopted for forthcoming studies.

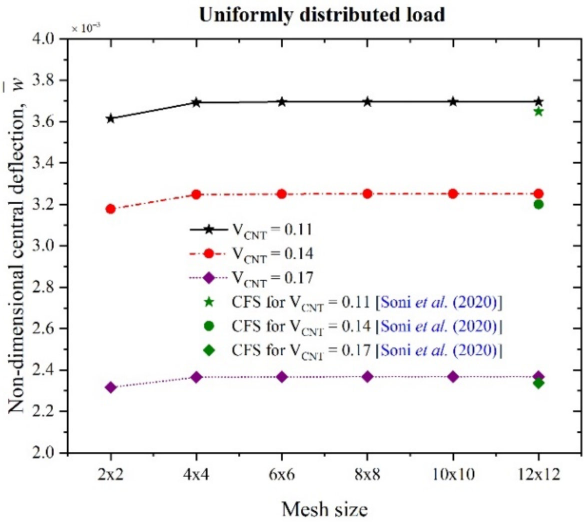

Fig. 4-4: Convergence study for non-dimensional deflection of the FG-CNTR plate subjected to UDL with *a/h*= 10 at 300 K temperature

4.3.2.2. Flexural response of FG-CNTR plate under UDL

The flexural behavior of FG-CNT reinforced plate is examined under uniformly distributed load for different set of boundary conditions i.e. SSSS, SCSC, SCSS and CCCC. The different span to thickness ratio (*a/h*) i.e. 10, 20 and 50 and different types of CNT distributions are considered i.e. UD, FG-V, FG-Λ, FG-O and FG-X for the analysis. Several problems have been solved to investigate the influence of temperature dependent material properties (temperature is taken as 300 K, 500 K and 700 K) on the flexural behavior of FG-CNT reinforced plate. For the validation of results, the computed results are compared with the existing results in the literature at 300 K for different boundary conditions.

The flexural response of square FG-CNT reinforced plate subjected to uniform distributed load in presented in Table 4.6 for different set of boundary conditions (SSSS, SCSC, SCSS, and CCCC). The volume fraction of CNT is taken as 0.11, 0.14 and 0.17 and corresponding to each volume fraction of CNT three different span to thickness ratios are considered (*a/h* = 10, 20 and 50) for the analysis. The CNTs are assumed to be distributed as uniformly (UD), and functional graded as V, O and X. The temperature dependent material properties are considered at 300 K temperature. The authors have compared the non-dimensional central deflection results computed for SSSS boundary condition with the analytical results provided by Soni *et al.* [47] to ensure the accuracy of FE model. Also, the computed results for same boundary condition are compared with FE model-based results (in the framework of first order shear deformation theory) provided by Zhu *et al.* [53]. It has been concluded that the results obtained using IHSDT provides better response than FSDT based FE model. This is due to avoided shear correction factor in higher order shear deformation theories. Moreover, the authors have compared the results for other set of boundary conditions i.e. SCSC and CCCC with the results reported in literature Zhu *et al.* [53]. The new results are presented for SCSS boundary condition (provided in Table 4.6). It has been predicted (from the results) that the non-dimensional central deflection of FG-CNT reinforced plate decreases with increase in the volume fraction of CNTs. Therefore, the maximum and minimum central deflection of FG-CNT reinforced plate is observed for volume fraction of CNTs taken as 0.11 and 0.17 respectively. The authors have seen the effect of different types of CNTs distribution on the central deflection of plate. It has been concluded from the Table 4.6 that FG-X has the minimum central deflection followed by UD, FG-V and FG-O. This is due to the pattern of CNTs distribution across the thickness of FG-CNT reinforced plate. The CNTs distribution i.e. FG-X has minimum central deflection because of CNTs distribution is more on the top and bottom of FG-CNT reinforced plate which increase the stiffness of the plate. Also, the effect of different set of boundary conditions is presented on the central deflection of FG-CNT reinforced plate. The FG-CNT reinforced plate subjected to transverse load with all edges clamped i.e. CCCC has minimum response in comparison to other set of boundary conditions. Thus, the FG-CNT reinforced plate subjected to transverse loading with CCCC boundary conditions is most preferable and plate with SSSS boundary conditions is least preferable. Moreover, it has been concluded (from the Table 4.6) that the FG-CNT reinforced plate under given set of conditions FG-X distribution (CNT distribution pattern) with all edges clamped (CCCC) and volume fraction of CNT is considered 0.17 for such type of application purposes.

Table 4.6: Non-dimensional central deflection of the square FG-CNTRC plate for different V^*_{CNT}, *a/h* ratio and boundary conditions subjected to uniform distributed load

V^*_{CNT}	*a/h*	CNT distribution	Non-dimensional central deflection							
			SSSS			SCSC		SCSS	CCCC	
			Present	Soni *et al.* [47]	Zhu *et al.* [53]	Present	Zhu *et al.* [53]	Present	Present	Zhu *et al.* [53]
0.11	10	UD	3.6965×10^{-3}	3.649×10^{-3}	3.739×10^{-3}	2.2160×10^{-3}	3.325×10^{-3}	2.8644×10^{-3}	2.0964×10^{-3}	2.228×10^{-3}
		FG-V	4.4283×10^{-3}	4.384×10^{-3}	4.466×10^{-3}	2.3766×10^{-3}	3.853×10^{-3}	3.2030×10^{-3}	2.2298×10^{-3}	2.351×10^{-3}
		FG-O	5.4412×10^{-3}	5.443×10^{-3}	5.230×10^{-3}	2.7906×10^{-3}	4.433×10^{-3}	3.8320×10^{-3}	2.5871×10^{-3}	2.512×10^{-3}
		FG-X	3.1162×10^{-3}	3.046×10^{-3}	3.177×10^{-3}	2.0737×10^{-3}	2.867×10^{-3}	2.5763×10^{-3}	1.9635×10^{-3}	2.109×10^{-3}
	20	UD	3.6226×10^{-2}	3.608×10^{-2}	3.628×10^{-2}	1.3007×10^{-2}	3.393×10^{-2}	2.0493×10^{-2}	1.3055×10^{-2}	1.339×10^{-2}
		FG-V	4.8752×10^{-2}	4.862×10^{-2}	4.879×10^{-2}	1.5665×10^{-2}	4.381×10^{-2}	2.6031×10^{-2}	1.5625×10^{-2}	1.593×10^{-2}
		FG-O	6.2536×10^{-2}	6.253×10^{-2}	6.155×10^{-2}	1.9572×10^{-2}	5.389×10^{-2}	3.3012×10^{-2}	1.9350×10^{-2}	1.860×10^{-2}
		FG-X	2.6873×10^{-2}	2.665×10^{-2}	2.701×10^{-2}	1.1055×10^{-2}	2.587×10^{-2}	1.6421×10^{-2}	1.1096×10^{-2}	1.150×10^{-2}
	50	UD	1.1561	1.1554	1.155	0.2632	1.099	0.5060	0.2617	0.2618
		FG-V	1.6540	1.6536	1.653	0.3633	1.504	0.7240	0.3650	0.3649
		FG-O	2.1636	2.1637	2.157	0.4766	1.909	0.9572	0.4793	0.4719
		FG-X	0.7911	0.7899	0.7900	0.1923	0.7728	0.3554	0.1893	0.1894
0.14	10	UD	3.2746×10^{-3}	3.201×10^{-3}	3.306×10^{-3}	2.0656×10^{-3}	2.974×10^{-3}	2.6192×10^{-3}	1.9608×10^{-3}	2.087×10^{-3}
		FG-V	3.8739×10^{-3}	3.801×10^{-3}	3.894×10^{-3}	2.1901×10^{-3}	3.412×10^{-3}	2.8946×10^{-3}	2.0644×10^{-3}	2.182×10^{-3}
		FG-O	4.7207×10^{-3}	4.689×10^{-3}	4.525×10^{-3}	2.5284×10^{-3}	3.916×10^{-3}	3.4155×10^{-3}	2.3649×10^{-3}	2.313×10^{-3}
		FG-X	2.8217×10^{-3}	2.736×10^{-3}	2.844×10^{-3}	1.9601×10^{-3}	2.583×10^{-3}	2.3957×10^{-3}	1.8563×10^{-3}	1.979×10^{-3}
	20	UD	3.0053×10^{-2}	2.971×10^{-2}	3.001×10^{-2}	1.1543×10^{-2}	2.852×10^{-2}	1.7642×10^{-2}	1.1589×10^{-2}	1.188×10^{-2}
		FG-V	4.0346×10^{-2}	3.995×10^{-2}	4.025×10^{-2}	1.3635×10^{-2}	3.689×10^{-2}	2.2111×10^{-2}	1.3656×10^{-2}	1.390×10^{-2}
		FG-O	5.1715×10^{-2}	5.137×10^{-2}	5.070×10^{-2}	1.6744×10^{-2}	4.557×10^{-2}	2.7747×10^{-2}	1.6689×10^{-2}	1.604×10^{-2}
		FG-X	2.2631×10^{-2}	2.229×10^{-2}	2.256×10^{-2}	1.0051×10^{-2}	2.184×10^{-2}	1.4479×10^{-2}	1.0087×10^{-2}	1.036×10^{-2}
	50	UD	0.9215	0.914	0.9175	0.2167	0.8890	0.4079	0.2139	0.2131
		FG-V	1.3304	1.321	1.326	0.2964	1.234	0.5810	0.2964	0.2955
		FG-O	1.7488	1.7375	1.738	0.3855	2.865	0.7671	0.3877	0.3805
		FG-X	0.6303	0.6252	0.6271	0.1604	0.6206	0.2903	0.1577	0.1560
0.17	10	UD	2.9711×10^{-3}	2.338×10^{-3}	2.394×10^{-3}	1.9444×10^{-3}	2.124×10^{-3}	2.4318×10^{-3}	1.8501×10^{-3}	1.412×10^{-3}
		FG-V	3.4748×10^{-3}	2.822×10^{-3}	2.864×10^{-3}	2.0419×10^{-3}	2.461×10^{-3}	2.6601×10^{-3}	1.9306×10^{-3}	1.486×10^{-3}
		FG-O	4.1873×10^{-3}	3.466×10^{-3}	3.378×10^{-3}	2.3165×10^{-3}	2.865×10^{-3}	3.0915×10^{-3}	2.1820×10^{-3}	$1.^{595}\times10^{-3}$
		FG-X	2.6106×10^{-3}	1.981×10^{-3}	2.012×10^{-3}	1.8647×10^{-3}	1.804×10^{-3}	2.2537×10^{-3}	1.7646×10^{-3}	1.318×10^{-3}
	20	UD	2.5880×10^{-2}	2.336×10^{-2}	2.348×10^{-2}	1.0498×10^{-2}	2.190×10^{-2}	1.5672×10^{-2}	1.0540×10^{-2}	8.560×10^{-3}
		FG-V	3.4588×10^{-2}	3.166×10^{-2}	3.174×10^{-2}	1.2213×10^{-2}	2.834×10^{-2}	1.9402×10^{-2}	1.2254×10^{-2}	1.021×10^{-2}
		FG-O	4.4167×10^{-2}	4.061×10^{-2}	4.020×10^{-2}	1.4728×10^{-2}	3.518×10^{-2}	2.4043×10^{-2}	1.4749×10^{-2}	1.198×10^{-2}
		FG-X	1.9803×10^{-2}	1.714×10^{-2}	1.737×10^{-2}	9.3277×10^{-3}	1.653×10^{-2}	1.3140×10^{-2}	9.3604×10^{-3}	7.290×10^{-3}
	50	UD	0.7663	0.7526	0.7515	0.1855	0.7135	0.3437	0.1826	0.1698
		FG-V	1.1122	1.0829	1.082	0.2516	0.9790	0.4864	0.2507	0.2384
		FG-O	1.4654	1.4182	1.416	0.3255	1.252	0.6400	0.3259	0.3085
		FG-X	0.5254	0.5150	0.5132	0.1393	04990	0.2474	0.1368	0.1223

Table 4.7: Non-dimensional central deflection of the square FG-CNTRC plate for different V_{CNT}^{*}, *a/h* ratio and boundary constraints under the action of UDL (temperature dependent properties at 500 K)

V_{CNT}^{*}	a/h	CNT distribution	Non-dimensional central deflection				
			SSSS (FEM)	SSSS (CFS)	SCSC	SCSS	CCCC
0.11	10	UD	5.3472×10^{-3}	5.230×10^{-3}	3.6632×10^{-3}	4.5027×10^{-3}	3.4947×10^{-3}
		FG-V	6.1759×10^{-3}	6.065×10^{-3}	3.8317×10^{-3}	4.8896×10^{-3}	3.6372×10^{-3}
		FG-O	7.5435×10^{-3}	7.548×10^{-3}	4.4336×10^{-3}	5.7875×10^{-3}	4.1709×10^{-3}
		FG-X	4.6983×10^{-3}	4.531×10^{-3}	3.4987×10^{-3}	4.1561×10^{-3}	3.3340×10^{-3}
	20	UD	4.3409×10^{-2}	4.312×10^{-2}	1.8996×10^{-2}	2.7474×10^{-2}	1.9047×10^{-2}
		FG-V	5.7521×10^{-2}	5.724×10^{-2}	2.1748×10^{-2}	3.3486×10^{-2}	2.1830×10^{-2}
		FG-O	7.3901×10^{-2}	7.390×10^{-2}	2.6574×10^{-2}	4.1964×10^{-2}	2.6645×10^{-2}
		FG-X	3.3356×10^{-2}	3.292×10^{-2}	1.6911×10^{-2}	2.3123×10^{-2}	1.6922×10^{-2}
	50	UD	1.22014	1.2187	0.30862	0.56082	0.30341
		FG-V	1.77720	1.7758	0.41509	0.78469	0.41020
		FG-O	2.35053	2.3505	0.53667	1.03321	0.53516
		FG-X	0.83649	0.8329	0.23446	0.40693	0.22962
0.14	10	UD	4.8326×10^{-3}	4.670×10^{-3}	3.4482×10^{-3}	4.1701×10^{-3}	3.2971×10^{-3}
		FG-V	5.4944×10^{-3}	5.335×10^{-3}	3.5726×10^{-3}	4.4781×10^{-3}	3.4017×10^{-3}
		FG-O	6.6209×10^{-3}	6.578×10^{-3}	4.0587×10^{-3}	5.2148×10^{-3}	3.8446×10^{-3}
		FG-X	4.3409×10^{-3}	4.144×10^{-3}	3.3267×10^{-3}	3.8995×10^{-3}	3.1689×10^{-3}
	20	UD	3.6592×10^{-2}	3.605×10^{-2}	1.7272×10^{-2}	2.4254×10^{-2}	1.7287×10^{-2}
		FG-V	4.7914×10^{-2}	4.732×10^{-2}	1.9403×10^{-2}	2.9002×10^{-2}	1.9478×10^{-2}
		FG-O	6.1129×10^{-2}	6.072×10^{-2}	2.3264×10^{-2}	3.5782×10^{-2}	2.3362×10^{-2}
		FG-X	2.8791×10^{-2}	2.821×10^{-2}	1.5698×10^{-2}	2.0906×10^{-2}	1.5697×10^{-2}
	50	UD	0.97069	0.9626	0.25897	0.45929	0.25382
		FG-V	1.41625	1.4056	0.34309	0.63550	0.33774
		FG-O	1.87491	1.8626	0.44020	0.83015	0.43535
		FG-X	0.67313	0.6626	0.20057	0.33881	0.19627
0.17	10	UD	4.4515×10^{-3}	3.337×10^{-3}	3.2681×10^{-3}	3.9051×10^{-3}	3.1298×10^{-3}
		FG-V	4.9963×10^{-3}	3.878×10^{-3}	3.3578×10^{-3}	4.1567×10^{-3}	3.2038×10^{-3}
		FG-O	5.9270×10^{-3}	4.736×10^{-3}	3.7472×10^{-3}	4.7575×10^{-3}	3.5695×10^{-3}
		FG-X	4.0736×10^{-3}	2.951×10^{-3}	3.1746×10^{-3}	3.6890×10^{-3}	3.0208×10^{-3}
	20	UD	3.1980×10^{-2}	2.778×10^{-2}	1.5986×10^{-2}	2.1964×10^{-2}	1.5979×10^{-2}
		FG-V	4.1402×10^{-2}	3.704×10^{-2}	1.7707×10^{-2}	2.5862×10^{-2}	1.7760×10^{-2}
		FG-O	5.2313×10^{-2}	4.742×10^{-2}	2.0820×10^{-2}	3.1372×10^{-2}	2.0912×10^{-2}
		FG-X	2.5728×10^{-2}	2.148×10^{-2}	1.4771×10^{-2}	1.9316×10^{-2}	1.4767×10^{-2}
	50	UD	0.8093	0.7913	0.2254	0.3926	0.2207
		FG-V	1.1781	1.1576	0.2947	0.5381	0.2898
		FG-O	1.5578	1.5293	0.3749	0.6968	0.3693
		FG-X	0.5671	0.5428	0.1777	0.2935	0.1738

The non-dimensional central deflection is presented in Table 4.7 and Table 4.8 considering temperature dependent material properties at 500 K and 700 K temperature respectively. The effect of temperature dependent material properties is seen on the central deflection of FG-CNT reinforced plate. The computed results (transverse deflection) based on

FE model are compared with the closed form solution (CFS) obtained using IHSDT subjected to uniformly distributed load with all edges simply supported. It has been observed from the comparison that the percentage error in results is less than 1% computed using FE model and CFS. Tables 4.6 - 4.8 are compared to see the effect of temperature dependent material properties on the central deflection of FG-CNT reinforced plate. For the comparison of the results, the following parameters are considered i.e., type of distribution pattern i.e. UD, volume fraction of CNTs as 0.11, a/h =10 and all edges simply supported (SSSS). It has been concluded from Tables 4.6 and 4.7 that with increase in temperature from 300 K to 500 K, the central deflection of FG-CNTR plate increases by 44% in comparison to considered material properties at 300 K. Further on comparing Tables 4.6 and 4.8, the observation is drawn that as the temperature is increased from 300 K to 700 K, the non-dimensional central deflection of FG-CNT reinforced plate increased by 417% in comparison to considering temperature dependent material properties at 300 K. Thus, it has been concluded that the bending is significantly influenced by considering temperature dependent material properties. As the temperature is increased from 300 K to 700 K, the central deflection of FG-CNT reinforced plate is significantly increased.

Table 4.8: Non-dimensional central deflection of the square FG-CNTRC plate for different, *a/h* ratio, and boundary constraints subjected to UDL (temperature dependent properties at 700 K)

V_{CNT}^*	*a/h*	CNT distribution	Non-dimensional central deflection				
			SSSS (FEM)	SSSS (CFS)	SCSC	SCSS	CCCC
0.11	10	UD	1.9388×10^{-2}	1.693×10^{-2}	1.6750×10^{-2}	1.8421×10^{-2}	1.6166×10^{-2}
		FG-V	2.0280×10^{-2}	1.787×10^{-2}	1.6871×10^{-2}	1.8967×10^{-2}	1.6266×10^{-2}
		FG-O	2.3859×10^{-2}	2.363×10^{-2}	1.8267×10^{-2}	2.1303×10^{-2}	1.7584×10^{-2}
		FG-X	1.8512×10^{-2}	1.546×10^{-2}	1.6493×10^{-2}	1.7796×10^{-2}	1.5860×10^{-2}
	20	UD	1.0034×10^{-1}	9.629×10^{-2}	7.2237×10^{-2}	8.6932×10^{-2}	7.1574×10^{-2}
		FG-V	1.1491×10^{-1}	0.1114	7.4863×10^{-2}	9.3626×10^{-2}	7.4358×10^{-2}
		FG-O	1.4180×10^{-1}	0.1417	8.6182×10^{-2}	1.1080×10^{-1}	8.5916×10^{-2}
		FG-X	8.9448×10^{-2}	8.406×10^{-2}	6.9405×10^{-2}	8.0857×10^{-2}	6.8826×10^{-2}
	50	UD	1.5977	1.5164	0.6720	0.9870	0.6565
		FG-V	2.1609	2.0804	0.7836	1.2225	0.7671
		FG-O	2.7974	2.7333	0.9629	1.5369	0.9441
		FG-X	1.2142	1.1353	0.5888	0.8175	0.5746
0.14	10	UD	1.8232×10^{-2}	1.525×10^{-2}	1.6037×10^{-2}	1.7453×10^{-2}	1.5488×10^{-2}
		FG-V	1.8885×10^{-2}	1.597×10^{-2}	1.6066×10^{-2}	1.7844×10^{-2}	1.5503×10^{-2}
		FG-O	2.1757×10^{-2}	2.119×10^{-2}	1.7115×10^{-2}	1.9688×10^{-2}	1.6535×10^{-2}
		FG-X	1.7595×10^{-2}	1.408×10^{-2}	1.5811×10^{-2}	1.6958×10^{-2}	1.5187×10^{-2}
	20	UD	9.1291×10^{-2}	8.610×10^{-2}	6.8273×10^{-2}	8.0799×10^{-2}	6.7566×10^{-2}
		FG-V	1.0248×10^{-1}	9.781×10^{-2}	7.0129×10^{-2}	8.6097×10^{-2}	6.9541×10^{-2}
		FG-O	1.2398×10^{-1}	0.1226	7.9115×10^{-2}	9.9938×10^{-2}	7.8695×10^{-2}
		FG-X	8.3188×10^{-2}	7.718×10^{-2}	6.6095×10^{-2}	7.6067×10^{-2}	6.5562×10^{-2}
	50	UD	1.3408	1.2542	0.6062	0.8647	0.5917
		FG-V	1.7815	1.6905	0.6935	1.0510	0.6781
		FG-O	2.2889	2.1982	0.8376	1.3030	0.8204
		FG-X	1.0408	0.9636	0.5431	0.7337	0.5298
0.17	10	UD	1.7267×10^{-2}	1.076×10^{-2}	1.5382×10^{-2}	1.6617×10^{-2}	1.4862×10^{-2}
		FG-V	1.7735×10^{-2}	1.135×10^{-2}	1.5317×10^{-2}	1.6869×10^{-2}	1.4789×10^{-2}
		FG-O	2.0023×10^{-2}	1.446×10^{-2}	1.6105×10^{-2}	1.8323×10^{-2}	1.5609×10^{-2}
		FG-X	1.6787×10^{-2}	1.009×10^{-2}	1.5148×10^{-2}	1.6195×10^{-2}	1.4530×10^{-2}
	20	UD	8.4526×10^{-2}	6.131×10^{-2}	6.4894×10^{-2}	7.5867×10^{-2}	6.4173×10^{-2}
		FG-V	9.3523×10^{-2}	7.104×10^{-2}	6.6132×10^{-2}	8.0120×10^{-2}	6.5505×10^{-2}
		FG-O	1.1083×10^{-1}	8.783×10^{-2}	7.3332×10^{-2}	9.1286×10^{-2}	7.2710×10^{-2}
		FG-X	7.8404×10^{-2}	5.497×10^{-2}	6.3100×10^{-2}	7.2080×10^{-2}	6.2632×10^{-2}
	50	UD	1.1675	0.9755	0.5579	0.7787	0.5443
		FG-V	1.5283	1.3418	0.6288	0.9322	0.6144
		FG-O	1.9456	1.7462	0.7463	1.1385	0.7301
		FG-X	0.9245	0.7384	0.5089	0.6746	0.4964

Moreover, in order to examine the influence of CNT distribution (UD, FG-V, FG-Λ, FG-O and FG-X) on displacement and stress, an FG-CNT reinforced plate is considered with all edges clamped (CCCC) boundary condition and *a/h* = 50 subjected to uniformly distributed load. The material properties are considered at 700 K temperature conditions.

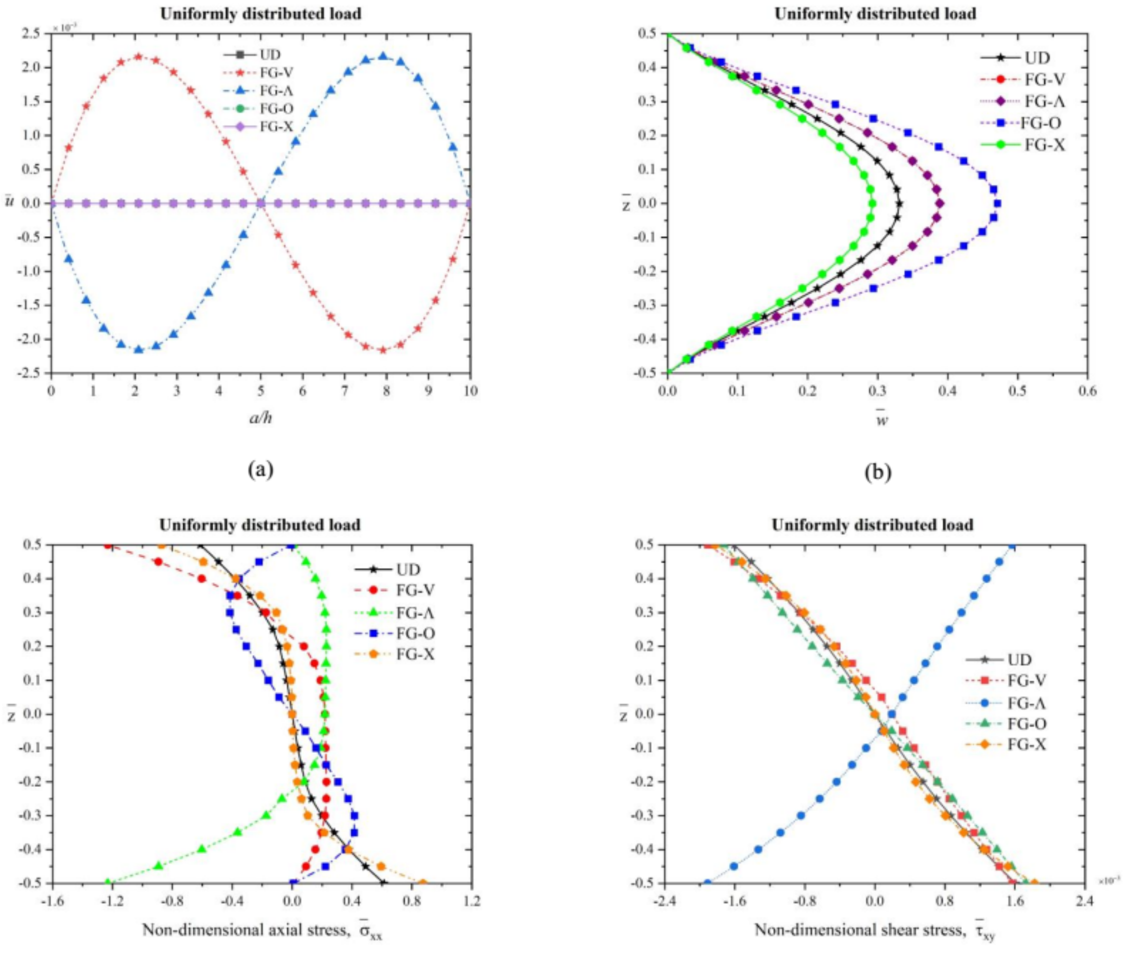

(a) (b)

(c) (d)

Fig. 4-5: Distribution of longitudinal and transverse displacement and in-plane axial and shear stress with five different distributions of CNT, all edge clamped (CCCC) boundary conditions and *a/h* = 50 subjected to UDL at 700 K temperature conditions

The longitudinal and transverse displacement and in-plane axial and shear stresses are presented in Figs. 4.5 (a-d). Fig. 4.5 (a) depicts the effect of CNT distributions on the longitudinal displacement of the FG-CNT reinforced plate. It is concluded that for the corresponding point, symmetric CNT distributions (UD, FG-O and FG-X) are always smaller in magnitude than the other two distributions (FG-V and FG-Λ). Moreover, in-plane longitudinal displacement is not noticeable for the case of symmetric CNT distribution. This is due to the distribution of CNT more on the top and bottom of the plate. From Fig. 4.5 (b), it is observed that displacement due to FG-X distribution in FG-CNT reinforced plate is minimum, followed by UD, FG-V, FG-Λ and FG-O distributions. This is because that the pattern of distribution adopted to reinforce CNT directly affects the stiffness of the plate. Fig. 4.5 (c) and (d) depicts the distribution of in-plane axial and shear stresses across the thickness direction. It is concluded that the symmetric CNT distribution represent symmetric behavior about the neutral axis (i.e. mid-plane). However, this is not the case with FG-V and FG-Λ. This is due to uneven distribution of CNT reinforcement about top and bottom surface.

4.3.2.3. Flexural response of FG-CNTR plate under SSL

In this sub-section, the bending analysis of FG-CNT reinforced plate is performed under sinusoidal loading condition subjected to different set of boundary conditions i.e. SSSS, SCSC, SCSS and CCCC. The temperature dependent material properties are considered to investigate the bending response of FG-CNT reinforced plate. The temperature is taken as 300 K, 500 K and 700 K for the bending analysis. The parametric studies have been conducted to observe the effect of different parameters i.e. span to thickness ratio (a/h = 10, 20 and 50), volume fraction of CNTs (0.11, 0.14 and 0.17), pattern of CNTs distribution (UD, FG-V, Λ, O and X) and different set of boundary conditions (SSSS, SCSC, SCSS and CCCC) on the bending response of FG-CNT reinforced plate.

The non-dimensional central deflection response of FG-CNT reinforced plate is presented in Table 4.9 for different types of CNT distribution pattern (UD and three types of FG) under sinusoidal loading condition. Also, the effect of volume fractions of CNTs (i.e. 0.11, 0.14 and 0.14), span to thickness ratios (a/h = 10, 20 and 50) and different set of boundary conditions on the bending response of FG-CNT reinforced plate. The temperature dependent material properties are considered at 300 K temperature. It has been depicted from the Table 4.9 that as the percentage content of CNTs increased the FG-CNT reinforced plate became stiffer. Thus, as the percentage content (of CNT) is increased corresponding to that the central deflection of the FG-CNT reinforced plate reduces. Also, the effect of CNTs distribution pattern is seen on the bending response of FG-CNT reinforced plate. The central deflection of FG-CNT reinforced plate is minimum for CNT distribution pattern considered as FG-X as compared to other types of distribution (UD, FG-V and FG-O). It is noticed that the non-dimensional central deflection maximum in the case of SSSS boundary condition as compared to other boundary conditions (i.e. SCSS, SCSC and CCCC) under sinusoidal loading condition. Also, the effect of the transverse sinusoidal load is a minimal bending response with CCCC boundary conditions as compare to other boundary conditions.

Table 4.9: Non-dimensional central deflection of the square FG-CNTRC plate for different V^*_{CNT}, *a/h* ratio and boundary constraints subjected to sinusoidal transverse load (temperature dependent properties at 300 K)

V^*_{CNT}	*a/h*	Type of CNT distribution	Non-dimensional central deflection			
			SSSS	SCSC	SCSS	CCCC
0.11	10	UD	2.4947×10^{-3}	1.5819×10^{-3}	1.9809×10^{-3}	1.5273×10^{-3}
		FG-V	2.9512×10^{-3}	1.6907×10^{-3}	2.1974×10^{-3}	1.6225×10^{-3}
		FG-O	3.5951×10^{-3}	1.9757×10^{-3}	2.6105×10^{-3}	1.8790×10^{-3}
		FG-X	2.1238×10^{-3}	1.4799×10^{-3}	1.7917×10^{-3}	1.4298×10^{-3}
	20	UD	2.4699×10^{-2}	9.9265×10^{-3}	1.4786×10^{-2}	9.9608×10^{-3}
		FG-V	3.2583×10^{-2}	1.1852×10^{-2}	1.8440×10^{-2}	1.1835×10^{-2}
		FG-O	4.1366×10^{-2}	1.4650×10^{-2}	2.3104×10^{-2}	1.4559×10^{-2}
		FG-X	1.8654×10^{-2}	8.4481×10^{-3}	1.1996×10^{-2}	8.4913×10^{-3}
	50	UD	0.7913	0.2071	0.3738	0.2087
		FG-V	1.1062	0.2844	0.5208	0.2862
		FG-O	1.4314	0.3701	0.6782	0.3716
		FG-X	0.5535	0.1511	0.2661	0.1522
0.14	10	UD	2.2236×10^{-3}	1.4768×10^{-3}	1.8197×10^{-3}	1.4294×10^{-3}
		FG-V	2.5976×10^{-3}	1.5611×10^{-3}	1.9937×10^{-3}	1.5033×10^{-3}
		FG-O	3.1392×10^{-3}	1.7969×10^{-3}	2.3387×10^{-3}	1.7205×10^{-3}
		FG-X	1.9310×10^{-3}	1.3987×10^{-3}	1.6690×10^{-3}	1.3515×10^{-3}
	20	UD	2.0715×10^{-2}	8.8279×10^{-3}	1.2840×10^{-2}	8.8712×10^{-3}
		FG-V	2.7219×10^{-2}	1.0371×10^{-2}	1.5806×10^{-2}	1.0384×10^{-2}
		FG-O	3.4530×10^{-2}	1.2647×10^{-2}	1.9625×10^{-2}	1.2624×10^{-2}
		FG-X	1.5860×10^{-2}	7.6841×10^{-3}	1.0637×10^{-2}	7.7276×10^{-3}
	50	UD	0.6391	0.1704	0.3040	0.1716
		FG-V	0.8993	0.2328	0.4235	0.2344
		FG-O	1.1691	0.3017	0.5514	0.3037
		FG-X	0.4467	0.1260	0.2183	0.1268
0.17	10	UD	2.0267×10^{-3}	1.3916×10^{-3}	1.6944×10^{-3}	1.3492×10^{-3}
		FG-V	2.3408×10^{-3}	1.4574×10^{-3}	1.8374×10^{-3}	1.4066×10^{-3}
		FG-O	2.7997×10^{-3}	1.6518×10^{-3}	2.1261×10^{-3}	1.5898×10^{-3}
		FG-X	1.7906×10^{-3}	1.3300×10^{-3}	1.5712×10^{-3}	1.2844×10^{-3}
	20	UD	1.7992×10^{-2}	8.0392×10^{-3}	1.1478×10^{-2}	8.0854×10^{-3}
		FG-V	2.3512×10^{-2}	9.3164×10^{-3}	1.3964×10^{-2}	9.3428×10^{-3}
		FG-O	2.9732×10^{-2}	1.1196×10^{-2}	1.7154×10^{-2}	1.1208×10^{-2}
		FG-X	1.3968×10^{-2}	7.1305×10^{-3}	9.6836×10^{-3}	7.1722×10^{-3}
	50	UD	0.5372	0.1458	0.2575	0.1468
		FG-V	0.7586	0.1981	0.3581	0.1995
		FG-O	0.9888	0.2555	0.4655	0.2574
		FG-X	0.3759	0.1093	0.1866	0.1100

The bending response of FG-CNT reinforced plate is presented in Fig. 4.6 and Table 4.10 subjected to sinusoidal load considering temperature dependent material properties at 500 K and 700 K, respectively. Further, Tables 4.9 and 4.10 are compared to observe the effect of temperature dependent material properties on the central deflection of FG-CNTR plate. However, Fig. 4.6 depicts the influence of volume fraction and boundary conditions on the response non-dimensional central deflection for *a/h* = 50 and FG-X distribution of CNT. For the comparison of the results, the following parameters are considered i.e. type of distribution pattern i.e. UD, volume fraction of CNTs as 0.11, *a/h* =10 and all edges simply supported (SSSS).

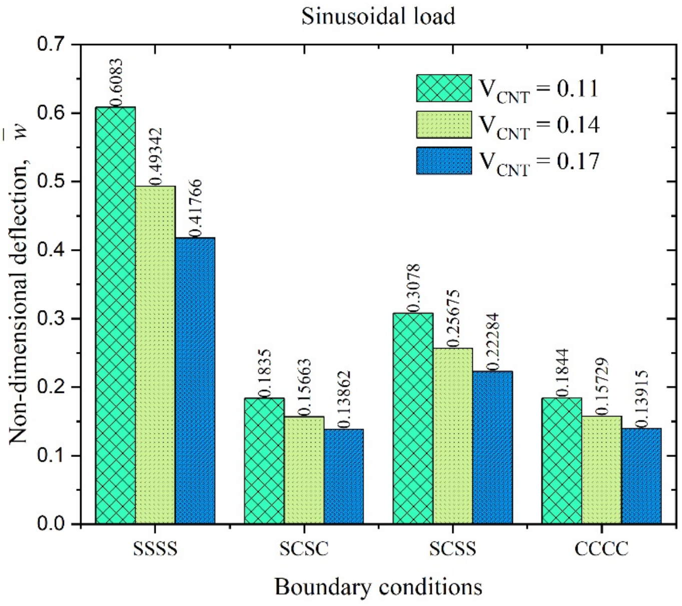

Fig. 4-6: Non-dimensional deflection of FG-CNT reinforced plate with *a/h*=50 subjected to sinusoidal load at 500 K temperature conditions

It has been concluded from the Tables 4.9 and 4.10 that with increase in temperature from 300 K to 700 K, the central deflection of FG-CNTR plate increases by 450% in comparison to considered material properties at 300 K. From Fig. 4.6, it is observed that with increase in volume fraction of CNT from 0.11 to 0.17, the central deflection decreased by 31.3%. Moreover, influence of boundary conditions is investigated by comparison of SSSS and CCCC for 0.11 volume fraction. It is concluded that non-dimensional central deflection decrease by 70 % due to change in boundary conditions from SSSS to CCCC. This is due to the type of constraint implemented for all edges clamped boundary condition (CCCC). Thus, it has been concluded that the bending is significantly influenced by considering temperature dependent material properties, volume fraction and boundary conditions. As the temperature is increased from 300 K to 700 K, the central deflection of FG-CNT reinforced plate is increased substantially. Moreover, by increasing the volume fraction of CNT to 0.17 and CCCC boundary conditions significantly decreases the non-dimensional central deflection for the same temperature conditions.

Table 4.10: Non-dimensional central deflection of the square CNTRC plate for different volume fraction (V_{CNT}^{*}), *a/h* ratio, and boundary constraints subjected to sinusoidal transverse load (TD properties at 700 K)

V_{CNT}^{*}	*a/h*	Type of CNT distribution	Non-dimensional central deflection			
			SSSS	SCSC	SCSS	CCCC
0.11	10	UD	1.3727×10^{-2}	1.2065×10^{-2}	1.3119×10^{-2}	1.1813×10^{-2}
		FG-V	1.4291×10^{-2}	1.2147×10^{-2}	1.3467×10^{-2}	1.1884×10^{-2}
		FG-O	1.6634×10^{-2}	1.3156×10^{-2}	1.5052×10^{-2}	1.2858×10^{-2}
		FG-X	1.3121×10^{-2}	1.1849×10^{-2}	1.2670×10^{-2}	1.1572×10^{-2}
	20	UD	7.4944×10^{-2}	5.5143×10^{-2}	6.5568×10^{-2}	5.5593×10^{-2}
		FG-V	8.5183×10^{-2}	5.7236×10^{-2}	7.0468×10^{-2}	5.7700×10^{-2}
		FG-O	1.0417×10^{-1}	6.6056×10^{-2}	8.3148×10^{-2}	6.6586×10^{-2}
		FG-X	6.7027×10^{-2}	5.2921×10^{-2}	6.1033×10^{-2}	5.3347×10^{-2}
	50	UD	1.1926	0.5193	0.7482	0.5199
		FG-V	1.6060	0.6087	0.9260	0.6098
		FG-O	2.0766	0.7515	1.1655	0.7534
		FG-X	0.9070	0.4533	0.6205	0.4537
0.14	10	UD	1.2940×10^{-2}	1.1555×10^{-2}	1.2450×10^{-2}	1.1318×10^{-2}
		FG-V	1.3348×10^{-2}	1.1572×10^{-2}	1.2694×10^{-2}	1.1329×10^{-2}
		FG-O	1.5252×10^{-2}	1.2352×10^{-2}	1.3966×10^{-2}	1.2103×10^{-2}
		FG-X	1.2475×10^{-2}	1.1349×10^{-2}	1.2073×10^{-2}	1.1076×10^{-2}
	20	UD	6.8339×10^{-2}	5.2076×10^{-2}	6.1003×10^{-2}	5.2502×10^{-2}
		FG-V	7.6313×10^{-2}	5.3565×10^{-2}	6.4871×10^{-2}	5.4001×10^{-2}
		FG-O	9.1689×10^{-2}	6.0645×10^{-2}	7.5182×10^{-2}	6.1143×10^{-2}
		FG-X	6.2403×10^{-2}	5.0381×10^{-2}	5.7440×10^{-2}	5.0784×10^{-2}
	50	UD	1.0008	0.4675	0.6562	0.4679
		FG-V	1.3268	0.5372	0.7963	0.5380
		FG-O	1.7011	0.6515	0.9874	0.6528
		FG-X	0.7784	0.4176	0.5573	0.4179
0.17	10	UD	1.2277×10^{-2}	1.1086×10^{-2}	1.1866×10^{-2}	1.0862×10^{-2}
		FG-V	1.2562×10^{-2}	1.1036×10^{-2}	1.2017×10^{-2}	1.0809×10^{-2}
		FG-O	1.4103×10^{-2}	1.1647×10^{-2}	1.3042×10^{-2}	1.1435×10^{-2}
		FG-X	1.1897×10^{-2}	1.0864×10^{-2}	1.1524×10^{-2}	1.0592×10^{-2}
	20	UD	6.3376×10^{-2}	4.9472×10^{-2}	5.7321×10^{-2}	4.9876×10^{-2}
		FG-V	6.9805×10^{-2}	5.0480×10^{-2}	6.0415×10^{-2}	5.0891×10^{-2}
		FG-O	8.2349×10^{-2}	5.6149×10^{-2}	6.8815×10^{-2}	5.6615×10^{-2}
		FG-X	5.8837×10^{-2}	4.8092×10^{-2}	5.4433×10^{-2}	4.8474×10^{-2}
	50	UD	0.8720	0.4298	0.5915	0.4301
		FG-V	1.1406	0.4863	0.7066	0.4868
		FG-O	1.4484	0.5792	0.8629	0.5800
		FG-X	0.6922	0.3910	0.5124	0.3913

Further, a study is conducted to investigate the response of displacement and stresses with five different distributions of CNT subjected to sinusoidal loading conditions. The response of the FG-CNTR plate, all edged clamped boundary conditions and *a/h* = 50 is presented in Figs. 4.7 (a-d) at 700 K temperature conditions.

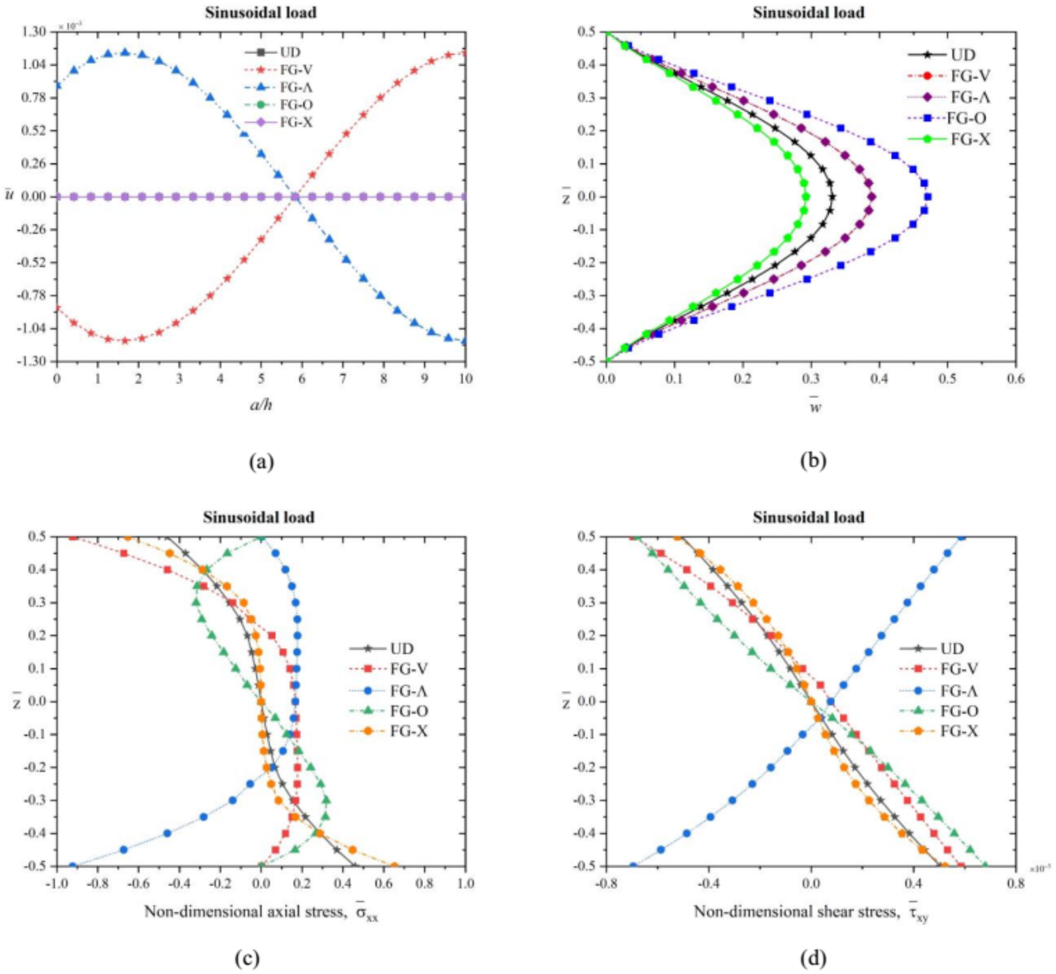

(a) (b)

(c) (d)

Fig. 4-7: Distribution of longitudinal and transverse displacement and in-plane axial and shear stress with five different distributions of CNT, all edge clamped (CCCC) boundary conditions and *a/h* = 50 subjected to SSL at 700 K temperature condition

It is observed from Fig 4.7 (a) that longitudinal displacement magnitude is minimal for symmetric CNT distribution (UD, FG-O and FG-X). At the same time, it is a significant variation for the FG-V and FG-Λ with an increment of *a/h* ratio, respectively. Fig. 4.7 (b), (c) and (d) depicts the response of transverse displacement and in-plane stresses (σ_{xx} and τ_{xy}) along the thickness direction. It is observed that transverse displacement is minimum for FG-X distribution and maximum for FG-O. It is seen that in-plane stress distributions for all CNT distributions are non-linear. However, symmetric behavior is observed for the symmetric CNT distributions (UD, FG-O and FG-X) about the neutral axis (i.e. mid-plane).

4.4. Buckling Response of the FG-CNTRC Plate

In this section, the IHSDT is implemented for buckling behavior of temperature-dependent FG-CNTRC plate subjected to uni-axial as well as bi-axial in plane compressive and tensile loading. A MATLAB code based on the theoretical formulation discussed in Chapter 3, is developed and implemented to examine the buckling response in different temperature conditions. In this view, closed form solution is first obtained and validated for simply supported boundary condition with existing literature at 300 K. Further, in order to ensure applicability of IHSDT to various boundary condition, the numerical finite element solution is obtained. The buckling response is examined for various volume fraction, span-thickness ratio (*a/h*), distribution of CNT, and boundary conditions under different temperature conditions.

4.4.1. Analytical solution

In order to study the buckling behavior, a square plate with gradation of CNT along the thickness for SSSS boundary condition exposed to in-plane compressive load is considered. The buckling response is predicted for different volume fraction of CNT, span-thickness ratio (*a/h*), and aspect ratio (*a/b*) in the present work. The properties of PmPV matrix and CNT material are taken same as indicated in Section 4.3. Also, effect of biaxial loading condition on the FG-CNTRC plate is examined in the present work. The results are presented for the buckling load parameter (λ_{cr}) expressed in non-dimensional form as follows.

$$\lambda_{cr} = \lambda b^2 / E_m h^3 \tag{4.1}$$

The uniaxial non-dimensional buckling parameter for FG-CNTRC simply supported square plates is presented in Table 4.11 under the action of in-plane compressive forces. For the analysis, four different types of CNT (UD, FG-V, FG-O and FG-X) distributions are considered in the square plate. Also, the influence of volume fraction of CNT and span-thickness ratio on the buckling response is depicted in Table 4.11. The comparison of the computed results for the considered plate with the existing results in the literature is also shown in Table 4.11. The material properties are considered at temperature 300 K. The numerical results are compared with the existing results due to Hajlaoui, *et al.* [105], Malekzadeh and Shojaee, [106], Zhang, *et al.* [107] and Kiani, Y., [56]. It is clearly seen that the results obtained by the present model are found good in agreement with the results reported in the literature. It is also noted that with increase in the volume fraction of CNT, the value of non-dimensional buckling parameter increase. The increment is due to increase in the stiffness of the FG-

CNTRC plate due to addition of CNT. The influence of CNT distribution indicates that the plate with FG-X distribution possesses the highest bucking load parameter followed by UD, FG-V and FG-O. It is also noted that the results provided in the literature are in the framework of FSDT and the present results are based upon the IHSDT which is more accurate and efficient than the FSDT. Moreover, the comparison is also made with the isotropic plate and it is found that for a plate (*a/h* = 10) with volume fraction as 0.11, the buckling load is 2.67, 2.1, 1.52 and 3.36 times the buckling load of the isotropic plate for UD, FG-V, FG-O and FG-X distribution, respectively.

Table 4.11: Uniaxial non-dimensional buckling load parameter for simply supported square FG-CNTRC plate with various volume fraction (V^*_{CNT}) and *a/h* ratio

V^*_{CNT}	*a/h*	CNT distribution	Present	Hajlaoui, *et al.* [105]	Malekzadeh and Shojaee [106]	Zhang *et al.* [107]	Kiani, Y. [56]
0.11	10	Isotropic	5.3337	-	-	-	-
		UD	19.6057	18.823	-	18.9783	18.9825
		FG-V	16.5249	-	-	-	-
		FG-O	13.4177	13.925	-	13.8356	13.7938
		FG-X	23.256	19.285	-	22.1612	22.1655
	20	Isotropic	5.5557	-	-	-	-
		UD	31.3701	31.003	31.5258	30.9221	31.0703
		FG-V	23.7517	-	-	-	-
		FG-O	18.657	18.933	19.0745	18.7618	18.8456
		FG-X	41.7042	40.282	41.7608	40.8422	41.0295
	50	Isotropic	5.6213	-	-	-	-
		UD	38.1236	38.082	-	37.7998	38.06
		FG-V	27.265	-	-	-	-
		FG-O	21.061	21.117	-	20.9312	21.0904
		FG-X	54.5445	54.234	-	54.0305	54.3867
	100	Isotropic	5.6308	-	-	-	-
		UD	39.3506	39.384	39.3633	39.1158	39.3391
		FG-V	27.8617	-	-	-	-
		FG-O	21.4606	21.481	21.4831	21.3316	21.4639
		FG-X	57.0941	57.09	57.1056	56.7373	57.0671
0.14	10	UD	22.2188	-	-	-	-
		FG-V	18.9505	-	-	-	-
		FG-O	15.475	-	-	-	-
		FG-X	25.7986	-	-	-	-
	20	UD	37.6927	37.22	37.8893	-	-
		FG-V	28.6398	-	-	-	-
		FG-O	22.501	22.946	23.0399	-	-
		FG-X	49.4073	47.541	49.7596	-	-
		UD	47.5273	-	-	-	-

	50	FG-V	33.7601	-	-	-	-
		FG-O	25.9555	-	-	-	-
		FG-X	68.0507	-	-	-	-
	100	UD	49.3973	49.438	49.4162	49.0816	-
		FG-V	34.6587	-	-	-	-
		FG-O	26.5446	26.578	23.0399	26.3572	-
		FG-X	72.0005	71.976	72.0432	71.5516	-
0.17	10	UD	30.6207	-	-	-	-
		FG-V	25.7145	-	-	-	-
		FG-O	21.0693	-	-	-	-
		FG-X	35.8832	-	-	-	-
	20	UD	48.5279	-	-	-	-
		FG-V	36.5565	-	-	-	-
		FG-O	28.7366	-	-	-	-
		FG-X	64.3043	-	-	-	-
	50	UD	58.6427	-	-	-	-
		FG-V	41.7363	-	-	-	-
		FG-O	32.1446	-	-	-	-
		FG-X	84.1186	-	-	-	-
	100	UD	60.4677	-	-	-	-
		FG-V	42.61	-	-	-	-
		FG-O	32.7044	-	-	-	-
		FG-X	88.0565	-	-	-	-

Further, a SSSS FG-CNTRC plate is considered for the evaluation of non-dimensional uniaxial and biaxial buckling load parameter with temperature dependent properties. The effect of volume fraction (0.11, 0.14 and 0.17), span-thickness ratio (10, 50 and 100) and temperature (300 K, 500 K and 700 K) are studied on uniaxial and biaxial non-dimensional buckling load parameter. The results are obtained for the various distribution of CNT (UD, FG-V, FG-O and FG-X) and listed in Table 4.12. It is clearly observed that as the temperature increases, the buckling parameter increases for both uniaxial as well as biaxial loading conditions. In addition, the most effective configuration is FG-X while FG-O is the least effective as evident through Table 4.12. Further, the effect of volume fraction of CNT is clearly visible on the buckling load parameter. The buckling load parameter increases due to increase in the volume fraction of CNT. The influence of span-thickness ratio indicate that the thin plate possesses higher non-dimensional buckling load relative to the thick plate for a specific volume fraction and CNT distribution.

Table 4.12: Effect of temperature dependent material properties on the uniaxial and biaxial buckling parameter for simply supported square FG-CNTRC plate with different volume fraction (V^*_{CNT}) and *a/h* ratio

V^*_{CNT}	*a/h*	Type of CNT distribution	*T* = 300 K		*T* = 500 K		*T* = 700 K	
			$\lambda_1 = 0$	$\lambda_1 = 1$	$\lambda_1 = 0$	$\lambda_1 = 1$	$\lambda_1 = 0$	$\lambda_1 = 1$
0.11	10	UD	19.6057	9.8028	24.383	12.1915	38.5536	19.2768
		FG-V	16.5249	8.2624	21.2732	10.6366	36.7143	18.3572
		FG-O	13.4177	6.7088	17.2443	8.6222	28.1178	14.0589
		FG-X	23.256	11.628	27.9318	13.9659	42.0998	21.0499
	50	UD	38.1236	19.0618	62.9728	31.4864	242.6907	121.3453
		FG-V	27.265	13.6325	44.4587	22.2294	179.9348	89.9674
		FG-O	21.061	10.5305	34.0695	17.0348	138.6082	69.3041
		FG-X	54.5445	27.2722	89.9583	44.9792	320.9776	160.4888
	100	UD	39.3506	19.6753	66.5244	33.2622	308.1422	154.0711
		FG-V	27.8617	13.9308	46.1535	23.0767	213.2976	106.6488
		FG-O	21.4606	10.7303	35.2071	17.6035	161.6361	80.818
		FG-X	57.0941	28.5471	97.3054	48.6527	442.1637	221.0818
0.14	10	UD	22.2188	11.1094	27.1801	13.59	42.6508	21.3254
		FG-V	18.9505	9.4752	24.0524	12.0262	40.904	20.452
		FG-O	15.475	7.7375	19.6601	9.83	31.2184	15.6092
		FG-X	25.7986	12.8993	30.4741	15.237	46.1311	23.0655
	50	UD	47.5273	23.7637	78.5688	39.2844	291.5918	145.7959
		FG-V	33.7601	16.8801	55.4162	27.7081	219.4752	109.7376
		FG-O	25.9555	12.9777	42.403	21.2015	170.3553	85.1777
		FG-X	68.0507	34.0253	111.6755	55.8377	376.7398	188.3699
	100	UD	49.3973	24.6986	83.982	41.991	385.9833	192.9917
		FG-V	34.6587	17.3294	57.9915	28.9957	268.5659	134.2829
		FG-O	26.5446	13.2723	44.099	22.0495	203.9447	101.9723
		FG-X	72.0005	36.0003	122.9766	61.4883	548.3741	274.187
0.17	10	UD	30.6207	15.3104	38.2486	19.1243	60.6757	30.3379
		FG-V	25.7145	12.8573	33.3092	16.6546	57.8392	28.9196
		FG-O	21.0693	10.5347	27.4553	13.7276	45.7712	22.8856
		FG-X	35.8832	17.9416	43.0577	21.5288	64.8187	32.4093
	50	UD	58.6427	29.3213	97.1824	48.5912	377.578	188.789
		FG-V	41.7363	20.8681	68.3853	34.1926	279.42	139.71
		FG-O	32.1446	16.0723	52.3648	26.1824	216.7892	108.3946
		FG-X	84.1186	42.0593	138.8018	69.4009	494.5593	247.2797
	100	UD	60.4677	30.2338	102.5028	51.2514	477.0128	238.5064
		FG-V	42.61	21.305	70.8969	35.4485	329.805	164.9025
		FG-O	32.7044	16.3522	53.9793	26.9896	250.3523	125.1761
		FG-X	88.0565	44.0282	150.1869	75.0935	682.5087	341.2544

The influence of volume fraction on the uniaxial buckling load parameter of FG-CNT reinforced simply supported square plate with *a/h* = 10 at 300 K temperature is illustrated in Fig. 4.8 (a). Four type of distributions considered are UD, FG-V, FG-O and FG-X for the analysis. It is observed that the buckling load parameter for the case of FG-X distribution is more effected by the variation of volume fraction and FG-O is least effected. The plate has higher value of buckling load parameter when the volume fraction in CNT reinforced plate is large fraction. Fig. 4.8 (b) depicts the influence of volume fraction on the biaxial buckling load parameter of FG-CNTRC square plate with SSSS conditions and *a/h* = 100 at 300 K temperature. It is observed that, at low volume fraction the buckling parameter is low which mean, it can withstand less load and as the volume fraction increases, the buckling parameter also increases. Moreover, the thin plate (*a/h* =100) possess higher buckling load relative to thick plate (*a/h* =10) for a specific configuration and CNT volume fraction.

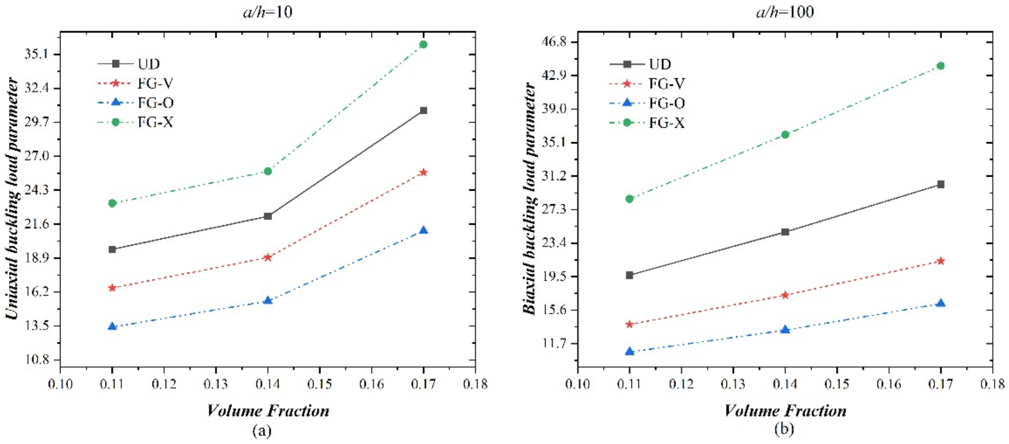

Fig. 4-8: Non-dimensional uniaxial and biaxial buckling load parameter versus volume fraction for the FG-CNTRC plate (a) *a/h* = 10 at *T* = 300 K (b) *a/h* = 100 at *T* = 300 K

Furthermore, the rectangular CNTRC plates are considered exposed to biaxial compression and the results are obtained considering diverse specifications including aspect ratio, *a/h* ratio, temperature and distribution of CNT. Table 4.13 depicts the effect of aspect ratio on the biaxial buckling parameter of FG-CNTRC plate with SSSS conditions. The aspect ratio is considered as 1.2, 1.5 and 2. The effect of different temperature (300 K, 500 K and 700 K) and span to thickness ratio (*a/h* = 10, 20, and 100) are also considered. The results are obtained for various distribution of CNT (UD, FG-V, FG-O and FG-X). It is noted that as the temperature increase from 300 K to 700 K, the buckling parameter increases. It is also noted that the buckling parameter decreases due to increment in the aspect ratio. Further, the CNT distribution FG-X shows the maximum buckling load parameter followed by UD, FG-V and

FG-O. This is due to maximum stiffness at the top and bottom surface of plate in FG-X configuration.

Table 4.13: Non dimensional biaxial buckling parameter for simply supported square FG-CNTRC plate considering the effect of different aspect ratio, *a/h* ratio with volume fraction (V_{CNT}^{*}) equal to 0.11

a/*b*	*a/h*	Type of CNT distribution	*T* = 300 K	*T* = 500 K	*T* = 700 K
0.5	10	UD	24.3758	28.2735	51.7733
		FG-V	22.4452	26.6902	50.6457
		FG-O	18.0226	20.8434	32.1855
		FG-X	26.8941	30.8879	58.0808
	20	UD	58.0041	73.7264	119.8007
		FG-V	47.7224	63.3985	113.7506
		FG-O	37.8292	50.5014	86.1874
		FG-X	69.8142	85.1825	131.1187
	100	UD	115.1715	194.8212	770.8015
		FG-V	80.2004	135.3243	569.5681
		FG-O	60.7678	102.48	437.5635
		FG-X	167.4292	280.9481	1.0214×10^{3}
1	10	UD	9.8028	12.1915	19.2768
		FG-V	8.2624	10.6366	18.3572
		FG-O	6.7088	8.6222	14.0589
		FG-X	11.628	13.9659	21.0499
	20	UD	15.685	23.0403	50.7535
		FG-V	11.8759	17.7522	44.4423
		FG-O	9.3285	13.9298	35.3634
		FG-X	20.8521	29.6428	57.763
	100	UD	19.6753	33.2622	154.0711
		FG-V	13.9308	23.0767	106.6488
		FG-O	10.7303	17.6035	80.818
		FG-X	28.5471	48.6527	221.0818
1.2	10	UD	6.9431	8.8802	14.4885
		FG-V	5.7616	7.5746	13.6166
		FG-O	4.6983	6.1579	10.7097
		FG-X	8.4139	10.3938	15.849
	20	UD	9.9916	14.9505	36.6493
		FG-V	7.5655	11.3535	31.1354
		FG-O	5.9873	8.9229	24.7562
		FG-X	13.4365	19.6713	42.6897
	100	UD	11.7298	19.5348	90.6807
		FG-V	8.4559	13.6937	62.3826
		FG-O	6.593	10.5258	47.2623
		FG-X	16.8489	28.4462	131.4342
1.5	10	UD	4.3693	5.7178	9.9186
		FG-V	3.6168	4.7864	9.1377
		FG-O	2.9887	3.9202	7.35
		FG-X	5.3871	6.861	10.9423
	20	UD	5.611	8.3851	22.9253
		FG-V	4.3334	6.3629	18.7644
		FG-O	3.4953	5.0518	14.8783
		FG-X	7.5339	11.2059	27.6
	100	UD	6.2078	9.9861	45.1593
		FG-V	4.6426	7.1711	31.0212
		FG-O	3.7059	5.6025	23.559
		FG-X	8.7173	14.3507	65.8916
2	10	UD	2.4085	3.1175	5.8069

		FG-V	2.06	2.6227	5.201
		FG-O	1.7592	2.1991	4.2662
		FG-X	2.9551	3.8025	6.5337
	20	UD	2.7629	3.9159	11.3075
		FG-V	2.2688	3.0796	8.9175
		FG-O	1.9073	2.5228	7.077
		FG-X	3.5863	5.1879	14.1956
	100	UD	2.9081	4.2972	17.451
		FG-V	2.3485	3.2751	12.1271
		FG-O	1.9625	2.6563	9.3085
		FG-X	3.8701	5.9471	25.415

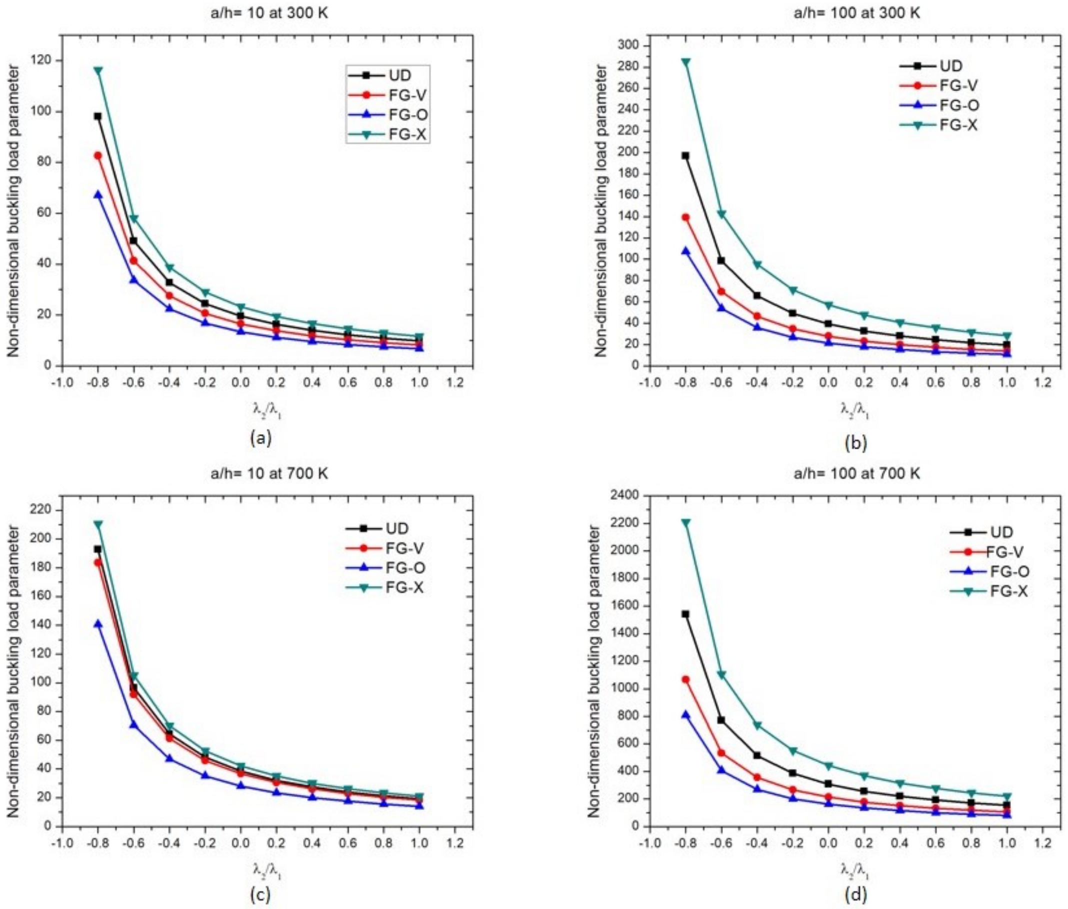

(a) (b)

(c) (d)

Fig. 4-9: Non-dimensional buckling parameter versus biaxial/uniaxial ratio for the SSSS FG-CNTRC plate with (a) *a/h* = 10 at *T* = 300 K, (b) *a/h* = 100 at *T* =300 K (c) *a/h* = 10 at *T* =700 K and (d) *a/h* = 100 at *T* = 700 K

The effect of biaxial load index ($k=\lambda_2/\lambda_1$) is examined on the buckling parameter behavior of the considered CNTRC plates. The value of *k* is chosen from -0.8 to 1. The negative value of *k* corresponds to axial tensile forces acting in *y*-direction. The uniaxial and biaxial compression corresponds to *k* = 0 and *k* = 1 respectively. The study is carried out for the thick as well as for the thin plates (*a/h* = 10 and 100) with volume fraction 0.11 while considering the temperature dependent properties of the constituents. Two different temperature condition at 300 K and 700 K are assumed. The buckling parameter is obtained for the considered example and the results are depicted in Fig 4.9. It is observed from the figure that the buckling parameter decreases due to increase in load index (k). This is due to the fact that the k increases the overall compressive force, thereby the reduction in the buckling parameter occurs. It is also noted that for negative value of k, the buckling load is higher than that of $k = 0$. This is because the negative value of k corresponds to axial tensile force, thereby reducing the overall compressive force and hence an increase in the buckling parameter is observed. The buckling load increases due to increase in a/h ratio at a particular temperature. The plate with FG-X distribution have highest buckling load followed by UD, FG-V and FG-O. For a particular a/h ratio, the plate at $T = 700$ K possesses higher buckling parameter related to the corresponding parameter at $T = 300$ K.

4.4.2. Finite element solution

This subsection presents the detailed numerical results on the basis of developed formulation for buckling characteristics of FG-CNT reinforced plates in the FE framework of IHSDT. The convergence and validation studies are first carried out to ascertain the accuracy and consistency of computer code that has been developed in MATLAB on the basis of the developed FE framework. Further, detailed numerical investigations are conducted to examine the effect of various specifications including the volume fraction of CNTs, span-thickness ratio, distribution of CNT and boundary conditions on the buckling response of temperature dependent FG-CNTRC plates. In this study, the material properties of the matrix and reinforced CNT are considered as temperature-dependent. The properties of the PmPV matrix and CNT material are taken same as indicated in Section 4.3. The different set of boundary conditions which include all edges simply-supported (SSSS), all edge clamped (CCCC), one side clamped and the other three edges simply-supported (SCSS), and two edges simply-supported and two edges clamped (SCSC) are considered. The boundary constraints associated with clamped and simply supported boundary are given as follows:

Clamped conditions (C): $u_\circ = v_\circ = w_\circ = \theta_x = \theta_y = \phi_x = \phi_y = 0$

Simply-supported conditions (S):

$$u_\circ = w_\circ = \theta_x = \phi_x = 0 \quad \text{at } y = 0 \text{ and } y = b$$
$$v_\circ = w_\circ = \theta_y = \phi_y = 0 \quad \text{at } x = 0 \text{ and } x = a$$

4.4.2.1. Convergence Study

In order to ensure the convergence behavior of the developed FE formulation, uniformly distributed CNT reinforced plate constraint with a variety of boundary conditions (SSSS, SCSS, SCSC, and CCCC) is considered. The geometrical properties are *a/h*=10, uniformly distributed CNT with $V_{CNT}^{*} = 0.11$ and the properties of matrix and CNT are considered at 300K temperature. The buckling load parameter $\bar{\lambda}_{cr} = \lambda b^2 / \left(E_m h^3\right)$ is investigated under uniaxial compression for the different mesh size from (2 × 2) to (10 × 10). The non-dimensional results are plotted in Fig. 4.10 for the considered mesh sizes and different boundary conditions. It is clear from the response of the buckling load parameter for different boundary conditions that a good convergence is attained at mesh size (10 × 10). Thus, from the above responses of buckling load parameter, the plates are discretized with a mesh of (10 × 10) for the further analyses in FE framework.

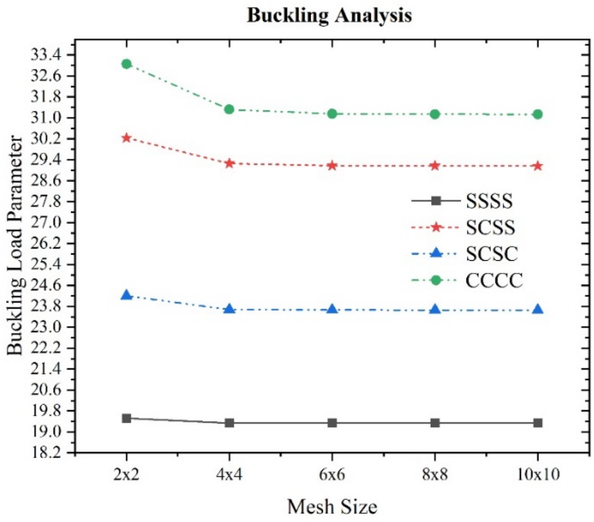

Fig. 4-10: Convergence study for the buckling load of FG-CNTRC plate for different mesh size and boundary conditions under uniaxial compression

4.4.2.2. Validation

In this study, the validation for the present results is ascertained to ensure the accuracy of the IHSDT based FE model for buckling response of CNTRC plates. For the comparison, FG-CNT reinforced plate is considered with SSSS conditions. The buckling parameters of a FG-CNT reinforced plates with different volume fractions of CNT (0.11, 0.14, and 0.17), span to thickness ratios (*a/h* = 10, 20 and 50) and CNT distribution (UD, FG-V, FG-O and FG-X) under the action of uniaxial compressive forces $(\gamma_1 = -1, \gamma_2 = 0)$ are computed and presented in Table 4.14. The buckling load parameters are also compared with the exact solution presented by Malekzadeh and Shojaee [106], FSDT based FE numerical solutions presented by Hajlaoui *et al.* [105] and Y. Kiani [56], and element-free IMLS-Ritz solutions presented by Zhang *et al.* [107] in Table 4.14. The comparison of the present FE results is also done with the present CFS results and it is noticed that the FE results agree well with the corresponding CFS results. It is concluded from the results that the IHSDT provides more accurate response than FSDT based numerical solutions. It is due to consideration of more realistic shear deformation expressed though inverse hyperbolic function. It is also noticed that the buckling parameter increases due to increase in *a/h* ratio and volume fraction of CNT.

Table 4.14: Non dimensional buckling parameter for square FG-CNT reinforced plate with SSSS conditions under the action of uniaxial compressive forces $(\gamma_1 = -1, \gamma_2 = 0)$ at 300 K temperature

V^*_{CNT}	*a/h*	Type of CNT distribution	Present	IHSDT (CFS)	Hajlaoui, *et al.* [105]	Zhang *et al.* [107]	Y. Kiani [56]	Malekzadeh and Shojaee [106]
0.11	10	UD	19.3336	19.6057	18.823	18.9783	18.9825	-
		FG-V	16.3431	16.5249	-	-	-	-
		FG-O	13.4161	13.4177	13.925	13.8356	13.7938	-
		FG-X	22.7098	23.256	19.285	22.1612	22.1655	-
	20	UD	31.2460	31.3701	31.003	30.9221	31.0703	31.5258
		FG-V	23.6855	23.7517	-	-	-	-
		FG-O	18.6561	18.657	18.933	18.7618	18.8456	19.0745
		FG-X	41.3707	41.7042	40.282	40.8422	41.0295	41.7608
	50	UD	38.0982	38.1236	38.082	37.7998	38.06	-
		FG-V	27.2532	27.265	-	-	-	-
		FG-O	21.0612	21.061	21.117	20.9312	21.0904	-
		FG-X	54.4623	54.5445	54.234	54.0305	54.3867	-
	100	UD	39.3447	39.3506	39.384	39.1158	39.3391	39.3633
		FG-V	27.8592	27.8617	-	-	-	-
		FG-O	21.4610	21.4606	21.481	21.3316	21.4639	21.4831
		FG-X	57.0730	57.0941	57.09	56.7373	57.0671	57.1056
0.14	10	UD	21.8460	22.2188	-	-	-	-
		FG-V	18.6988	18.9505	-	-	-	-
		FG-O	15.4721	15.4750	-	-	-	-
		FG-X	25.1587	25.7986	-	-	-	-
	20	UD	37.5124	37.6927	37.22	-	-	37.8893
		FG-V	28.5447	28.6398	-	-	-	-
		FG-O	22.5006	22.501	22.946	-	-	23.0399
		FG-X	48.9985	49.4073	47.541	-	-	49.7596
	50	UD	47.4885	47.5273	-	-	-	-
		FG-V	33.7426	33.7601	-	-	-	-
		FG-O	25.9558	25.9555	-	-	-	-
		FG-X	67.9428	68.0507	-	-	-	-
	100	UD	49.3880	49.3973	49.438	49.0816	-	49.4162
		FG-V	34.6549	34.6587	-	-	-	-
		FG-O	26.5453	26.5446	26.578	26.3572	-	23.0399
		FG-X	71.9722	72.0005	71.976	71.5516	-	72.0432

4.4.2.3. Parametric studies

In this study, the effect of temperature-dependent material properties on the buckling load of the FG-CNTRC plate under the action of uniaxial compressive $\left(\gamma_1 = -1, \gamma_2 = 0\right)$ is examined along with the influence of other parameters including boundary constraints, span-thickness ratio, CNT volume fraction, and distribution pattern of CNT. The examination is performed for different boundary condition (SSSS, SCSS, SCSC, and CCCC) and considering temperature dependent properties at 300 K, 500 K, and 700 K. The computed results in terms of non-dimensional buckling parameter are listed in Table 4.15. It is concluded from the Table 4.15 that due to the increase in temperature from 300 K to 500 K, the buckling parameter increases by 19.38% in comparison to material properties considered at 300 K (V^*_{CNT} = 0.11, UD-CNT and SSSS boundary condition). Moreover, the buckling parameter increase by 73.47 % when increasing the temperature conditions from 300 K to 700 K (V^*_{CNT} = 0.11, UD-CNT and SSSS boundary condition). Thus, it has been observed that temperature-dependent material properties have significant impact on the buckling response of the FG-CNT reinforced plate. Further, it has been observed (from Table 4.15) that buckling parameter increases with the increase in volume fraction from 0.11 to 0.17. The effect of boundary conditions discloses that the FG-CNT reinforced plate with all edges clamped (CCCC) possess highest buckling parameter relative to other three boundary conditions. The buckling parameter increases due to increase in span-thickness ratio for a specific volume fraction and distribution of CNT and specific boundary condition.

Further, investigations are performed to predict the effect of the volume fraction of CNT on the buckling parameter for different boundary conditions. The analysis has been conducted for a/h = 10, FG-X distribution, and the material properties are considered at 300 K. The obtained results are depicted in Fig. 4.11. The results reveal that due to increment in the CNT volume fraction, the buckling parameter is significantly increased. Consider a case when all the edges of FG-CNT plates are simply supported (SSSS) and volume fraction of CNT is increased from 14 % to 28 %, correspondingly the buckling parameter is increased by 91 %. The influence of the boundary constraints suggests that the FG-CNTRC plate with all edges clamped is most suitable for biaxial compressive load as compared to other boundary conditions. An FG-CNTRC plate (V^*_{CNT}= 0.11) with boundary condition as SSSS and temperature dependent material properties at 300 K temperature is further considered and the obtained results are presented in Fig. 4.12. Moreover, the effect of span to thickness ratio is investigated on the buckling load parameter of the FG-CNT reinforced plate. It has been concluded that the buckling parameter increases due to increment the in span-thickness ratio. Also, it has been predicted that CNT distribution i.e. FG-X is more suitable for these conditions, followed by UD, FG-V, and the least preferred is FG-O distribution. This is because the distribution of CNTs along the top and bottom surfaces enhances the overall stiffness of the FG-CNTRC plate significantly.

Table 4.15: Effect of temperature-dependent material properties on the buckling response of square CNTRC plate under the action of uniaxial compression with different volume fraction (V_{CNT}^{*}), *a/h* ratio and boundary constraints

V^{*}_{CNT}	*a/h*	CNT distribution	300 K				500 K				700 K			
			SSSS	SCSS	SCSC	CCCC	SSSS	SCSS	SCSC	CCCC	SSSS	SCSS	SCSC	CCCC
0.11	10	UD	19.334	23.659	29.162	31.133	23.802	27.279	32.149	33.984	33.539	34.982	37.551	38.407
		FG-V	16.343	21.105	27.051	29.122	20.850	25.092	30.610	32.564	32.216	34.057	37.242	38.180
		FG-O	13.416	17.599	22.863	24.894	17.242	21.136	26.186	28.163	27.678	30.164	34.039	35.708
		FG-X	22.710	26.405	31.388	33.323	26.883	29.629	33.868	35.576	35.090	36.238	38.263	39.049
	20	UD	31.246	48.601	71.897	74.594	45.772	65.521	90.320	92.970	98.299	111.022	130.199	132.704
		FG-V	23.686	38.392	59.430	62.213	35.331	53.780	78.062	80.785	86.483	102.648	124.728	127.288
		FG-O	18.656	30.444	47.706	50.338	27.857	43.089	63.544	66.131	70.720	85.962	106.477	108.951
		FG-X	41.371	60.822	85.572	88.392	58.520	78.329	102.766	105.534	109.909	119.753	136.310	138.910
	50	UD	38.098	71.274	127.937	130.943	62.898	115.430	200.121	203.093	241.301	363.288	518.858	521.682
		FG-V	27.253	50.916	92.545	95.662	44.424	82.800	147.392	150.469	179.199	288.813	436.664	439.563
		FG-O	21.061	39.043	70.963	73.855	34.069	63.482	113.619	116.484	138.585	227.765	350.517	353.259
		FG-X	54.462	100.728	176.873	180.049	89.720	160.079	267.822	270.953	317.309	444.509	601.655	604.627
0.14	10	UD	21.846	26.070	31.593	33.603	26.388	29.671	34.479	36.325	35.842	37.164	39.543	40.347
		FG-V	18.699	23.548	29.646	31.775	23.466	27.603	33.150	35.139	34.745	36.433	39.436	40.312
		FG-O	15.472	19.890	25.448	27.528	19.650	23.608	28.856	30.873	30.409	32.844	36.652	38.276
		FG-X	25.159	28.623	33.523	35.521	29.230	31.803	35.947	37.674	37.181	38.320	40.219	41.036
	20	UD	37.512	56.789	81.941	84.734	54.069	74.842	100.642	103.386	108.584	120.486	139.302	141.889
		FG-V	28.545	45.415	68.815	71.702	42.243	62.479	88.496	91.321	97.232	112.722	134.740	137.395
		FG-O	22.501	36.305	55.952	58.642	33.518	50.698	73.213	75.856	80.924	96.194	117.387	119.914
		FG-X	48.999	69.572	95.259	98.238	67.708	87.433	112.011	114.938	118.919	128.256	144.451	147.195
	50	UD	47.488	88.485	157.236	160.357	78.455	142.132	242.184	245.265	289.575	420.296	584.023	586.949
		FG-V	33.743	63.153	114.186	117.428	55.365	102.532	180.343	183.538	218.398	340.859	501.541	504.547
		FG-O	25.956	48.416	87.835	90.792	42.403	78.848	139.952	142.879	170.343	272.567	409.549	412.344
		FG-X	67.943	124.258	214.667	218.035	111.367	194.556	317.904	321.219	372.303	501.385	660.842	663.993
0.17	10	UD	30.209	37.135	45.913	49.049	37.364	42.956	50.740	53.663	52.993	55.318	59.451	60.828
		FG-V	25.455	33.072	42.590	45.915	32.696	39.551	48.432	51.576	51.095	54.147	59.363	60.920
		FG-O	21.064	28.010	36.742	39.918	27.441	33.996	42.388	45.469	44.940	48.845	55.024	57.587
		FG-X	35.244	41.059	48.900	52.107	41.779	46.211	52.994	55.944	55.061	57.192	60.727	62.128
	20	UD	48.342	75.525	112.196	116.474	71.174	102.395	141.691	145.893	154.607	175.059	205.692	209.669
		FG-V	36.464	59.327	92.272	96.723	54.752	83.787	122.210	126.564	136.044	162.214	197.756	201.853
		FG-O	28.736	47.359	74.983	79.048	43.399	67.976	101.337	105.329	113.698	139.290	173.233	177.039
		FG-X	63.936	93.980	132.285	136.953	90.512	121.246	159.236	163.824	170.596	186.796	213.528	217.868
	50	UD	58.605	109.705	197.229	201.993	97.071	178.459	310.143	314.853	375.469	567.911	814.027	818.507
		FG-V	41.720	77.884	141.687	146.660	68.337	127.487	227.400	232.308	278.371	450.784	684.441	689.072
		FG-O	32.145	59.713	108.870	113.316	52.366	97.954	176.176	180.577	216.788	360.265	559.932	564.145
		FG-X	84.030	155.192	272.407	277.681	138.544	247.022	413.253	418.454	490.451	687.617	931.608	936.553

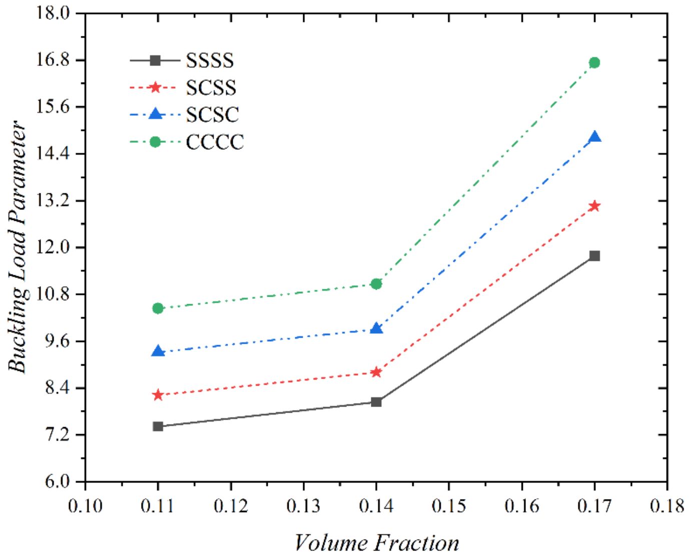

Fig. 4-11: Effect of volume fraction of CNT on the buckling load parameter under biaxial compressive load

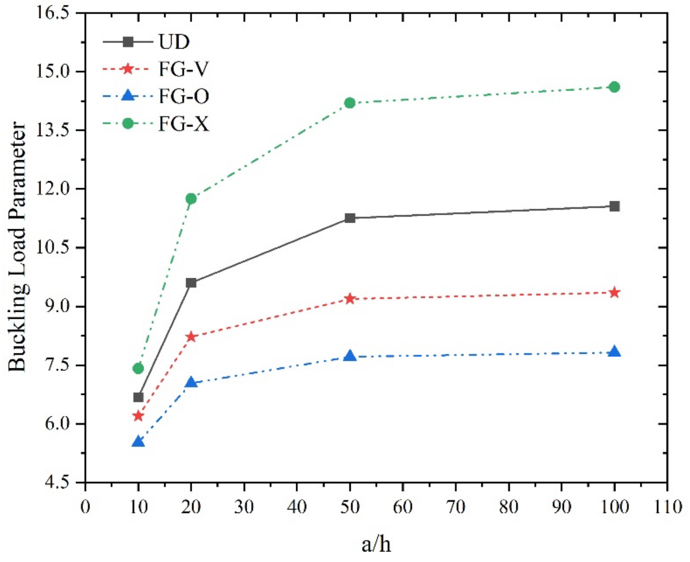

Fig. 4-12: Influence of span-thickness ratio on the buckling load parameter under biaxial compression load

4.5. Free Vibration of FG-CNTRC Plate

In this section, the free vibration response of the square temperature-dependent FG-CNT reinforced plate using analytical (Navier) and numerical (FEM) approach based on IHSDT is presented. The analytical solution is implemented for the square FG-CNT reinforced plate with SSSS constraints. This solution is unaffected by any computational error but only limited to simply supported boundary condition. To extend the studies for more boundary conditions, the FEM based numerical solution is obtained. To obtain the analytical and numerical solution a generalized MATLAB code is developed in order to compute the analytical and numerical solution. Further, a comparison is made with the existing results to ensure the accuracy of the presented methodology. The convergence of finite element solutions for the free vibration response is ensured. The new results are presented at 500 K and 700 K temperature conditions. The free vibration response is examined for different volume fraction of CNT, distribution of CNT, span-thickness ratio and boundary conditions.

4.5.1. Analytical solution

For the vibration behavior, a square plate with gradation of CNT along the thickness with SSSS boundary constraints is considered. In this section, the vibration response is predicted for different volume fraction of CNT, span-thickness ratio (*a/h*), and aspect ratio (*a/b*). The vibration response of FG-CNT reinforced plate is predicted by considering four different types of CNT gradation schemes. The vibration response is depicted in terms of a non-dimensional frequency parameter for CNTRC and the following non-dimensional form is considered.

$$\bar{\omega} = \omega\left(a^2/h\right)\sqrt{\rho^m/E^m} \tag{4.2}$$

The properties of PmPV matrix and CNT material are taken same as indicated in Section 4.3. The matrix properties are considered at $T = 300$ K. The results obtained for various distribution of CNT (UD, FG-V, FG-O and FG-X) and other parameters are listed in Table 4.16. The present results are also compared with the results reported in literature due to Zhu *et al.* [53] and Singh and Bhar [108]. It is noted that the results presented by Zhu *et al.* [53] are in the framework of FSDT and also simulated in ANSYS using SHELL element. The comparison of results reveals that there is a close agreement of the present results. However, the agreement of results increases with increase in *a/h* ratio. This is accounted towards the fact that the shear deformation effect is higher in the thick plates (low *a/h* ratio).

Table 4.16: Non dimensional natural frequency parameter of square FG-CNTRC plate with different volume fraction (V^*_{CNT}), *a/h* ratio and SSSS boundary constraints

V^*_{CNT}	*a/h*	Type of CNT distribution	Present	Zhu *et al.* [53]	Zhu *et al.* [53] ANSYS	Singh and Bhar [108]
0.11	10	UD	13.6824	13.532	13.521	13.735
		FG-V	12.5514	12.452	12.495	12.606
		FG-O	11.3109	11.550	11.600	11.675
		FG-X	14.9076	14.616	14.659	14.873
	20	UD	17.3608	17.355	17.328	17.458
		FG-V	15.1011	15.110	15.103	15.179
		FG-O	13.3865	13.523	13.531	13.582
		FG-X	20.0196	19.939	19.916	20.093
	50	UD	19.1637	19.223	19.184	19.238
		FG-V	16.2054	16.252	16.216	16.267
		FG-O	14.2436	14.302	14.290	14.326
		FG-X	22.9224	22.984	22.910	23.000
0.14	10	UD	14.5219	14.306	14.296	14.553
		FG-V	13.4020	13.256	13.300	13.451
		FG-O	12.1106	12.338	12.391	12.501
		FG-X	15.6537	15.368	15.413	15.669
	20	UD	18.9708	18.921	18.893	19.082
		FG-V	16.5309	16.510	16.503	16.625
		FG-O	14.6549	14.784	14.794	14.882
		FG-X	21.7226	21.643	21.620	21.867
	50	UD	21.3293	21.354	21.311	21.417
		FG-V	17.9755	17.995	17.956	18.048
		FG-O	15.7622	15.801	15.788	15.859
		FG-X	25.5226	25.555	25.474	25.631
0.17	10	UD	16.9910	16.815	16.801	16.832
		FG-V	15.5578	15.461	15.514	15.409
		FG-O	14.0826	14.282	14.345	14.198
		FG-X	18.4014	18.278	18.330	18.377
	20	UD	21.4563	21.456	21.422	21.102
		FG-V	18.6164	18.638	18.628	18.303
		FG-O	16.5085	16.628	16.640	16.326
		FG-X	24.7024	24.764	24.735	24.422
	50	UD	23.6178	23.697	23.649	23.077
		FG-V	19.9235	19.982	19.938	19.488
		FG-O	17.4857	17.544	17.529	17.136
		FG-X	28.2867	28.413	28.322	27.653

The present IHSDT has the capability to capture these deformation effects more precisely and hence large deviation from FSDT are observed for thick plates. Further, the effect of volume fraction indicates that there is an increment in non-dimensional natural frequency of the considered plates due to increase in volume fraction of CNT for a specific *a/h* ratio and CNT distribution. It is also noted that the non-dimensional natural frequency increase due to increase in *a/h* ratio for a particular CNT distribution and volume fraction. The effect of CNT distribution indicates that the plate with FG-X configuration possesses highest natural frequency followed by UD, FG-V and FG- O.

Further, the influence of CNT volume fraction on the non-dimensional natural frequency parameter is obtained and shown in Fig. 4.13. The study is conducted for all four considered CNT distributions with a variety of volume fraction (0.11, 0.12, 0.14, 0.17 and 0.28) at 300 K temperature. The thick plate (*a/h* = 10) as well as thin plate (*a/h* =100) is analyzed for the vibration behavior and the behavior is depicted in Fig. (4.13a) and Fig. (4.13b) respectively. It is clearly observed that, the increment of volume fraction in the CNT increases the value of the frequency parameter for all the four distributions. The plate with the FG-X configuration possesses higher frequency relative to UD while the plate with FG-O configuration possesses lower frequency relative to UD. For a particular volume fraction and CNT configuration, the thin plate (*a/h* =100) possesses higher non-dimensional natural frequency relative to thick plate (*a/h* = 10).

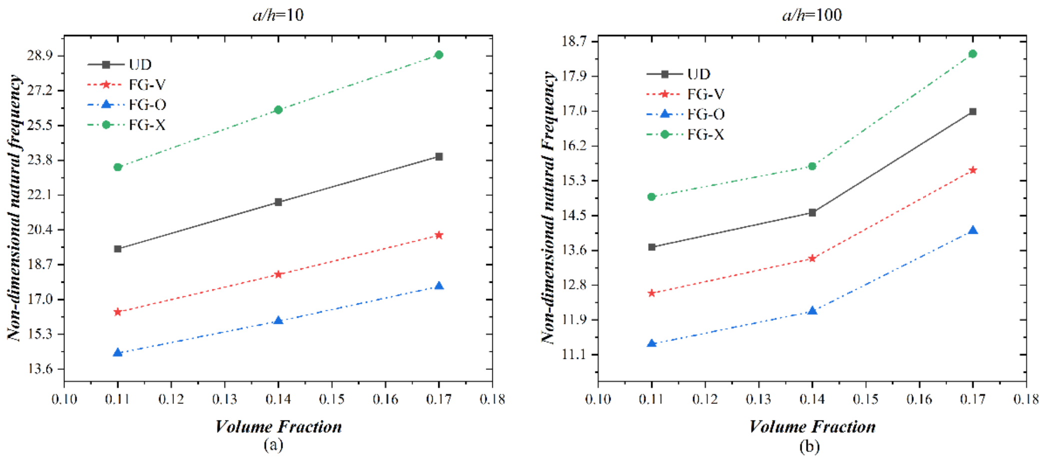

Fig. 4-13: Influence of volume fraction of CNT on the non-dimensional natural frequency of FG CNTRC plate (a) *a/h* = 10, and (b) *a/h* = 100

The vibration response is further carried out with the temperature dependent material properties. The non-dimensional natural frequency parameter of FG-CNTRC plate with the variation of volume fraction, span to thickness ratio and temperature are obtained and listed in Table 4.17. The numerical results from the table show the increment in the natural frequency due to rise in the temperature. The span to thickness ratio has significant influence on the natural frequency parameter indicating that the increment in the span to thickness ratio increases the natural frequency. It is also observed that the non-dimensional natural frequency for FG-X is the highest, while in case of FG-O, it is lowest. It is also noteworthy that the non-dimensional natural frequency decreases due to increase in the volume fraction.

Table 4.17: Non dimensional frequency parameter of square SSSS FG-CNTRC plate with different volume fraction (V^*_{CNT}), *a/h* ratio and temperature dependent properties at 500 K and 700 K

V^*_{CNT}	Type of CNT distribution	*a/h* = 10		*a/h* = 50		*a/h* = 100	
		T = 500 K	*T* = 700 K	*T* = 500 K	*T* = 700 K	*T* = 500 K	*T* = 700 K
0.11	UD	15.2645	19.201	24.6299	48.3545	25.3206	54.4956
	FG-V	14.2505	18.7362	20.6937	41.6336	21.0901	45.339
	FG-O	12.8294	16.3948	18.1161	36.542	18.4203	39.4688
	FG-X	16.3418	20.0656	29.4382	55.6105	30.6233	65.2798
0.14	UD	16.0668	20.1316	27.4242	52.8352	28.3595	60.7984
	FG-V	15.1077	19.7138	23.0304	45.8359	23.5657	50.7138
	FG-O	13.657	17.2206	20.1466	40.3832	20.5503	44.1939
	FG-X	17.0164	20.938	32.6959	60.0574	34.3176	72.4682
0.17	UD	18.9973	23.9359	30.404	59.9328	31.2322	67.3755
	FG-V	17.7188	23.3675	25.5031	51.5545	25.9742	56.0221
	FG-O	16.0845	20.7848	22.3178	45.4116	22.6646	48.8103
	FG-X	20.1623	24.7414	36.3362	68.5931	37.8052	80.5921

In order to investigate the response of rectangular plates, the influence of aspect ratio (*a/h* =1.2, 1.5 and 2) and span-thickness ratio on the non-dimensional natural frequency parameter of FG-CNTRC plate with SSSS constraints at different temperature (300 K, 500 K and 700 K) is examined. The CNT volume fraction is chosen as 0.11. The obtained results are listed in Table 4.18. It is observed that the non-dimensional natural frequency decreases due to increment in the aspect ratio. The influence of aspect ratio and span-thickness ratio on natural frequency parameter is more in case FG-X configuration as compared to other configurations.

Table 4.18: Non dimensional natural frequency parameter of rectangular FG-CNTRC plate (V^*_{CNT}) for different aspect ratio (*a*/*b*), *a*/*h* ratio with SSSS boundary constraints (TD properties at 300 K, 500 K and 700 K)

a/b	*a/h*	Type of CNT distribution	*T* = 300 K	*T* = 500 K	*T* = 700 K
0.5	10	UD	8.5301	9.1892	12.4352
		FG-V	8.1785	8.9248	12.2977
		FG-O	7.3254	7.8836	9.8027
		FG-X	8.9633	9.6063	12.5846
	20	UD	13.1924	14.8796	18.975
		FG-V	11.9552	13.7897	18.4883
		FG-O	10.6461	12.3075	16.0915
		FG-X	14.4789	15.9978	19.8517
	100	UD	18.6223	24.2205	48.1793
		FG-V	15.5389	20.1848	41.4129
		FG-O	13.5268	17.5663	36.2992
		FG-X	22.4532	29.0858	55.4614
1	10	UD	13.6824	15.2645	19.201
		FG-V	12.5514	14.2505	18.7362
		FG-O	11.3109	12.8294	16.3948
		FG-X	14.9076	16.3418	20.0656
	20	UD	17.3608	21.0445	31.2452
		FG-V	15.1011	18.4664	29.2349
		FG-O	13.3865	16.3601	26.0777
		FG-X	20.0196	23.8733	33.3347
	100	UD	19.4742	25.3206	54.4956
		FG-V	16.3863	21.0901	45.339
		FG-O	14.3815	18.4203	39.4688
		FG-X	23.4573	30.6233	65.2798
1.2	10	UD	15.2627	17.2669	22.064
		FG-V	13.8943	15.9394	21.3881
		FG-O	12.5486	14.3717	18.9664
		FG-X	16.8073	18.6852	23.078
	20	UD	18.368	22.4705	35.1919
		FG-V	15.9792	19.5771	32.4332
		FG-O	14.2175	17.3576	28.9203
		FG-X	21.3019	25.7775	37.9833
	100	UD	19.9301	25.7199	55.4145
		FG-V	16.9216	21.5338	45.9614
		FG-O	14.9419	18.8796	40.0058
		FG-X	23.8864	31.0368	66.7146
1.5	10	UD	17.4684	19.9882	26.3363
		FG-V	15.8854	18.2804	25.2759
		FG-O	14.4425	16.5449	22.6675
		FG-X	19.4013	21.9	27.6638
	20	UD	19.8599	24.2793	40.1535
		FG-V	17.4505	21.1468	36.3238
		FG-O	15.6741	18.8443	32.3449
		FG-X	23.0137	28.0689	44.0595
	100	UD	20.9167	26.5291	56.4157
		FG-V	18.0885	22.481	46.7576

		FG-O	16.1612	19.8709	40.7478
		FG-X	24.7866	31.8026	68.1462
2	10	UD	21.4523	24.41	33.3258
		FG-V	19.834	22.3829	31.536
		FG-O	18.3308	20.4976	28.5605
		FG-X	23.7656	26.9627	35.3522
	20	UD	23.0507	27.4423	46.6374
		FG-V	20.8863	24.3343	41.4136
		FG-O	19.1516	22.026	36.8939
		FG-X	26.262	31.5874	52.2568
	100	UD	23.6764	28.7808	57.9991
		FG-V	21.2767	25.1261	48.3491
		FG-O	19.4499	22.6283	42.3595
		FG-X	27.3132	33.8583	69.9933

4.5.2. Finite element solution

This subsection presents the detailed numerical results on the basis of developed formulation for free vibration characteristics of FG-CNTRC plates in the FE framework of IHSDT. The convergence and validation studies are first carried out to ascertain the accuracy and consistency of computer code that has been developed in MATLAB on the basis of the developed FE framework. Further, detailed numerical investigations are conducted to examine the effect of various parameters including the CNT volume fraction, span to thickness ratio, CNT distribution and the boundary constraints on the free vibration response of temperature dependent FG-CNTRC plates. The properties of PmPV matrix and CNT material are taken same as indicated in Section 4.3.

4.5.2.1. Convergence Study

For the purpose of ensuring the convergence behavior of the FE solution, an FG-CNTRC plate with $a/h=10$, volume fraction ($V_{CNT}=0.11$) and uniform distribution of CNT is considered. The material properties are assumed at 300 K temperature condition. The free vibration response is studied in the form of a fundamental frequency parameter, $\bar{\omega} = \omega\left(\rho_m/E_m\right)^{1/2}\left(a^2/h\right)$ for the plate, and the mesh distributions are considered from (2 × 2) to (10 × 10) to study the convergence of the solution.

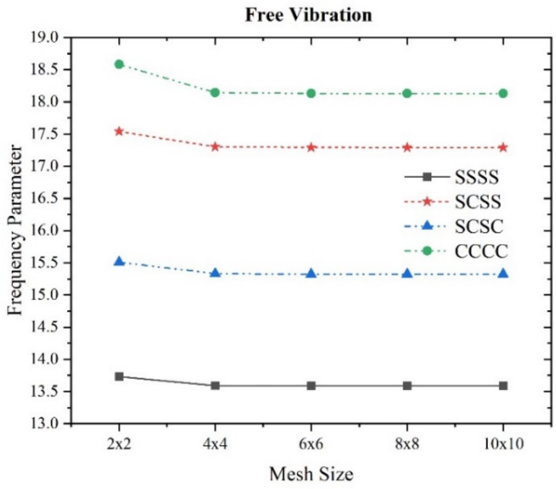

Fig. 4-14: Convergence study for fundamental frequency parameter of FG-CNTRC plate with different boundary constraints

The obtained non-dimensional results are plotted in Fig. 4.14 for various mesh sizes and different boundary conditions. It is depicted from Fig. 4.14 that frequency parameters converge excellently between (8 × 8) and (10 × 10) for different boundary conditions. On account of the above, a mesh size of (10 × 10) is used for the further investigation.

4.5.2.2. Validation

The accuracy of the developed FEM is illustrated by presenting a comparison study for the fundamental frequency parameter of the FG-CNTRC plate with all edges simply supported. The analysis is carried out for various volume fractions of CNT (0.11, 0.14, and 0.17), different span to thickness ratios (*a/h* = 10, 20 and 50) and four types of CNT distribution (UD, FG-V, FG-O, and FG-X). The material parameters of the matrix and the CNT are considered at 300K temperature. The non-dimensional results $\bar{\omega} = \omega\left(\rho_m / E_m\right)^{1/2}\left(a^2/h\right)$ are obtained and compared with the FSDT based FEM and ANSYS solutions presented by Zhu *et al.* [53], HSDT based isogeometric FE solution presented by Singh and Bhar [108], and Navier solution of inverse trigonometric SDT by Singh and Sahoo [48] in Table 4.19. The results are also compared with the analytical results and it is noted that the average percentage difference due to FE solution is 0.27%. Moreover, it is noted that the percentage difference of the presented results from FSDT results is 0.4 %, from ANSYS results is 0.49 % and from HSDT results is 1.07 %. It is concluded that results obtained using IHSDT in FE framework are in accordance with the existing literature developed in the framework of FSDT based FEM solution, isogeometric solution and Navier solution. It is also noted that the fundamental frequency increases due to increment in *a/h* ratio and volume fraction of CNT. Moreover, the plate with FG-O distribution of CNT possesses the least non-dimensional natural frequency and the plate with FG-X distribution possesses the highest natural frequency for a specific *a/h* ratio and CNT volume fraction.

In order to ensure the applicability to predict higher modes of vibration, first six frequency parameters of the FG-CNTRC plate with SSSS and CCCC boundary constraints are presented in Tables 4.20 and 4.21, respectively. The obtained natural frequencies relative to first six modes are compared with the existing results. The comparison study is based on volume fraction, plate span to thickness ratio and distribution of CNT in FG-CNTRC plate and with the results reported in the literature by Zhu *et al.* [53] in the framework of FSDT. It is noted that the presented results agree well with the existing results.

Table 4.19: Non dimensional fundamental frequency parameter of square FG-CNTRC plate for different volume fraction (V_{CNT}^*), *a/h* ratio with SSSS boundary condition

V_{CNT}^*	*a/h*	Type of CNT distribution	Present	IHSDT (CFS)	Singh and Sahoo [48]	Zhu *et al.* [53]		Singh and Bhar [108]
						FEM	ANSYS	
0.11	10	UD	13.5879	13.6824	13.6875	13.532	13.521	13.735
		FG-V	12.4830	12.5514	12.465	12.452	12.495	12.606
		FG-O	11.3112	11.3109	11.562	11.550	11.600	11.675
		FG-X	14.7313	14.9076	14.624	14.616	14.659	14.873
	20	UD	17.3266	17.3608	17.3698	17.355	17.328	17.458
		FG-V	15.0803	15.1011	15.103	15.110	15.103	15.179
		FG-O	13.3865	13.3865	13.541	13.523	13.531	13.582
		FG-X	19.9393	20.0196	19.939	19.939	19.916	20.093
	50	UD	19.1574	19.1637	19.200	19.223	19.184	19.238
		FG-V	16.2020	16.2054	16.269	16.252	16.216	16.267
		FG-O	14.2438	14.2436	14.316	14.302	14.290	14.326
		FG-X	22.9052	22.9224	22.910	22.984	22.910	23.000
0.14	10	UD	14.4003	14.5219	14.515	14.306	14.296	14.553
		FG-V	13.3138	13.4020	13.324	13.256	13.300	13.451
		FG-O	12.1107	12.1106	12.341	12.338	12.391	12.501
		FG-X	15.4579	15.6537	15.413	15.368	15.413	15.669
	20	UD	18.9256	18.9708	18.980	18.921	18.893	19.082
		FG-V	16.5038	16.5309	16.631	16.510	16.503	16.625
		FG-O	14.6553	14.6549	14.792	14.784	14.794	14.882
		FG-X	21.6323	21.7226	21.657	21.643	21.620	21.867
	50	UD	21.3207	21.3293	21.300	21.354	21.311	21.417
		FG-V	17.9710	17.9755	18.001	17.995	17.956	18.048
		FG-O	15.7624	15.7622	15.852	15.801	15.788	15.859
		FG-X	25.5024	25.5226	25.555	25.555	25.474	25.631
0.17	10	UD	16.8772	16.9910	16.9994	16.815	16.801	16.832
		FG-V	15.4805	15.5578	15.472	15.461	15.514	15.409
		FG-O	14.0826	14.0826	14.293	14.282	14.345	14.198
		FG-X	18.2359	18.4014	18.361	18.278	18.330	18.377
	20	UD	21.4154	21.4563	21.4673	21.456	21.422	21.102
		FG-V	18.5933	18.6164	18.824	18.638	18.628	18.303
		FG-O	16.5091	16.5085	16.649	16.628	16.640	16.326
		FG-X	24.6311	24.7024	24.782	24.764	24.735	24.422
	50	UD	23.6104	23.6178	23.6000	23.697	23.649	23.077
		FG-V	19.9198	19.9235	20.024	19.982	19.938	19.488
		FG-O	17.4861	17.4857	17.626	17.544	17.529	17.136
		FG-X	28.2719	28.2867	28.531	28.413	28.322	27.653

Table 4.20: Non dimensional frequency parameter (for first six modes) of square FG-CNTRC plate for different volume fraction (V^*_{CNT}), *a/h* ratio with SSSS boundary constraints

V^*_{CNT}	*a/h*	Mode	UD		FG-V		FG-O		FG-X	
			Present	Zhu *et al.* [53]	Present	Zhu *et al.* [53]	Present	Zhu *et al.* [53]	Present	Zhu *et al.* [53]
0.11	10	1	13.588	13.532	12.483	12.452	11.311	11.550	14.731	14.616
		2	17.693	17.700	17.037	17.060	16.083	16.265	18.655	18.646
		3	19.428	19.449	19.477	19.499	19.478	19.499	19.478	19.499
		4	19.428	19.449	19.477	19.499	19.478	19.499	19.478	19.499
		5	27.221	27.569	26.985	27.340	26.139	26.513	28.094	28.519
		6	33.158	32.563	31.886	31.417	29.272	30.280	34.416	33.598
	20	1	17.327	17.355	15.080	15.110	13.387	13.523	19.939	19.939
		2	21.421	21.511	19.815	19.903	18.331	18.486	23.694	23.776
		3	31.882	32.399	31.045	31.561	29.644	30.166	33.837	34.389
		4	38.855	38.898	38.955	38.998	38.955	38.998	38.955	38.998
		5	38.855	38.898	38.955	38.998	38.955	38.998	38.955	38.998
		6	48.535	50.199	47.558	47.739	42.595	43.948	50.478	52.268
	50	1	19.157	19.223	16.202	16.252	14.244	14.302	22.905	22.984
		2	23.273	23.408	21.028	21.142	19.264	19.373	26.623	26.784
		3	34.068	34.669	32.764	33.350	31.056	31.615	36.949	37.591
		4	52.091	54.043	51.492	53.430	49.511	51.370	54.904	56.946
		5	70.078	70.811	59.533	60.188	52.124	53.035	79.986	83.150
		6	72.180	72.900	62.133	62.780	54.945	55.823	82.434	84.896
0.14	10	1	14.400	14.306	13.314	13.256	12.111	12.338	15.458	15.368
		2	18.391	18.362	17.736	17.734	16.685	16.848	19.369	19.385
		3	19.775	19.791	19.862	19.879	19.863	19.879	19.863	19.879
		4	19.775	19.791	19.862	19.879	19.863	19.879	19.863	19.879
		5	27.908	28.230	27.684	28.021	26.664	27.003	28.930	29.398
		6	34.418	33.646	33.300	32.678	30.816	31.633	35.459	34.631
	20	1	18.926	18.921	16.504	16.510	14.655	14.784	21.632	21.642
		2	22.811	22.867	21.024	21.087	19.322	19.449	25.268	25.360
		3	33.084	33.570	32.125	32.617	30.410	30.906	35.369	35.938
		4	39.549	39.583	39.726	39.759	39.726	39.759	39.726	39.759
		5	39.549	39.583	39.726	39.759	39.726	39.759	39.726	39.759
		6	49.773	51.422	49.424	51.078	46.018	47.341	52.215	54.062
	50	1	21.321	21.354	17.971	17.995	15.762	15.801	25.502	25.555
		2	25.192	25.295	22.556	22.643	20.477	20.563	29.053	29.192
		3	35.697	36.267	34.102	34.660	31.979	32.509	39.205	39.833
		4	53.670	55.608	52.907	54.833	50.351	52.184	57.274	59.333
		5	77.465	78.110	65.949	66.552	57.837	58.748	82.810	87.814
		6	78.599	80.015	68.352	68.940	60.407	61.277	90.546	91.299

Table 4.21: Non dimensional frequency parameter (for six modes) of square FG-CNTRC plate for different volume fraction (V^*_{CNT}), *a/h* ratio with CCCC boundary constraints

V^*_{CNT}	*a/h*	Mode	UD		FG-V		FG-O		FG-X	
			Present	Zhu *et al.* [53]	Present	Zhu *et al.* [53]	Present	Zhu *et al.* [53]	Present	Zhu *et al.* [53]
0.11	10	1	18.128	17.625	17.646	17.211	16.459	16.707	18.686	18.083
		2	23.327	23.041	23.054	22.818	22.054	22.253	23.911	23.606
		3	33.366	33.592	33.297	33.070	32.173	32.378	33.998	34.338
		4	35.081	33.729	34.323	33.552	32.440	32.857	35.986	34.467
		5	37.275	37.011	37.403	36.528	35.755	35.809	37.414	37.447
		6	38.243	37.317	37.672	37.437	37.414	37.447	39.120	37.786
	20	1	28.648	28.400	26.447	26.304	23.934	24.486	30.858	30.421
		2	33.222	33.114	31.503	31.496	29.246	29.795	35.294	35.036
		3	43.983	44.559	42.920	43.589	40.883	41.895	45.958	46.480
		4	60.078	59.198	56.853	56.249	51.930	53.557	62.955	61.980
		5	60.927	61.851	59.850	59.221	55.191	56.617	63.292	64.562
		6	62.756	63.043	60.416	62.608	58.411	60.719	65.860	65.174
	50	1	39.539	39.730	33.974	34.165	29.908	30.303	46.049	46.166
		2	43.583	43.876	38.737	39.043	34.964	35.444	49.716	49.934
		3	53.808	54.768	50.191	51.204	46.741	47.878	59.337	60.225
		4	71.654	74.488	69.277	72.202	65.885	68.842	76.725	79.534
		5	97.097	98.291	85.185	86.291	75.268	77.468	102.108	108.694
		6	97.287	100.537	88.002	89.054	78.349	80.460	110.329	110.921
0.14	10	1	18.721	18.127	18.310	17.791	17.179	17.311	19.214	18.593
		2	23.931	23.572	23.715	23.413	22.681	22.782	24.546	24.243
		3	34.074	34.252	34.060	34.101	33.084	33.411	34.837	35.224
		4	36.183	34.650	35.529	34.275	33.539	33.441	36.989	35.411
		5	37.939	37.921	38.135	37.538	37.011	36.788	38.146	38.169
		6	39.322	37.972	38.844	38.159	38.146	38.169	40.168	38.789
	20	1	30.276	29.911	28.158	27.926	25.631	26.127	32.285	31.857
		2	34.737	34.516	33.070	32.976	30.695	31.186	36.739	36.487
		3	45.418	45.898	44.393	44.989	42.089	43.034	47.542	48.087
		4	62.440	61.628	59.816	58.951	55.066	56.403	64.846	64.334
		5	62.809	64.199	61.981	61.816	58.139	59.155	65.658	66.912
		6	65.405	64.496	62.707	64.135	59.557	61.793	68.226	67.148
	50	1	43.473	43.583	37.431	37.568	32.990	33.369	50.299	50.403
		2	47.275	47.479	41.929	42.175	37.690	38.145	53.828	54.025
		3	57.107	57.968	53.019	53.963	48.964	50.055	63.258	64.112
		4	74.654	77.395	71.917	74.785	67.747	70.646	80.599	83.394
		5	100.056	106.371	93.055	94.022	82.593	84.799	106.235	112.896
		6	105.618	106.487	95.677	96.573	85.411	87.511	118.507	119.134

4.5.2.3. Parametric studies

In this subsection, the influence of temperature-dependent material properties on the free vibration response of the FG-CNTRC plate is investigated along with the effect of other parameters such as boundary constraints, span-thickness ratio, and volume fraction and gradation pattern of CNT. The effect of span to thickness ratio (10, 20, and 50) and volume fraction (0.11, 0.14, and 0.17), distribution of CNT (UD, FG-V, FG-O and FG-X) are taken into consideration. The analysis is carried out for boundary constraints identified as SSSS, SCSS, SCSC, and CCCC considering temperature dependent properties at 300 K, 500 K, and 700 K. The results are obtained in the form of non-dimensional frequency parameter and the same are listed in Table 4.22. It is concluded from Table 4.22 that with an increase in temperature from 300 K to 500 K, the fundamental frequency increase by 11% as compared to material properties considered at 300 K ($V_{CNT}^{*}=0.11$, UD-CNT and SSSS boundary condition). However, the fundamental frequency increase by 32 % when increasing temperature condition from 300 K to 700 K ($V_{CNT}^{*}=0.11$, UD-CNT with SSSS boundary constraints). Thus, it is concluded that TD material properties have a substantial influence on the fundamental frequency of the FG-CNT reinforced plate. Further, it is noted that the frequency parameter increases due to increment in the volume fraction of CNT from 0.11 to 0.17. This is accounted towards the substantial increment in the stiffness of the FG-CNTRC plate due to higher volume fraction. Moreover, the FG-CNTRC plate with FG-X distribution has maximum fundamental frequency relative to the other sets of distributions of CNT. That is because the distribution of CNTs along the top and bottom surfaces enhances the stiffness of the FG-CNT reinforced plate relatively higher. The influence of the boundary constraints reveals that the FG-CNT reinforced plate with all edges clamped (CCCC) possess higher frequency as compared to the other three boundary constraints. The non-dimensional frequency parameter increases due to increment in the span-thickness ratio for a specific volume fraction and distribution pattern of CNT and specific boundary constraint.

Table 4.22: Non dimensional fundamental frequency parameter of square FG-CNTRC plate for different volume fraction (V_{CNT}^*), *a/h* ratio, and different boundary constraints with TD properties

V_{CNT}^*	*a/h*	CNT distribution	300 K				500 K				700 K			
			SSSS	SCSS	SCSC	CCCC	SSSS	SCSS	SCSC	CCCC	SSSS	SCSS	SCSC	CCCC
0.11	10	UD	13.588	17.290	15.323	18.128	15.083	18.002	16.342	18.807	17.911	19.163	18.341	19.918
		FG-V	12.483	16.771	14.569	17.646	14.109	17.659	15.745	18.487	17.553	19.111	18.105	19.872
		FG-O	11.311	15.557	13.387	16.459	12.829	16.504	14.551	17.351	16.268	18.431	17.152	19.184
		FG-X	14.731	17.832	16.102	18.686	16.032	18.399	16.976	19.226	18.320	19.326	18.659	20.113
	20	UD	17.327	28.039	22.658	28.648	20.974	30.983	25.972	31.528	30.748	36.142	32.977	36.599
		FG-V	15.080	25.767	20.313	26.447	18.422	29.106	23.753	29.698	28.838	35.544	31.830	36.014
		FG-O	13.387	23.219	18.158	23.934	16.360	26.450	21.366	27.069	26.077	33.220	29.344	33.697
		FG-X	19.939	30.264	25.110	30.858	23.719	32.742	28.148	33.285	32.514	36.832	34.159	37.308
	50	UD	19.157	39.054	28.325	39.539	24.615	48.354	35.822	48.740	48.216	74.664	61.489	74.901
		FG-V	16.202	33.387	24.011	33.974	20.686	41.814	30.483	42.276	41.549	69.278	55.375	69.540
		FG-O	14.244	29.287	21.045	29.908	18.116	36.811	26.731	37.300	36.539	62.488	49.396	62.763
		FG-X	22.905	45.611	33.536	46.049	29.399	55.427	41.927	55.781	55.292	79.582	67.375	79.816
0.14	10	UD	14.400	17.882	15.990	18.721	15.832	18.536	16.959	19.345	18.457	19.583	18.834	20.348
		FG-V	13.314	17.437	15.289	18.310	14.924	18.263	16.421	19.094	18.171	19.580	18.654	20.351
		FG-O	12.111	16.299	14.139	17.179	13.655	17.208	15.287	18.038	16.998	19.009	17.808	19.756
		FG-X	15.458	18.339	16.688	19.214	16.665	18.872	17.522	19.722	18.798	19.752	19.123	20.564
	20	UD	18.926	29.683	24.303	30.276	22.725	32.451	27.549	32.988	32.215	37.174	34.193	37.635
		FG-V	16.504	27.501	21.934	28.158	20.081	30.739	25.407	31.318	30.482	36.719	33.177	37.190
		FG-O	14.655	24.956	19.698	25.631	17.889	28.172	23.011	28.762	27.808	34.642	30.862	35.108
		FG-X	21.632	31.687	26.650	32.285	25.433	33.962	29.543	34.515	33.714	37.752	35.223	38.243
	50	UD	21.321	43.020	31.400	43.473	27.405	52.790	39.507	53.154	52.653	78.565	65.618	78.796
		FG-V	17.971	36.882	26.621	37.431	23.020	45.947	33.741	46.381	45.724	73.617	59.689	73.870
		FG-O	15.762	32.420	23.337	32.990	20.147	40.611	29.647	41.061	40.382	67.007	53.647	67.267
		FG-X	25.502	49.877	37.028	50.299	32.651	59.878	45.897	60.223	59.703	82.823	71.045	83.060
0.17	10	UD	16.877	21.570	19.086	22.622	18.777	22.483	20.384	23.491	22.371	23.964	22.920	24.909
		FG-V	15.480	20.935	18.141	22.042	17.556	22.093	19.657	23.138	21.966	23.985	22.690	24.941
		FG-O	14.083	19.597	16.791	20.693	16.082	20.848	18.334	21.874	20.598	23.256	21.665	24.168
		FG-X	18.236	22.168	19.982	23.282	19.860	22.921	21.099	23.999	22.804	24.218	23.311	25.239
	20	UD	21.415	34.836	28.088	35.604	25.989	38.589	32.284	39.274	38.319	45.155	41.156	45.728
		FG-V	18.593	31.945	25.116	32.812	22.788	36.232	29.490	36.982	35.941	44.510	39.784	45.101
		FG-O	16.509	28.970	22.535	29.842	20.291	33.225	26.700	33.973	32.856	42.059	37.097	42.631
		FG-X	24.631	37.444	31.041	38.230	29.311	40.572	34.837	41.290	40.252	45.901	42.450	46.528
	50	UD	23.610	48.209	34.930	48.823	30.387	59.853	44.278	60.342	59.766	92.993	76.442	93.290
		FG-V	19.920	41.072	29.518	41.823	25.494	51.644	37.601	52.234	51.458	86.275	68.800	86.606
		FG-O	17.486	36.074	25.874	36.840	22.318	45.596	33.017	46.196	45.412	78.562	61.806	78.894
		FG-X	28.272	56.265	41.371	56.847	36.302	68.449	51.766	68.920	68.308	98.559	83.344	98.870

Further, investigations are carried out to predict the higher modes of vibration for which SSSS and CCCC boundary conditions are considered for various *a/h* =10, 20 and 50 to ensure the applicability of the present formulation to predict higher modes of vibration for thick and thin FG-CNT reinforced plates. The first six frequency parameters of the FG-CNTRC plate with material properties considered at 500 K and 700 K temperatures are presented in Tables 4.23 and 4.24, respectively. The natural frequency parameters are presented for the plates with $V_{CNT}^{*} = 0.17$, and considered distribution patterns of CNT (UD, FG-V, FG-O and FG-X). It has been depicted from tables that frequency parameters evaluated at 700 K are higher than the corresponding frequency parameters at 500 K temperature. The first six mode shapes of vibration are also drawn for a specific case of FG-X distribution pattern of CNT. A thin FGCNTR plate (*a/h* = 20) with all its edges simply supported and clamped is considered and material properties corresponding to 700 K temperature are assumed for the analysis. These mode shapes are depicted in Fig. 4.15. This difference in eigenvalues can be attributed to the mechanical property variation between the longitudinal and transverse directions.

Table 4.23: Non dimensional frequency parameter (six modes) of square FG-CNTRC plate for different *a/h* ratio with SSSS and CCCC boundary constraints (TD properties at 500 K, $V_{CNT}^{*} = 0.17$)

a/h	Mode	SSSS				CCCC			
		UD	FG-V	FG-O	FG-X	UD	FG-V	FG-O	FG-X
10	1	15.083	14.109	12.829	16.032	18.807	18.487	17.351	19.226
	2	18.722	18.094	17.028	19.478	23.807	23.627	22.639	24.299
	3	19.428	19.477	19.478	19.478	33.660	33.626	32.759	34.243
	4	19.428	19.477	19.478	19.574	36.298	35.748	33.773	37.010
	5	27.779	27.517	26.592	28.608	37.273	37.390	37.057	37.398
	6	34.852	33.980	31.389	35.777	39.267	38.850	37.398	39.990
20	1	20.974	18.422	16.360	23.719	31.528	29.698	27.069	33.285
	2	24.345	22.341	20.498	26.822	35.628	34.139	31.725	37.347
	3	33.779	32.575	30.906	35.947	45.707	44.729	42.531	47.456
	4	38.856	38.955	38.956	38.956	62.073	61.559	56.893	63.968
	5	38.856	38.955	38.956	38.956	64.361	61.824	59.420	66.956
	6	49.682	49.098	47.362	51.784	66.723	64.411	59.694	69.268
50	1	24.615	20.686	18.116	29.399	48.740	42.276	37.300	55.781
	2	27.904	24.613	22.246	32.337	51.989	46.104	41.384	58.752
	3	37.337	35.117	32.931	41.198	60.698	55.944	51.602	66.960
	4	54.234	52.947	50.630	57.786	76.831	73.402	69.277	82.615
	5	78.226	75.213	66.032	81.930	100.844	98.579	91.597	106.455
	6	87.707	77.180	68.186	97.389	115.286	102.960	93.993	127.641

Table 4.24: Non dimensional frequency parameter (six modes) of square FG-CNTRC plate for *a/h* ratio with SSSS and CCCC boundary constraints (TD properties at 700 K and $V^*_{CNT} = 0.17$)

a/h	Mode	SSSS				CCCC			
		UD	FG-V	FG-O	FG-X	UD	FG-V	FG-O	FG-X
10	1	17.911	17.553	16.268	18.320	19.918	19.872	19.184	20.113
	2	19.428	19.478	19.438	19.478	24.630	24.623	23.932	24.966
	3	19.428	19.478	19.478	19.478	34.191	34.233	33.532	34.684
	4	20.837	20.585	19.478	21.312	37.270	37.371	37.151	37.374
	5	29.038	28.930	27.902	29.667	38.360	38.244	37.374	38.687
	6	37.256	37.352	35.891	37.361	41.040	40.965	39.900	41.449
20	1	30.748	28.838	26.077	32.514	36.599	36.014	33.697	37.308
	2	32.854	31.161	28.558	34.580	40.037	39.544	37.310	40.864
	3	38.856	38.735	36.372	38.956	49.046	48.716	46.564	50.144
	4	38.856	38.956	38.956	38.956	64.405	64.252	62.088	65.866
	5	39.984	38.956	38.956	41.718	72.671	71.678	67.793	73.936
	6	53.750	52.979	50.727	55.630	74.539	73.624	69.827	74.749
50	1	48.216	41.549	36.539	55.292	74.901	69.540	62.763	79.816
	2	49.848	43.512	38.647	56.762	76.859	71.709	65.064	81.739
	3	55.485	50.008	45.471	62.011	82.703	78.055	71.680	87.548
	4	67.784	63.563	59.338	73.804	94.810	90.950	84.895	99.686
	5	87.928	84.932	80.738	93.634	114.733	111.777	105.896	119.806
	6	97.141	97.390	97.390	97.390	143.111	141.004	135.020	148.617

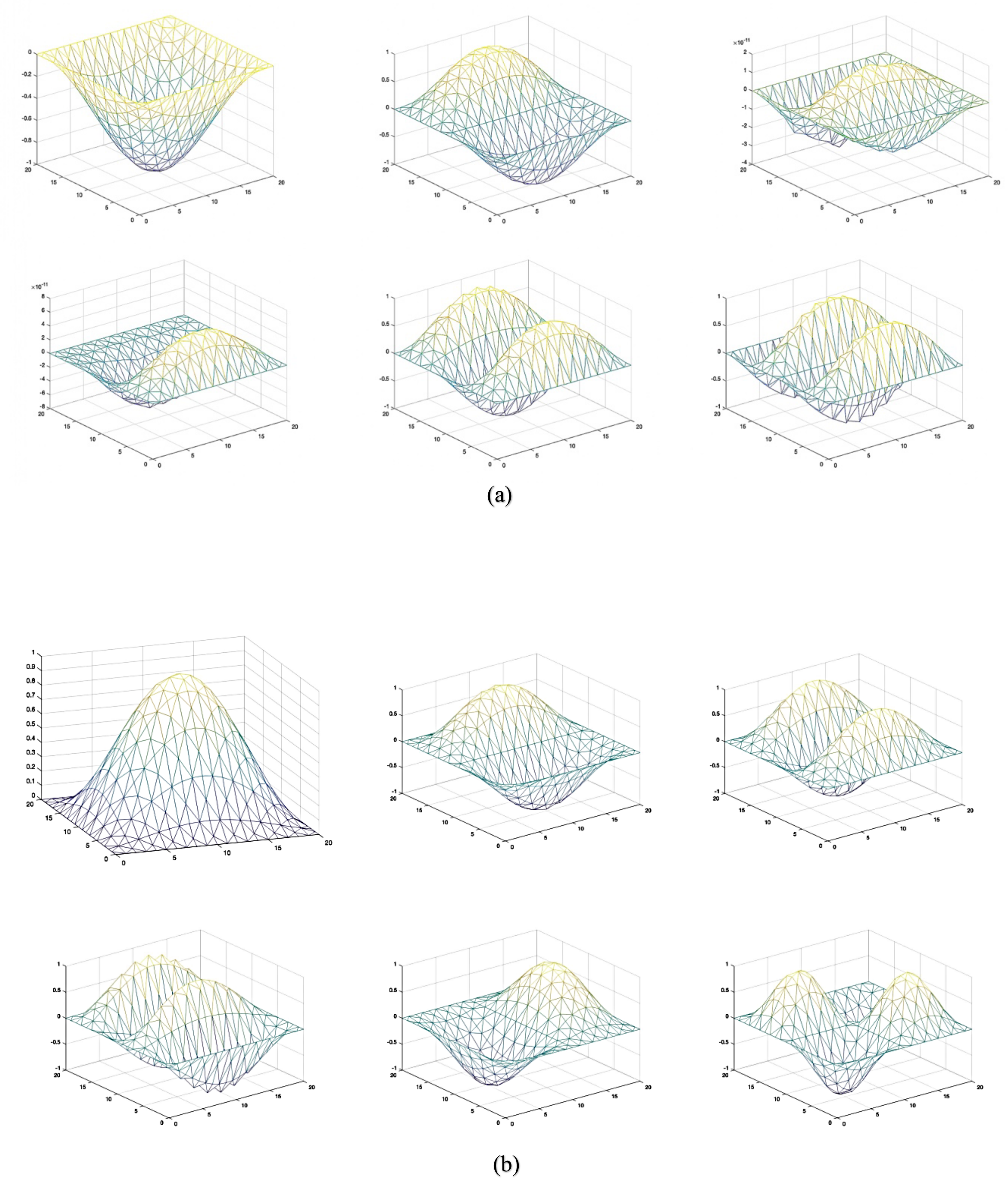

(a)

(b)

Fig. 4-15: First six mode shapes of FG-X distributed FG-CNTRC plate with all its edges simply supported (SSSS) and clamped (CCCC) at 700 K temperature

4.6. Hygro-Thermo-Mechanical Behavior of FG-CNTRC Plate

In this section, numerous examples are considered to study the response of FG-CNTRC plates under the action of different mechanical, thermal and moisture environment. A closed form solution is proposed for different loading conditions using a Navier type solution for simply supported FG-CNTRC plates. Further, the FEM is implemented to extend the solution technique for general boundary conditions. Moreover, in the parametric study, the effect of volume fraction of CNT, plate span to thickness ratio, distribution of CNT and boundary constraints on the FG-CNTRC plates are studied. The PMMA (Poly [methyl methacrylate]) is considered as the matrix to examine the hygro-thermo-mechanical condition. The properties of the CNT are same as indicated in section 4.3. The material properties of PMMA are as follows [80]:

$E_m = 2.5$ GPa, $\rho^m = 1150$ Kg/m^3, $\beta^m = 0.33$, $\nu^m = 0.34$.

4.6.1. Convergence study

In order to study the convergence of presented FEM, a FG-CNTRC plate with $a/h = 10$, $V_{CNT} = 0.11$, and UD, FG-V, FG-O and FG-X distribution of CNT is considered. The plate is exposed to uniform thermal loading ($T_2 = 100$, $T_1 = T_3 = 0$) alone. The results are obtained in the form of transverse deflection for a variety of mesh ranging from elements to 144 elements. The Fig. 4.16 indicates the convergence of mesh for two different boundary constraints (SSSS and SCSC). It is depicted that a good convergence behavior is achieved at the mesh size (10 × 10). It is observed that the plate with boundary condition SSSS is more affected by the thermal loading w.r.t the SCSC boundary condition. It is concluded that the deformation in the FG-X distribution is least due to the thermal loading condition for both the boundary conditions.

Further, in another convergence study for thin FG-CNTRC, a plate with span to thickness ratio ($a/h = 100$), volume fraction ($V_{CNT} = 0.11$) and two different distributions of CNT (UD and FG-X) is considered. The dimensional transverse deflection response of the thin FG-CNT reinforced plate subjected to two different boundary condition (SSSS and SCSC) under thermal loading ($T_2 = 100$, $T_1 = T_3 = 0$) for different mesh size is obtained and indicated in Fig. 4.17. Similar convergence behavior is observed as that of the thick plates ($a/h = 10$) and on that basis, the further studies are carried out at a mesh size of (10 × 10) i.e. with 100 elements.

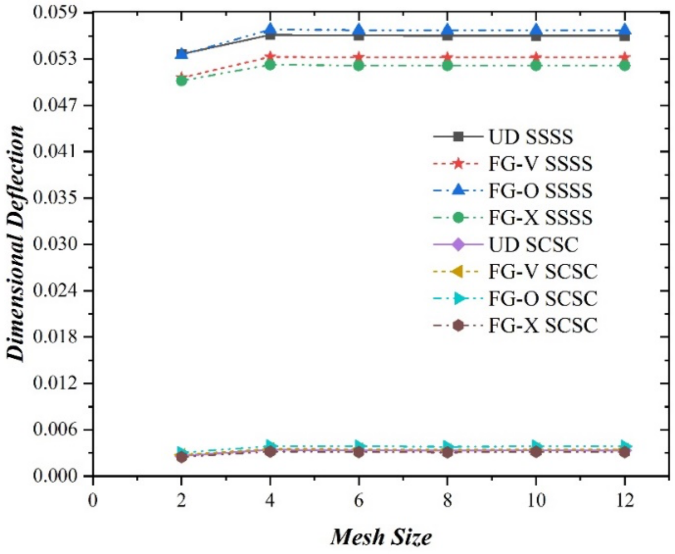

Fig. 4-16: Convergence study for dimensional transverse deflection of the thick (*a/h* = 10) FG-CNTRC plate for different mesh size, two different distributions of CNT and two different boundary conditions under uniform thermal loading

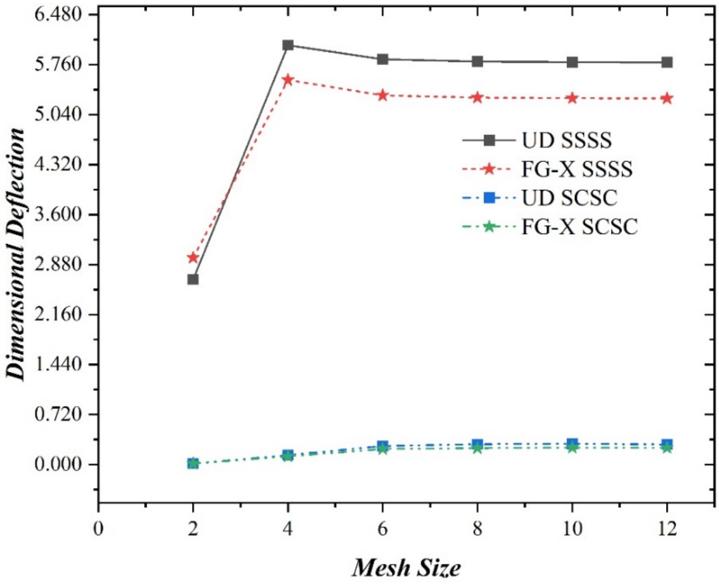

Fig. 4-17: Convergence study for dimensional transverse deflection of the thin (*a/h* = 100) FG-CNTRC plate for different mesh size, two different distributions of CNT and two different boundary conditions under uniform thermal loading

4.6.2. Hygro-thermo-mechanical response of the FG-CNT reinforced plate

For this study, a simply supported thick to moderately thin FG-CNT reinforced plate with volume fraction (0.11, 0.14, 0.17), plate span to thickness ratio (10, 20, 50) and CNT distribution (UD, FG-V, O, X) is considered. The plate is subjected to uniform thermal load (T_2 = 100) varying linearly along the thickness direction (T_1, T_3 = 0) and thermo-mechanical load ($T_2 = 100$ and $q = 1 \times 10^5$). The effect of different temperature loading on the dimensional transverse deflection is demonstrated in Table 4.25.

Table 4.25: Dimensional transverse deflection (in mm) of square FG-CNTRC plate for different and *a/h* ratio under thermal ($T_2 = 100$, $T_1 = T_3 = 0$, $q = 0$) and thermo-mechanical ($q = 1\times10^5$, $T_2 = 100$) loading condition with SSSS boundary condition

V^*_{CNT}	*a/h*	Type of CNT distribution	T_2		$q + T_2$	
			CFS	FEM	CFS	FEM
0.11	10	UD	5.606×10^{-2}	5.608×10^{-2}	5.938×10^{-2}	5.944×10^{-2}
		FG-V	5.323×10^{-2}	5.329×10^{-2}	5.726×10^{-2}	5.735×10^{-2}
		FG-O	5.676×10^{-2}	5.678×10^{-2}	6.175×10^{-2}	6.177×10^{-2}
		FG-X	5.215×10^{-2}	5.227×10^{-2}	5.490×10^{-2}	5.507×10^{-2}
	20	UD	0.2230	0.2232	0.2576	0.2579
		FG-V	0.2133	0.2134	0.2599	0.2602
		FG-O	0.2273	0.2275	0.2871	0.2872
		FG-X	0.2070	0.2073	0.2324	0.2329
	50	UD	1.3874	1.3899	2.5277	2.5326
		FG-V	1.3316	1.3336	2.9483	2.9526
		FG-O	1.4199	1.4220	3.5258	3.5295
		FG-X	1.2838	1.2863	2.0660	2.0708
0.14	10	UD	5.444×10^{-2}	5.447×10^{-2}	5.734×10^{-2}	5.741×10^{-2}
		FG-V	5.097×10^{-2}	5.106×10^{-2}	5.445×10^{-2}	5.457×10^{-2}
		FG-O	5.590×10^{-2}	5.592×10^{-2}	6.020×10^{-2}	6.022×10^{-2}
		FG-X	4.924×10^{-2}	4.940×10^{-2}	5.169×10^{-2}	5.190×10^{-2}
	20	UD	0.2157	0.2159	0.2442	0.2445
		FG-V	0.2040	0.2042	0.2423	0.2426
		FG-O	0.2231	0.2232	0.2723	0.2724
		FG-X	0.1952	0.1956	0.2164	0.2168
	50	UD	1.3392	1.3417	2.2443	2.2489
		FG-V	1.2724	1.2745	2.5701	2.5744
		FG-O	1.3911	1.3934	3.0919	3.0959
		FG-X	1.2082	1.2106	1.8275	1.8319
0.17	10	UD	5.260×10^{-2}	5.262×10^{-2}	5.474×10^{-2}	5.478×10^{-2}
		FG-V	4.841×10^{-2}	4.848×10^{-2}	5.101×10^{-2}	5.110×10^{-2}
		FG-O	5.420×10^{-2}	5.422×10^{-2}	5.740×10^{-2}	5.742×10^{-2}
		FG-X	4.648×10^{-2}	4.661×10^{-2}	4.826×10^{-2}	4.842×10^{-2}
	20	UD	0.2093	0.2095	0.2318	0.2320
		FG-V	0.1943	0.1944	0.2247	0.2249
		FG-O	0.2167	0.2169	0.2557	0.2558
		FG-X	0.1854	0.1856	0.2019	0.2023
	50	UD	1.3029	1.3052	2.0466	2.0504
		FG-V	1.2136	1.2154	2.2742	2.2774
		FG-O	1.3531	1.3552	2.7371	2.7401
		FG-X	1.1513	1.1535	1.6613	1.6647

To ensure the validation of finite element solutions (FEM), the results for SSSS plate are validated with independently obtained CFS and presented in the tabulated form. It is observed that the percentage error range between CFS and FEM solutions is 0.03 % to 1.0 % for all the obtained results. It is also revealed that the distribution of CNTs along the thickness direction significantly influences the non-dimensional transverse deflection. However, FG-X distribution reflects the minimum response to the uniform temperature field followed by UD, FG-V and FG-O. This is due to the distribution of CNT more on the top and bottom of FG-X which increases the stiffness of the FG-CNT reinforced plate. The dimensional deflection decreases with increase the volume fraction of CNT in the matrix material. Moreover, with an increase in the volume fraction from 0.11 to 0.14, the dimensional transverse deflection decreases by 2.9 % in case of FEM solution. Similarly, with an increase in the volume fraction from 0.11 to 0.17, the dimensional transverse deflection decreases by 6.2 % in the case of FEM solution.

In another study, a FG-CNT reinforced plate with simply supported boundary conditions is considered. The effect of volume fraction (0.11, 0.14 and 0.17), span to thickness ratio (a/h = 10, 20 and 50), distribution of CNT (UD, FG-V, FG-O and FG-X) on the dimensional transverse deflection of the plate under the action of hygro-thermo-mechanical loading are obtained and the results are presented Table 4.26. The FG-CNT reinforced plate is subjected to hygro-thermal ($T_2 = 100$ and $c_2 = 0.01$) and hygro-thermo-mechanical loading ($q = 1 \times 10^5$, $T_2 = 100$ and $c_2 = 0.01$). A closed form solution of Navier type and finite element solution is presented to ensure the accuracy of the obtained solution. It is observed that the percentage difference of finite element solution with respect to present closed form solution lies in the range of 0.03 % to 1.0 %. The simply supported FG-CNT reinforced plate is more affected by the hygro-thermo-mechanical load with respect to the hygro-thermal load. The dimensional transverse deflection increases with increases in the span to thickness ratio. It is concluded that transverse deflection increases or decreases with the type of dispersion used in the matrix material. In addition, the FG-X distribution has the least response among the other three distributions.

Table 4.26: Dimensional transverse deflection (in mm) of square FG-CNTRC plate for different and *a/h* ratio under hygro-thermal and hygro-thermo-mechanical loading condition with SSSS boundary condition

V^*_{CNT}	*a/h*	Type of CNT distribution	$T_2 + c_2$		$q + T_2 + c_2$	
			CFS	FEM	CFS	FEM
0.11	10	UD	5.962×10^{-2}	5.968×10^{-2}	6.294×10^{-2}	6.304×10^{-2}
		FG-V	5.826×10^{-2}	5.835×10^{-2}	6.229×10^{-2}	6.241×10^{-2}
		FG-O	6.354×10^{-2}	6.357×10^{-2}	6.854×10^{-2}	6.857×10^{-2}
		FG-X	5.462×10^{-2}	5.481×10^{-2}	5.737×10^{-2}	5.761×10^{-2}
	20	UD	0.2336	0.2338	0.2682	0.2686
		FG-V	0.2299	0.2302	0.2765	0.2769
		FG-O	0.2502	0.2503	0.3099	0.3101
		FG-X	0.2135	0.2138	0.2389	0.2394
	50	UD	1.4477	1.4500	2.5880	2.5927
		FG-V	1.4296	1.4317	3.0463	3.0507
		FG-O	1.5547	1.5570	3.6606	3.6644
		FG-X	1.3189	1.3212	2.1010	2.1057
0.14	10	UD	5.742×10^{-2}	5.749×10^{-2}	6.032×10^{-2}	6.043×10^{-2}
		FG-V	5.521×10^{-2}	5.533×10^{-2}	5.869×10^{-2}	5.885×10^{-2}
		FG-O	6.165×10^{-2}	6.168×10^{-2}	6.594×10^{-2}	6.597×10^{-2}
		FG-X	5.135×10^{-2}	5.158×10^{-2}	5.380×10^{-2}	5.408×10^{-2}
	20	UD	0.2240	0.2242	0.2524	0.2528
		FG-V	0.2174	0.2176	0.2557	0.2561
		FG-O	0.2416	0.2418	0.2908	0.2910
		FG-X	0.2002	0.2006	0.2213	0.2219
	50	UD	1.3848	1.3872	2.2899	2.2944
		FG-V	1.3498	1.3519	2.6475	2.6518
		FG-O	1.4988	1.5011	3.1996	3.2037
		FG-X	1.2340	1.2362	1.8533	1.8575
0.17	10	UD	5.585×10^{-2}	5.591×10^{-2}	5.798×10^{-2}	5.807×10^{-2}
		FG-V	5.305×10^{-2}	5.316×10^{-2}	5.565×10^{-2}	5.578×10^{-2}
		FG-O	6.034×10^{-2}	6.037×10^{-2}	6.354×10^{-2}	6.356×10^{-2}
		FG-X	4.883×10^{-2}	4.902×10^{-2}	5.062×10^{-2}	5.083×10^{-2}
	20	UD	0.2187	0.2189	0.2411	0.2414
		FG-V	0.2093	0.2095	0.2397	0.2400
		FG-O	0.2371	0.2373	0.2761	0.2763
		FG-X	0.1911	0.1914	0.2077	0.2080
	50	UD	1.3547	1.3569	2.0984	2.1021
		FG-V	1.3014	1.3033	2.3620	2.3653
		FG-O	1.4732	1.4754	2.8571	2.8603
		FG-X	1.1811	1.1831	1.6910	1.6944

Thereafter, an FG-CNT reinforced plate with volume fraction (V^*_{CNT} = 0.17) and FG-X distribution with SSSS constraints is considered under the uniform non-linear temperature field (T_2 = T_3 = 100) and non-linear moisture field (c_2 = c_3 = 0.01). The influence of span to thickness ratio on the dimensional transverse deflection is illustrated in Fig. 4.18. It is noted that with increment in span to thickness ratio, the deflection increases. Moreover, the FG-CNT reinforced plate experiences the lower deformation due to the non-linear moisture field relative to that due to the non-linear temperature field.

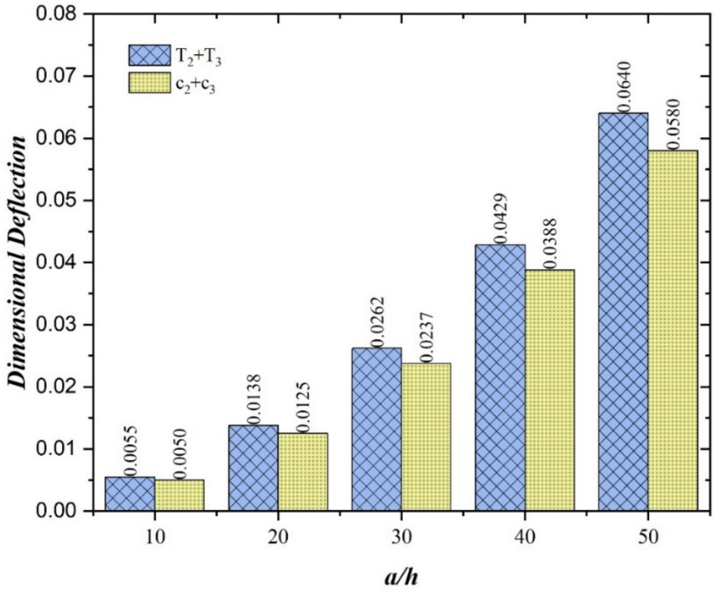

Fig. 4-18: Effect of temperature ($T_2 = T_3 = 100$) and moisture ($c_2 = c_3 = 0.01$) on the dimensional deflection of FG-CNTRC plate with SCSC boundary condition exposed to hygro-thermal environment

In the next example, the influence of volume fraction on the dimensional transverse deflection is observed for two edges simply supported and two edges clamped (SCSC) FG-CNT reinforced plate with FG-X distribution and span to thickness ratio (a/h=10). The numerical results are presented for non-linear temperature (T_2 = T_3 = 100), and non-linear moisture (c_2 = c_3 = 0.01) in Fig. 4.19. A decrement in the dimensional transverse deflection is observed with an increment in volume fraction for the non-linear temperature field. Moreover, an increment in dimensional transverse deflection is observed due to an increment in volume fraction for the non-linear moisture field. It is also depicted that at volume fraction (V_{CNT} = 0.11), the dimensional deflection is more affected by the non-linear temperature field than the non-linear moisture field. Similarly, at volume fraction (V_{CNT} = 0.28), the dimensional deflection is more affected by the moisture field than the non-linear temperature field.

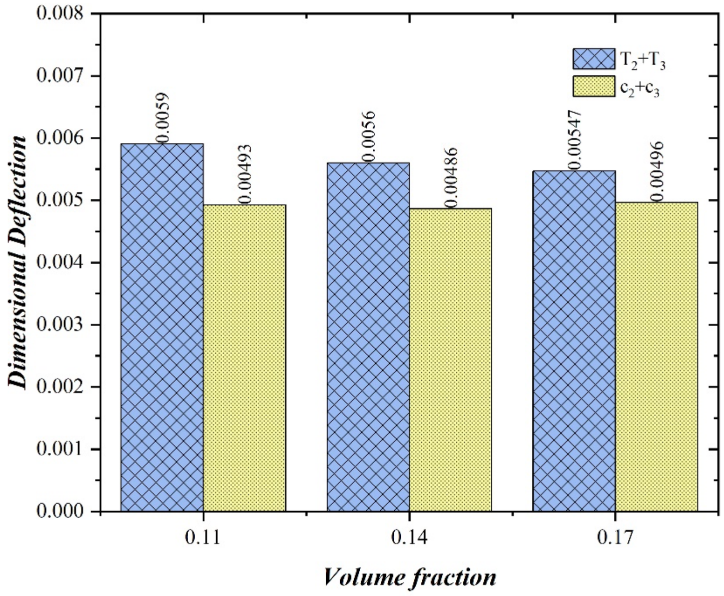

Fig. 4-19: Influence of non-linear temperature and moisture on the FG-CNT reinforced plate with SCSC boundary conditions

Thereafter, a FG-CNTR plate with span to thickness ratio (*a/h* = 10) and two edges simply supported and two edges clamped is considered under the influence of uniform hygro-thermo-mechanical load ($q = 1\times10^5$, $T_2 = T_3 = 100$ and $c_2 = c_3 = 0.01$). The effect of volume fraction on dimensional transverse deflection is presented in Fig. 4.20. With increment in the volume fraction, a decrement in the transverse deflection is noticed. Moreover, rate of decrement is more in the FG-CNT reinforced plate with SSSS boundary condition than the FG-CNT reinforced plate with SCSC boundary condition.

Further, the influence of span to thickness ratio (*a/h*) on the dimensional transverse deflection of the FG-CNT reinforced plate under the effect of hygro-thermo-mechanical ($q = 1 \times 10^5$, $T_2 = T_3 = 100$ and $c_2 = c_3 = 0.01$) loading condition is illustrated in Fig. 4.21. The FEM results are presented for SSSS and SCSC boundary conditions. With the increase in span to thickness ratio, the increment in the dimensional deflection is observed more in the FG-CNT reinforced plate with SSSS boundary condition than that of the FG-CNT reinforced plate with SCSC boundary condition. This is due to the constraints imposed by the clamped boundary condition on the FG-CNT reinforced plate. In addition, the moderately thin plate is more affected by hygro-thermo-mechanical loading conditions, whereas the thick plate is least affected.

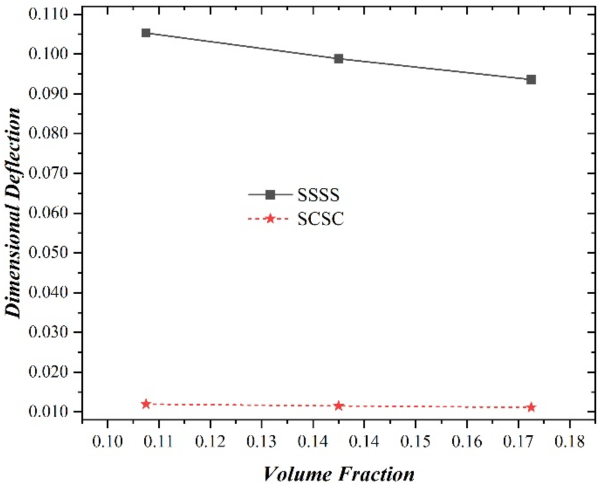

Fig. 4-20: Influence of CNT volume fraction on the deflection of FG-CNTRC plate with different (SSSS and SCSC) boundary constraints under the action of hygro-thermo-mechanical loading (q+T_2+T_3+c_2+c_3)

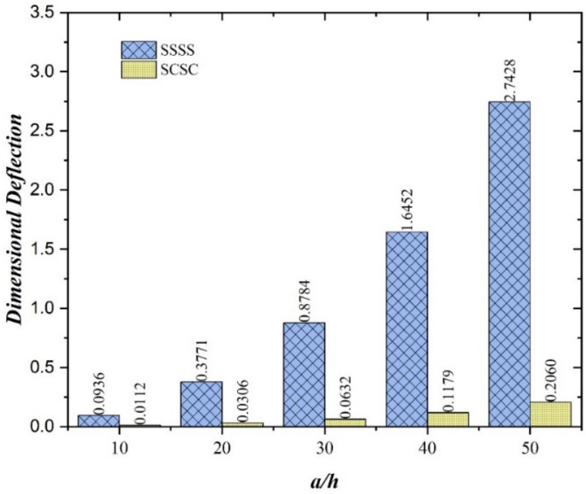

Fig. 4-21: The influence of *a/h* ratio on the dimensional deflection exposed to hygro-thermo-mechanical loading condition

Further, a FG-CNT reinforced plate with three edges simply supported and one edge clamped is considered under different temperature and moisture loading conditions. Effect of volume fraction, span to thickness ratio and distributions of CNT on the transverse deflection of FG-CNT reinforced plate is indicated in Table 4.27. The results are presented for dimensional transverse deflection for FG-CNT reinforced plate subjected to thermal ($T_2 = 100$, $T_1 = T_3 = 0$), thermo-mechanical ($T_2 = 100$, $q = 1 \times 10^5$), hygro-thermal ($T_2 = 100$, $c_2 = 0.01$) and hygro-thermo-mechanical ($q = 1 \times 10^5$, $T_2 = 100$, $c_2 = 0.01$) environment conditions. It is seen that the transverse deflection decreases as the volume fraction of CNT increase.

Table 4.27: Dimensional transverse deflection (in mm) of square FG-CNTRC plate for different and *a/h* ratio with SCSS boundary constraints under different loading condition

V_{CNT}^{*}	*a/h*	Type of CNT distribution	T_2	$q+T_2$	T_2+c_2	$q+T_2+c_2$
			FEM	FEM	FEM	FEM
0.11	10	UD	2.499×10^{-2}	2.746×10^{-2}	2.695×10^{-2}	2.939×10^{-2}
		FG-V	2.223×10^{-2}	2.502×10^{-2}	2.479×10^{-2}	2.753×10^{-2}
		FG-O	2.336×10^{-2}	2.672×10^{-2}	2.667×10^{-2}	3.002×10^{-2}
		FG-X	2.553×10^{-2}	2.773×10^{-2}	2.706×10^{-2}	2.926×10^{-2}
	20	UD	7.458×10^{-2}	9.270×10^{-2}	8.050×10^{-2}	9.778×10^{-2}
		FG-V	7.017×10^{-2}	9.351×10^{-2}	7.792×10^{-2}	9.997×10^{-2}
		FG-O	7.533×10^{-2}	0.1053	8.467×10^{-2}	0.1132
		FG-X	7.220×10^{-2}	8.681×10^{-2}	7.694×10^{-2}	9.103×10^{-2}
	5	UD	0.4157	0.8983	0.4459	0.9197
		FG-V	0.4004	1.0986	0.4447	1.1230
		FG-O	0.4337	1.3596	0.4876	1.3958
		FG-X	0.3896	0.7242	0.4096	0.7434
0.14	10	UD	2.533×10^{-2}	2.756×10^{-2}	2.706×10^{-2}	2.926×10^{-2}
		FG-V	2.195×10^{-2}	2.444×10^{-2}	2.422×10^{-2}	2.666×10^{-2}
		FG-O	2.343×10^{-2}	2.639×10^{-2}	2.631×10^{-2}	2.924×10^{-2}
		FG-X	2.546×10^{-2}	2.753×10^{-2}	2.688×10^{-2}	2.894×10^{-2}
	20	UD	7.346×10^{-2}	8.894×10^{-2}	7.885×10^{-2}	9.375×10^{-2}
		FG-V	6.750×10^{-2}	8.699×10^{-2}	7.448×10^{-2}	9.291×10^{-2}
		FG-O	7.365×10^{-2}	9.845×10^{-2}	8.200×10^{-2}	0.1054
		FG-X	7.055×10^{-2}	8.327×10^{-2}	7.469×10^{-2}	8.711×10^{-2}
	50	UD	0.4035	0.7871	0.4280	0.8078
		FG-V	0.3820	0.9342	0.4188	0.9571
		FG-O	0.4188	1.1553	0.4664	1.1821
		FG-X	0.3707	0.6408	0.3877	0.6572
0.17	10	UD	2.328×10^{-2}	2.486×10^{-2}	2.513×10^{-2}	2.667×10^{-2}
		FG-V	2.010×10^{-2}	2.189×10^{-2}	2.255×10^{-2}	2.428×10^{-2}
		FG-O	2.193×10^{-2}	2.405×10^{-2}	2.497×10^{-2}	2.704×10^{-2}
		FG-X	2.275×10^{-2}	2.417×10^{-2}	2.426×10^{-2}	2.566×10^{-2}
	20	UD	6.982×10^{-2}	8.140×10^{-2}	7.539×10^{-2}	8.637×10^{-2}
		FG-V	6.389×10^{-2}	7.891×10^{-2}	7.132×10^{-2}	8.525×10^{-2}
		FG-O	7.136×10^{-2}	9.055×10^{-2}	8.026×10^{-2}	9.803×10^{-2}
		FG-X	6.463×10^{-2}	7.408×10^{-2}	6.910×10^{-2}	7.820×10^{-2}
	50	UD	0.3901	0.7013	0.4183	0.7224
		FG-V	0.3657	0.8220	0.4079	0.8457
		FG-O	0.4132	1.0173	0.4641	1.0489
		FG-X	0.3489	0.5645	0.3678	0.5828

Table 4.28: Dimensional transverse deflection (in mm) of square FG-CNTRC plate for different and *a/h* ratio with SCSC boundary constraints under different loading condition

V_{CNT}^{*}	*a/h*	*Type of CNT distribution*	T_2	$q+T_2$	T_2+c_2	$q+T_2+c_2$
			FEM	*FEM*	*FEM*	*FEM*
0.11	10	UD	3.300×10^{-3}	4.565×10^{-3}	6.050×10^{-3}	7.263×10^{-3}
		FG-V	3.430×10^{-3}	4.818×10^{-3}	6.289×10^{-3}	7.576×10^{-3}
		FG-O	3.807×10^{-3}	5.462×10^{-3}	6.976×10^{-3}	8.508×10^{-3}
		FG-X	3.092×10^{-3}	4.270×10^{-3}	5.671×10^{-3}	6.806×10^{-3}
	20	UD	8.622×10^{-3}	1.731×10^{-2}	1.581×10^{-2}	2.434×10^{-2}
		FG-V	9.412×10^{-3}	2.011×10^{-2}	1.726×10^{-2}	2.744×10^{-2}
		FG-O	1.076×10^{-2}	2.407×10^{-2}	1.971×10^{-2}	3.200×10^{-2}
		FG-X	7.767×10^{-3}	1.507×10^{-2}	1.425×10^{-2}	2.139×10^{-2}
	50	UD	4.274×10^{-2}	0.2672	7.835×10^{-2}	0.2870
		FG-V	4.906×10^{-2}	0.3640	8.994×10^{-2}	0.3832
		FG-O	5.642×10^{-2}	0.4734	0.1034	0.4926
		FG-X	3.584×10^{-2}	0.1958	6.574×10^{-2}	0.2140
0.14	10	UD	3.143×10^{-3}	4.298×10^{-3}	5.861×10^{-3}	6.989×10^{-3}
		FG-V	3.245×10^{-3}	4.497×10^{-3}	6.051×10^{-3}	7.236×10^{-3}
		FG-O	3.606×10^{-3}	5.068×10^{-3}	6.712×10^{-3}	8.059×10^{-3}
		FG-X	2.934×10^{-3}	4.036×10^{-3}	5.483×10^{-3}	6.547×10^{-3}
	20	UD	8.061×10^{-3}	1.566×10^{-2}	1.503×10^{-2}	2.246×10^{-2}
		FG-V	8.651×10^{-3}	1.784×10^{-2}	1.613×10^{-2}	2.508×10^{-2}
		FG-O	9.902×10^{-3}	2.121×10^{-2}	1.843×10^{-2}	2.916×10^{-2}
		FG-X	7.247×10^{-3}	1.381×10^{-2}	1.354×10^{-2}	1.991×10^{-2}
	50	UD	3.850×10^{-2}	0.2189	7.179×10^{-2}	0.2392
		FG-V	4.429×10^{-2}	0.2968	8.260×10^{-2}	0.3163
		FG-O	5.147×10^{-2}	0.3837	9.581×10^{-2}	0.4046
		FG-X	3.205×10^{-2}	0.1634	5.989×10^{-2}	0.1798
0.17	10	UD	3.114×10^{-3}	3.883×10^{-3}	5.909×10^{-3}	6.678×10^{-3}
		FG-V	3.232×10^{-3}	4.065×10^{-3}	6.136×10^{-3}	6.952×10^{-3}
		FG-O	3.618×10^{-3}	4.588×10^{-3}	6.842×10^{-3}	7.769×10^{-3}
		FG-X	2.869×10^{-3}	3.590×10^{-3}	5.469×10^{-3}	6.191×10^{-3}
	20	UD	8.163×10^{-3}	1.367×10^{-2}	1.549×10^{-2}	2.091×10^{-2}
		FG-V	8.944×10^{-3}	1.548×10^{-2}	1.698×10^{-2}	2.352×10^{-2}
		FG-O	1.032×10^{-2}	1.837×10^{-2}	1.952×10^{-2}	2.738×10^{-2}
		FG-X	7.213×10^{-3}	1.189×10^{-2}	1.375×10^{-2}	1.832×10^{-2}
	50	UD	4.072×10^{-2}	0.1794	7.728×10^{-2}	0.2044
		FG-V	4.678×10^{-2}	0.2447	8.883×10^{-2}	0.2708
		FG-O	5.478×10^{-2}	0.3159	0.1036	0.3426
		FG-X	3.350×10^{-2}	0.1334	6.386×10^{-2}	0.1550

In order to study the influence of thermal, thermo-mechanical, hygro-thermal and hygro-thermo-mechanical loadings on the dimensional deflection, the two edges simply supported and two edges clamped FG-CNT reinforced plate is considered. The effect of volume fraction, span to thickness ratio and distributions of CNT on FG-CNT reinforced plate is tabulated in Table 4.28. It is observed that the FG-CNT reinforced plate with SCSC boundary conditions is more affected by hygro-thermo-mechanical loading followed by hygro-thermal, thermo-mechanical and thermal loading. It is seen that dimensional deflection having FG-X distribution is lowest, while the dimensional deflection having FG-O distribution is highest among the various distributions. With the increase in volume fraction from 0.11 to 0.14, the dimensional deflection is decreased for thermal loading by 4.8%. Similarly, increase in volume fraction from 0.11 to 0.17, the dimensional deflection is decreased for thermal loading condition by 5.7 %. The dimensional deflection increases with increases in the span to thickness ratio. In addition, for a particular case (V_{CNT} = 0.11, UD and thermal loading condition), the dimensional deflection is increased by 161.2% when the span to thickness ratio increases from 10 to 20.

4.7. Bending Analysis of Cracked FG-CNT Reinforced Plate

In this section, bending analysis of cracked plate is performed using extended finite element method (XFEM) under uniformly distributed loading along with different set of boundary conditions. A pre-exiting crack with variable crack length (function of the length of the plate) is considered in the FG-CNT reinforced plate, to examine the effect of crack on the transverse deflection of the plate. The Heaviside and crack tip enrichment functions are employed to model the crack face and crack tip, respectively. The Gauss quadrature rule is employed to perform the integration in the domain. Whereas, the sub-triangulation technique is employed to integrate the discontinuous elements. A generalized MATLAB code is developed using the XFEM in order to formulate the surface crake on the FG-CNT reinforced plate. The material properties of the matrix and reinforced CNT are temperature-dependent. The properties PmPV matrix and CNT material are taken same as indicated in Section 4.3. The effect of the volume fraction of CNT, distribution of CNT, span to thickness ratio, crack length and boundary conditions is examined on the transverse deflection of the FG-CNT reinforced plate.

The static response of FG-CNT reinforced cracked plate is examined subjected to the uniform load. The properties of the material are assumed to be temperature dependent; however, the response is evaluated at T = 300 K. The location of the crack along y-axis is assumed as 0.6 times the width of the plate ($y = 0.6 \times b$). The crack length (L_c) (along the x-axis) is assumed as 0.15a, 0.3a, 0.5a, and 0.7a where a is the length of the plate. The volume fraction of the CNT is taken as 0.11 for the bending analysis. The non-dimensional transverse deflection $\overline{w} = 100wE_m h^3 / a^4$ is tabulated in Table 4.29 and Table 4.30 for thin plates (a/h =100 and 50) and moderately thick plates (a/h =20 and 10) respectively with various crack lengths, distribution of CNT (UD, FG-V, FG-O and FG-X) and different boundary conditions (SSSS, SCSS and SCSC). It is observed that FG-X distribution of CNT along with SCSC boundary condition is least affected by the presence of crack in the FG-CNT reinforced plate. With the increase in the crack length from 0.15 to 0.7 (a/h = 100, UD), the non-dimensional transverse deflection is increased by 2.3 %.

Table 4.29: Non dimensional transverse deflection of square FG-CNTRC plate (V^*_{CNT}) for thin plates (*a/h* = 100, 50) with different crack lengths under the action of UDL

a/h	*Lc*	Type of CNT distribution	Non-dimensional central deflection		
			SSSS	SCSS	SCSC
100	0.15	UD	0.3764	0.156	0.077
		FG-V	0.5441	0.2289	0.1106
		FG-O	0.7139	0.305	0.1466
		FG-X	0.2537	0.1061	0.0532
	0.2	UD	0.3765	0.1560	0.0770
		FG-V	0.5441	0.2289	0.1106
		FG-O	0.7140	0.3051	0.1466
		FG-X	0.2537	0.1061	0.0532
	0.25	UD	0.3764	0.1560	0.0770
		FG-V	0.5441	0.2289	0.1106
		FG-O	0.7140	0.3051	0.1466
		FG-X	0.2537	0.1061	0.0532
	0.3	UD	0.3766	0.1561	0.0770
		FG-V	0.5444	0.2290	0.1107
		FG-O	0.7145	0.3052	0.1467
		FG-X	0.2538	0.1061	0.0532
50	0.15	UD	0.3889	0.1701	0.0892
		FG-V	0.5562	0.2434	0.1231
		FG-O	0.7275	0.3217	0.1613
		FG-X	0.2661	0.1195	0.0651
	0.2	UD	0.3889	0.1702	0.0893
		FG-V	0.5563	0.2434	0.1231
		FG-O	0.7276	0.3217	0.1613
		FG-X	0.2661	0.1195	0.0652
	0.25	UD	0.3889	0.1702	0.0892
		FG-V	0.5563	0.2434	0.1231
		FG-O	0.7276	0.3217	0.1613
		FG-X	0.2661	0.1195	0.0652
	0.3	UD	0.3891	0.1703	0.0893
		FG-V	0.5567	0.2435	0.1232
		FG-O	0.7283	0.322	0.1613
		FG-X	0.2662	0.1196	0.0652

Table 4.30: Non dimensional transverse deflection of square FG-CNTRC plate (V_{CNT}^{*}) for moderately thick plates (a/h = 20 and 10) with different crack lengths under the action of UDL

a/h	L_C	Type of CNT distribution	Non-dimensional central deflection		
			SSSS	SCSS	SCSC
20	0.15	UD	0.4757	0.2691	0.172
		FG-V	0.6401	0.3418	0.207
		FG-O	0.821	0.4334	0.2584
		FG-X	0.3529	0.2156	0.1461
	0.2	UD	0.4758	0.2691	0.1721
		FG-V	0.6403	0.3419	0.2072
		FG-O	0.8214	0.4335	0.2586
		FG-X	0.3529	0.2156	0.1463
	0.25	UD	0.4761	0.269	0.1761
		FG-V	0.6408	0.3421	0.2114
		FG-O	0.822	0.4342	0.2632
		FG-X	0.3532	0.2157	0.1495
	0.3	UD	0.4761	0.2692	0.1722
		FG-V	0.641	0.3421	0.2072
		FG-O	0.8225	0.4339	0.2586
		FG-X	0.3531	0.2157	0.1463
10	0.15	UD	0.7765	0.6017	0.4667
		FG-V	0.9302	0.6728	0.5006
		FG-O	1.1429	0.8049	0.5878
		FG-X	0.6546	0.5412	0.4366
	0.2	UD	0.7768	0.6019	0.467
		FG-V	0.9306	0.6731	0.5009
		FG-O	1.1436	0.8053	0.588
		FG-X	0.6548	0.5413	0.4369
	0.25	UD	0.7778	0.603	0.471
		FG-V	0.9319	0.6741	0.5054
		FG-O	1.1451	0.8064	0.5931
		FG-X	0.6557	0.5421	0.4404
	0.3	UD	0.7777	0.6025	0.4672
		FG-V	0.9321	0.674	0.5011
		FG-O	1.1457	0.8067	0.5882
		FG-X	0.6555	0.5418	0.4371

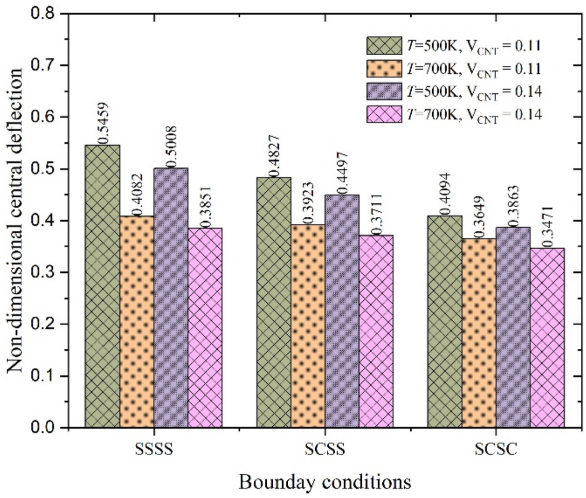

Fig. 4-22: Effect of different volume fractions of CNT, temperature dependent material properties and boundary conditions on the non-dimensional central deflection for the FG-CNT reinforced cracked plate with *a/h* = 10, FG-X distribution of CNT (with *Lc* = 0.2*a*) subjected to uniformly distributed load

The influence of volume fraction (0.11 & 0.14), temperature dependent material properties (at 500 K and 700 K) and boundary conditions (SSSS, SCSS and SCSC) is examined on the non-dimensional central deflection of a square thick (*a/h* = 10) FG-CNT (FG-X distribution) reinforced plate in the presence of surface crack (equal to 0.2 times the length of the plate) subjected to uniform distributed load. From Fig. 4.22, it is depicted that the non-dimensional central deflection decreases with increases in the temperature conditions from 500 K to 700 K for the FG-CNT reinforced plate. Moreover, the SCSC boundary condition has the least response in comparison to other two boundary conditions (SSSS and SCSS) when subjected to uniformly distributed loading condition. It is also observed that the non-dimensional central deflection decreases with an increase in the volume fraction of CNT from 0.11 to 0.14.

Further, the effect of different volume fractions (0.11 & 0.14), temperature dependent material properties (at 500 K and 700 K) and boundary conditions (SSSS, SCSS, SCSC) is investigated on the deflection of thin (*a/h* = 100) FG-CNT (FG-X) reinforced plate with surface crack (of 0.2 times the length of the plate) is presented in Fig. 4.23. When the volume fraction of the CNT increases, the incremental changes in the non-dimensional central deflection of SCSC plate are much smaller than the SSSS plate. This is due to presence of clamped boundary conditions which possess strong constraints. With the increase in the temperature condition from 500 K to 700 K, the non-dimensional deflection of thin FG-CNT reinforced plate decreases, which may attribute to the considered non-dimensionality for the obtained results.

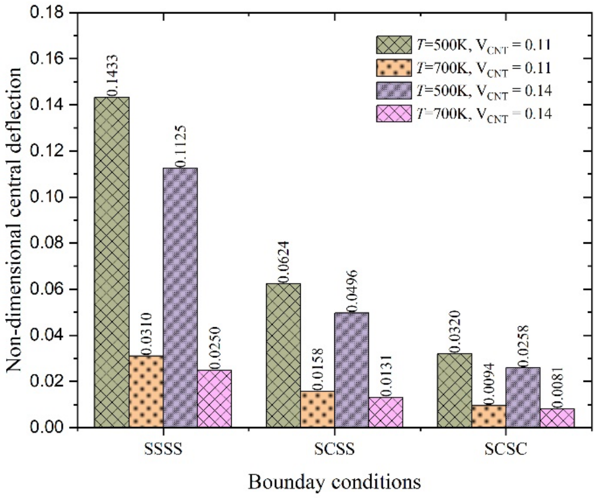

Fig. 4-23: Effect of different volume fractions of CNT, temperature dependent material properties and boundary conditions on the non-dimensional central deflection for the FG-CNT reinforced cracked plate with *a/h* = 100, FG-X distribution of CNT (L_C =0.2*a*)subjected to uniformly distributed load

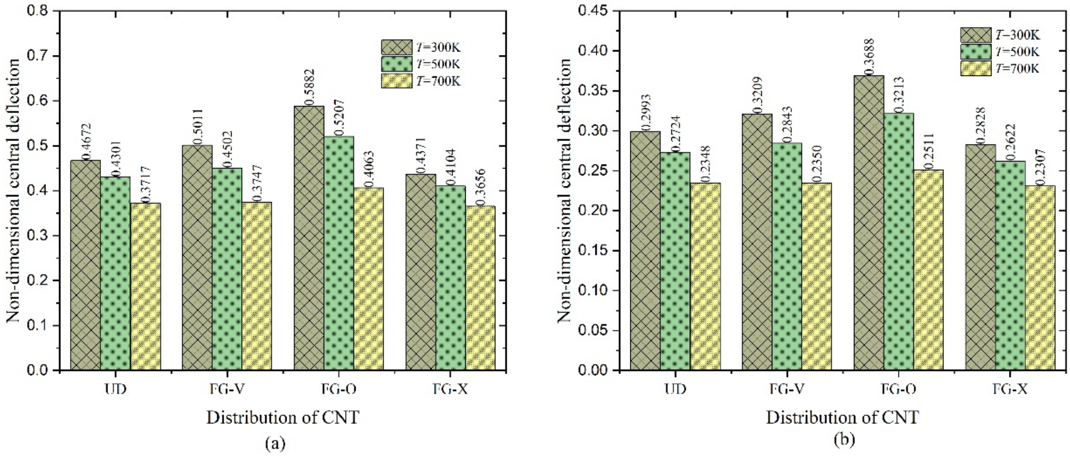

(a) (b)

Fig. 4-24: Effect of distribution of CNT on the non-dimensional central deflection of FG-CNT reinforced plate with L_C = 0.3*a*, *a/h*=10, SCSC boundary condition subjected to uniform distributed load

Moreover, the effect of temperature dependent material properties (considered at 300 K, 500 K and 700 K) and distribution of CNT (UD, FG-V, FG-O and FG-X) is examined on the non-dimensional central deflection of a square FG-CNT reinforced cracked thick plate (*a/h* = 10). The plate is subjected to uniformly distributed load along with SCSC boundary condition. Figures 4.24 (a) and (b) presents the non-dimensional central deflection of FG-CNT reinforced cracked plate considering volume fractions of CNT as 0.11 and 0.17, respectively. It is depicted that with increase in volume fraction of CNT, there is significant decrement in the non-dimensional central deflection. It is observed that the FG-X distribution of CNT possess the least value of non-dimensional central deflection in comparison to other distribution i.e. UD, FG-V and FG-O. With the increase in temperature condition, the significant decrement in non-dimensional central deflection is observed for all the distribution of CNT.

4.8. Summary

In this chapter, the results are obtained through MATLAB codes based on the formulation developed in Chapter 3 and presented categorically. The validity of the proposed IHSDT for FG-CNTRC plates is first ensured for the simply supported cross ply plates by presenting the analytical solution (Navier type) for the structural analysis (static, buckling and free vibration) of CNTRC plates. The analysis has been carried out with temperature independent as well as temperature dependent properties. The performance of the theories is checked against various existing theories and the exact solution. The comparison of the present results with the established results indicates the accuracy and the efficiency of the present IHSDTs for the structural behavior of the FG-CNTRC plates. Further, in order to enhance the range of applicability of IHSDTs to different boundary conditions and loading conditions, the finite element solutions are presented for a variety of cases along with the comparison with other numerical approaches and the performance of present FEM in conjunction with IHSDTs is ensured. The influence of diverse specification including the CNT distribution patterns, the CNT volume fraction, the span-thickness ratio, the boundary constraints, the aspect ratio, and the loading conditions on the structural response is carried out and, on that basis, observations are noted. Further, the response of CNTRC plate in hygro-thermal environment is carried out wherein the several combinations of hygro-thermo-mechanical loads (constant temperature, linear temperature changes as well as non-linear temperature change across thickness, linear moisture change as well as non-linear moisture change across the thickness) are considered and the effects of diverse specifications of CNTRC plates on the response characteristics are examined. In addition to these, a cracked CNTRC plate modelled in the framework of XFEM is analyzed to predict the influence of the crack on the response of the considered plate. A pre-existing crack parallel to the *x* axis and varying crack length is considered and the influence of the plates' specification on the cracked plate are examined.

Chapter 5 CONCLUSION

5.1. Concluding Remarks

In this work, IHSDT is formulated for structural (static, buckling and free vibration) and failure analysis of the CNT reinforced plates. The effective material properties of the CNT reinforced plate are assumed to be temperature dependent and estimated according to the extended rule of mixture. The CNT reinforced plates are modelled in the framework of IHSDT wherein the in-plane displacements are expressed using a non-polynomial function of thickness coordinate while the transverse displacement is assumed to be constant. The mathematical system of equations is obtained using the principle of virtual work by employing linear structural kinematics and generalised Hooke's law. A closed form solution is developed for the structural behaviour of FG-CNT reinforced plates which is free from any computational error. Further, a generalized C^0 continuous eight noded isoparametric serendipity finite element methodology is developed to handle the temperature dependent structural response for various boundary conditions, hygro-thermo-mechanical environment conditions. The structural response is evaluated for different volume fraction, span-to-thickness ratio, distribution of CNT and boundary conditions. Further, an extended finite element method is implemented to investigate the FG-CNT reinforced plate in the presence of surface crack. The following conclusions are made as follows:

- The implemented IHSDT is based on a non-polynomial shear strain shape function. The displacement field is chosen in such a way that it satisfies the zero transverse shear stress condition at the top and bottom of the plate in the thickness direction and does not require a shear correction factor. The effect of in-plane shear deformation in the displacements is defined using the shear strain shape function in terms of an inverse hyperbolic trigonometric function. It is concluded that IHSDT is capable to predict efficient and accurate structural responses of the CNT reinforced plates subjected to different loading condition, temperature and moisture conditions.
- The Navier type closed form solution is first developed for structural behaviour of the simply supported temperature dependent CNT reinforced plate and validation of the obtained results is compared with the existing results in the literature.

- The finite element methodology is then developed in order to enhance the applicability. An eight noded isoparametric serendipity element is selected to discretize the plate geometry. The formulated finite element methodology is implemented for the static, buckling and free vibration responses of the CNT reinforced plate. It is also implemented to study the effect of hygro-thermo-mechanical environment on the static behaviour of the FG-CNT reinforced plate.
- Further, in order to study the influence of presence of surface crack on the CNT reinforced plate, an XFEM is implemented to examine the static behaviour of the CNT reinforced plate. Heaviside function and crack tip enrichment function are used to model the crack face and crack tip of the CNT reinforced plate respectively.
- The distribution of CNT played a significant role in the structural analysis of CNT reinforced plates. The plate with FG-X distribution of CNT experiences the least deformation due to different loading conditions (uniformly distributed and sinusoidal) and possesses higher buckling load under in-plane loads (uni-axial compressive and bi-axial compressive and tensile load). This is due to the maximum distribution of CNT at the top and bottom of the plate, which improves the overall stiffness of the CNT-reinforced plate.
- The effect of volume fraction and boundary conditions on the FG-X distribution reinforced CNT plate reveals that due to the increase in volume fraction of CNT from 0.11 to 0.17, the dimensionless deflection reduces by 31.33 %, 24.47 %, 27.61 % and 24.53 % for SSSS, SCSS, SCSC and CCCC conditions respectively.
- The percentage difference of finite element solution with respect to the present closed form solution for buckling response of CNT reinforced plate lies in the range of 0.002 % to 2.5 %. Moreover, the buckling response of CNT reinforced plate is greatly affected by the temperature-dependent material properties. When the temperature is raised from 300 K to 700 K (V^*_{CNT} = 0.11, UD-CNT and SSSS boundary condition), the buckling parameter increase by 73.47 %.
- For the free vibration, the percentage difference of finite element solution with respect to the present closed form solution lies in the range of 0.0 % to 1.25 %. Moreover, the fundamental frequency increases by 32 % when increasing temperature conditions from 300 K to 700 K ($V^*_{CNT} = 0.11$, UD-CNT with SSSS boundary constraints).
- To ensure the validation of finite element solutions (FEM), the results for SSSS plate are validated with independently obtained closes form solutions (CFS) for bending

response of CNT reinforced plate subjected hygro-thermo-mechanical environment. It is observed that the percentage difference of finite element solution with respect to present closed form solution lies in the range of 0.03 % to 1.0 %.

- The effect of temperature dependent material properties significantly influences the bending response of the CNT reinforced plate in the presence of a surface crack. It is observed that the static response decreased by 88 % when increasing temperature conditions from 300 K to 700 K.
- Thus, the structural responses of CNT reinforced plate depend significantly on the CNT volume fraction, type of distribution, plate span to thickness ratio, aspect ratio and boundary conditions of the plate.

5.2. Significant Contributions of the Thesis

The thesis has made significant contributions by exploring the structural responses of CNT reinforced plates under varying temperature-dependent material properties. This has enabled an understanding of how the plates respond with different temperature dependent material properties. Additionally, the research has introduced new knowledge to the field by examining the effects of hygro-thermo-mechanical environmental conditions on CNT reinforced plates, including how they behave under real-life working conditions. The thesis has also investigated the structural behavior of CNT reinforced plates in the presence of cracks.

5.3. Scope for the Future Work

This section discusses some of the possible areas of research to which the presented work can be extended in future. Some possible extensions of future work as listed below.

- The present work can be extended by including the stretching effect and the material uncertainty while modeling the CNT reinforced composite plate.
- The present formulation can be extended to CNT reinforced smart composite by considering the piezomagnetic materials.
- The present work only contributed to static analysis of CNT reinforced plate in the presence of a surface crack. The presented work can be extended to response of CNT reinforced plate in the presence of strong and weak discontinuities such as a holes, inclusions and randomly oriented minor cracks.
- The present work can be extended to forced vibration response of CNT reinforced plate.

References

[1] Ashby, M.F., Shercliff, H. and Cebon, D., 2018. *Materials: engineering, science, processing and design*. Butterworth-Heinemann.

[2] Iijima, S., 1991. Helical microtubules of graphitic carbon. *Nature*, 354(6348), pp.56-58.

[3] Lu, J.P., 1997. Elastic properties of single and multilayered nanotubes. *Journal of physics and chemistry of solids*, 58(11), pp.1649-1652.

[4] Beg, S., Rahman, M., Jain, A., Saini, S., Hasnain, M.S., Swain, S., Imam, S., Kazmi, I. and Akhter, S., 2018. Emergence in the functionalized carbon nanotubes as smart nanocarriers for drug delivery applications. In *Fullerens, Graphenes and Nanotubes*, pp. 105-133.

[5] Tang, Z.K., Zhang, L., Wang, N., Zhang, X.X., Wen, G.H., Li, G.D., Wang, J.N., Chan, C.T. and Sheng, P., 2001. Superconductivity in 4 angstrom single-walled carbon nanotubes. *Science*, 292(5526), pp.2462-2465.

[6] Small, J.P., Shi, L. and Kim, P., 2003. Mesoscopic thermal and thermoelectric measurements of individual carbon nanotubes. *Solid State Communications*, 127(2), pp.181-186.

[7] Treacy, M.J., Ebbesen, T.W. and Gibson, J.M., 1996. Exceptionally high Young's modulus observed for individual carbon nanotubes. *Nature*, 381(6584), pp.678-680.

[8] Thostenson, E.T., Ren, Z. and Chou, T.W., 2001. Advances in the science and technology of carbon nanotubes and their composites: a review. *Composites Science and Technology*, 61(13), pp.1899-1912.

[9] Qian H, Greenhalgh ES, Shaffer MSP, Bismarck A. 2010 Carbon nanotube-based hierarchical composites: A review. *Journal of Materials Chemistry,* 20, pp. 4751-4762.

[10] Zhang, Q., Zhao, M., Liu, Y., Cao, A., Qian, W., Lu, Y. and Wei, F., 2009. Energy-absorbing hybrid composites based on alternate carbon-nanotube and inorganic layers. *Advanced Materials*, 21(28), pp.2876-2880.

[11] Chou, T.W., Gao, L., Thostenson, E.T., Zhang, Z. and Byun, J.H., 2010. An assessment of the science and technology of carbon nanotube-based fibers and composites. *Composites Science and Technology*, 70(1), pp.1-19.

[12] Carrera, E., 2002. Theories and finite elements for multilayered, anisotropic, composite plates and shells. *Archives of Computational Methods in Engineering*, 9, pp.87-140.

[13] Jang, J. and Han, S., 1999. Mechanical properties of glass-fibre mat/PMMA functionally gradient composite. *Composites Part A: Applied Science and Manufacturing*, 30(9), pp.1045-1053.

[14] Lianxi, H. and Erde, W., 2000. Fabrication and mechanical properties of SiCw/ZK51A magnesium matrix composite by two-step squeeze casting. *Materials Science and Engineering: A*, 278(1-2), pp.267-271.

[15] Allaoui, A., Bai, S., Cheng, H.M. and Bai, J.B., 2002. Mechanical and electrical properties of a MWNT/epoxy composite. *Composites Science and Technology*, 62(15), pp.1993-1998.

[16] Fidelus, J.D., Wiesel, E., Gojny, F.H., Schulte, K. and Wagner, H.D., 2005. Thermo-mechanical properties of randomly oriented carbon/epoxy nanocomposites. *Composites Part A: Applied Science and Manufacturing*, 36(11), pp.1555-1561.

[17] de Villoria, R.G., Miravete, A., Cuartero, J., Chiminelli, A. and Tolosana, N., 2006. Mechanical properties of SWNT/epoxy composites using two different curing cycles. *Composites Part B: Engineering*, 37(4-5), pp.273-277.

[18] Sharma, K. and Shukla M. 2012. Experimental Study of Mechanical Properties of Multiscale Carbon Fiber-Epoxy-CNT Composites. *Advanced Materials Research*, 383-390, pp. 2723-2727.

[19] Huang, B., Guo, Y., Wang, J., Du, J., Qian, Z., Ma, T. and Yi, L., 2017. Bending and free vibration analyses of antisymmetrically laminated carbon nanotube-reinforced functionally graded plates. *Journal of Composite Materials*, 51(22), pp.3111-3125.

[20] Ansari, R., Rouhi, S. and Eghbalian, M., 2017. On the elastic properties of curved carbon nanotubes/polymer nanocomposites: A modified rule of mixture. *Journal of Reinforced Plastics and Composites*, 36(14), pp.991-1008.

[21] Huang, T. and Gong, Y., 2018. A multiscale analysis for predicting the elastic properties of 3D woven composites containing void defects. *Composite Structures*, 185, pp.401-410.

[22] Shi, D.L., Feng, X.Q., Huang, Y.Y., Hwang, K.C. and Gao, H., 2004. The effect of nanotube waviness and agglomeration on the elastic property of carbon nanotube-reinforced composites. *Journal of Engineering Materials and Technology*, 126(3), pp.250-257.

[23] Han, Y. and Elliott, J., 2007. Molecular dynamics simulations of the elastic properties of polymer/carbon nanotube composites. *Computational Materials Science*, 39(2), pp.315-323.

[24] Gajbhiye, S.O., Singh, S.P., Vibration analysis of single-walled carbon nanocones using multiscale atomistic finite element method incorporating Tersoff–Brenner potential. *Applied. Physics A*, 120 (1), pp.271-286

[25] Singh, P.K., Sharma, K., Kumar, A. and Shukla, M. 2017. Effects of functionalization on the mechanical properties of multiwalled carbon nanotubes: A molecular dynamics approach. *Journal of Composite Materials*, 51(5), pp. 671-680.

[26] Ravindranath, P.K., Roy, S., Unnikrishnan, V., Wang, X., Xu, T., Baughman, R. and Lu, H., 2019. A multiscale model to study the enhancement in the compressive strength of multi-walled CNT sheet overwrapped carbon fiber composites. *Composite Structures*, 219, pp.170-178.

[27] Reddy, J.N. 1984. A Simple Higher-Order Theory for Laminated Composite Plates. *Journal of Applied Mechanics*, 51(4), pp. 745–752. doi:10.1115/1.3167719.

[28] Kant, T., Ravichandran, R.V., Pandya, B.N. and Mallikarjuna, B.N., 1988. Finite element transient dynamic analysis of isotropic and fibre reinforced composite plates using a higher-order theory. *Composite Structures*, 9(4), pp.319-342.

[29] Murthy, M.V.V., 1981. An improved transverse shear deformation theory for laminated antisotropic plates. NASA Technical paper (No. L-14533).

[30] Swaminathan, K. and Patil, S.S., 2007. Higher order refined computational model with 12 degrees of freedom for the stress analysis of antisymmetric angle-ply plates–analytical solutions. *Composite Structures*, 80(4), pp.595-608.

[31] Talha, M. and Singh, B., 2010. Static response and free vibration analysis of FGM plates using higher order shear deformation theory. *Applied Mathematical Modelling*, 34(12), pp.3991-4011.

[32] Touratier, M., 1991. An efficient standard plate theory. *International Journal of Engineering Science*, 29(8), pp.901-916.

[33] Shimpi, R.P., Arya, H. and Naik, N.K., 2003. A higher order displacement model for the plate analysis. *Journal of Reinforced Plastics and Composites*, 22(18), pp.1667-1688.

[34] Aydogdu, M., 2009. A new shear deformation theory for laminated composite plates. *Composite Structures*, 89(1), pp.94-101.

[35] El Meiche, N., Tounsi, A., Ziane, N. and Mechab, I., 2011. A new hyperbolic shear deformation theory for buckling and vibration of functionally graded sandwich plate. *International Journal of Mechanical Sciences*, 53(4), pp.237-247.

[36] Mantari, J.L., Oktem, A.S. and Guedes Soares, C. 2012. A new trigonometric shear deformation theory for isotropic, laminated composite and sandwich plates. *International Journal of Solids and Structures*, 49(1), pp. 43–53.

[37] Mantari, J.L., Bonilla, E.M. and Soares, C.G., 2014. A new tangential-exponential higher order shear deformation theory for advanced composite plates. *Composites Part B: Engineering*, 60, pp.319-328.

[38] Thai, C.H., Ferreira, A.J.M., Bordas, S.P.A., Rabczuk, T. and Nguyen-Xuan, H., 2014. Isogeometric analysis of laminated composite and sandwich plates using a new inverse trigonometric shear deformation theory. *European Journal of Mechanics-A/Solids*, 43, pp.89-108.

[39] Sarangan, S. and Singh, B.N. 2016. Higher-order closed-form solution for the analysis of laminated composite and sandwich plates based on new shear deformation theories. *Composite Structures*, 138, pp.391–403.

[40] Grover, N., Maiti, D.K. and Singh, B.N. 2013. A new inverse hyperbolic shear deformation theory for static and buckling analysis of laminated composite and sandwich plates. *Composite Structures*, 95, pp.667–675.

[41] Grover, N., Singh, B.N. and Maiti, D.K., 2013. New nonpolynomial shear-deformation theories for structural behavior of laminated-composite and sandwich plates. *AIAA Journal*, 51(8), pp.1861-1871.

[42] Shen, H.S., 2009. Nonlinear bending of functionally graded carbon nanotube-reinforced composite plates in thermal environments. *Composite Structures*, 91(1), pp.9-19.

[43] Alibeigloo, A., 2013. Static analysis of functionally graded carbon nanotube-reinforced composite plate embedded in piezoelectric layers by using theory of elasticity. *Composite Structures*, 95, pp.612-622.

[44] Zhang, L.W., Song, Z.G. and Liew, K.M., 2015. State-space Levy method for vibration analysis of FG-CNT composite plates subjected to in-plane loads based on higher-order shear deformation theory. *Composite Structures*, 134, pp.989-1003.

[45] Huang, B., Guo, Y., Wang, J., Du, J., Qian, Z., Ma, T. and Yi, L., 2017. Bending and free vibration analyses of antisymmetrically laminated carbon nanotube-reinforced functionally graded plates. *Journal of Composite Materials*, 51(22), pp.3111-3125.

[46] Wang, A., Chen, H., Hao, Y. and Zhang, W., 2018. Vibration and bending behavior of functionally graded nanocomposite doubly-curved shallow shells reinforced by graphene nanoplatelets. *Results in Physics*, 9, pp.550-559.

[47] Soni, A., Grover, N., Bhardwaj, G. and Singh, B.N., 2020. Non-polynomial framework for static analysis of functionally graded carbon nano-tube reinforced plates. *Composite Structures*, 233, p.111569.

[48] Singh, S.D. and Sahoo, R., 2020. Static and free vibration analysis of functionally graded CNT reinforced composite plates using trigonometric shear deformation theory. *Structures*, 28, pp. 685-696.

[49] Bousahla, A.A., Bourada, F., Mahmoud, S.R., Tounsi, A., Algarni, A., Bedia, E.A. and Tounsi, A., 2020. Buckling and dynamic behavior of the simply supported CNT-RC beams using an integral-first shear deformation theory. *Computers and Concrete, An International Journal*, 25(2), pp.155-166.

[50] Bourada, F., Bousahla, A.A., Tounsi, A., Bedia, E.A., Mahmoud, S.R., Benrahou, K.H. and Tounsi, A., 2020. Stability and dynamic analyses of SW-CNT reinforced concrete

beam resting on elastic-foundation. *Computers and Concrete, An International Journal*, 25(6), pp.485-495.

[51] Zerrouki, R., Karas, A., Zidour, M., Bousahla, A.A., Tounsi, A., Bourada, F., Tounsi, A., Benrahou, K.H. and Mahmoud, S.R., 2021. Effect of nonlinear FG-CNT distribution on mechanical properties of functionally graded nano-composite beam. *Structural Engineering and Mechanics, An International Journal*, 78(2), pp.117-124.

[52] Bendenia, N., Zidour, M., Bousahla, A.A., Bourada, F., Tounsi, A., Benrahou, K.H., Bedia, E.A., Mahmoud, S.R. and Tounsi, A., 2020. Deflections, stresses and free vibration studies of FG-CNT reinforced sandwich plates resting on Pasternak elastic foundation. *Computers and Concrete, An International Journal*, 26(3), pp.213-226.

[53] Zhu, P., Lei, Z.X. and Liew, K.M., 2012. Static and free vibration analyses of carbon nanotube-reinforced composite plates using finite element method with first order shear deformation plate theory. *Composite Structures*, 94(4), pp.1450-1460.

[54] Sharma, N., Tiwari, P., Maiti, D.K., and Maity D. 2021. Free vibration analysis of functionally graded porous plate using 3-D degenerated shell element. *Composites Part C: Open Access*, 6, pp.100208.

[55] Lei, Z.X., Liew, K.M. and Yu, J.L., 2013. Buckling analysis of functionally graded carbon nanotube-reinforced composite plates using the element-free kp-Ritz method. *Composite Structures*, 98, pp.160-168.

[56] Kiani, Y., 2016. Shear buckling of FG-CNT reinforced composite plates using Chebyshev-Ritz method. *Composites Part B: Engineering*, 105, pp.176-187.

[57] Lei, Z.X., Zhang, L.W. and Liew, K., 2016. Vibration of FG-CNT reinforced composite thick quadrilateral plates resting on Pasternak foundations. *Engineering Analysis with Boundary Elements*, 64, pp.1-11.

[58] Bhagat, V., Jeyaraj, P. and Murigendrappa, S.M., 2018. Buckling and free vibration behavior of a temperature dependent FG-CNTRC cylindrical panel under thermal load. *Materials Today: Proceedings*, 5(11), pp.23682-23691.

[59] Mehar, K., Panda, S.K., Devarajan, Y. and Choubey, G., 2019. Numerical buckling analysis of graded CNT-reinforced composite sandwich shell structure under thermal loading. *Composite Structures*, 216, pp.406-414.

[60] Liu, Z., Wang, C., Duan, G., and Tan, J., 2020. Isogeometric analysis of functionally graded CNT-reinforced composite plates based on refined plate theory. *Journal of Mechanical Science and Technology,* 34*,* pp. 3687–3700.

[61] Xiang, P., Xia, Q., Jiang, L.Z., Peng, L., Yan, J.W. and Liu, X., 2021. Free vibration analysis of FG-CNTRC conical shell panels using the kernel particle Ritz element-free method. *Composite Structures*, 255, pp.112987.

[62] Gupta, A., Talha, M. and Chaudhari, V.K., 2016. Natural frequency of functionally graded plates resting on elastic foundation using finite element method. *Procedia Technology*, 23, pp.163-170.

[63] Gupta, A. and Talha, M., 2016. Nonlinear vibration response of shear deformable functionally graded plate using finite element method. *Procedia Technology*, 23, pp.201-208.

[64] Mehar, K. and Panda, S.K., 2016. Free vibration and bending behaviour of CNT reinforced composite plate using different shear deformation theory. *In IOP Conference Series: Materials Science and Engineering*, 115, pp. 012014.

[65] Mehar, K. and Panda, S.K., 2016. Geometrical nonlinear free vibration analysis of FG-CNT reinforced composite flat panel under uniform thermal field. *Composite Structures*, 143, pp.336-346.

[66] Tiwari, P., Barman, S. K., Maiti, D. K., and Maity, D. 2019. Free Vibration Analysis of Delaminated Composite Plate Using 3D Degenerated Element. *Journal of Aerospace Engineering*, 32(5), pp.04019070

[67] Farzam, A. and Kapania, R.K., 2022. Buckling analysis of functionally graded plates using Isogeometric Finite Element Method and ABAQUS. *In AIAA SCITECH 2022 Forum*, pp.1488.

[68] Wu, C.H. and Tauchert, T.R., 1980. Thermoelastic analysts of laminated plates. 2: Antisymmetric cross-ply and angle-ply laminates. *Journal of Thermal Stresses*, 3(3), pp.365-378.

[69] Reddy, J.N. and Hsu, Y.S., 1980. Effects of shear deformation and anisotropy on the thermal bending of layered composite plates. *Journal of Thermal Stresses*, 3(4), pp.475-493.

[70] Khdeir, A.A. and Reddy, J.N., 1991. Thermal stresses and deflections of cross-ply laminated plates using refined plate theories. *Journal of Thermal Stresses*, 14(4), pp.419-438.

[71] Khare, R.K., Kant, T. and Garg, A.K., 2003. Closed-form thermo-mechanical solutions of higher-order theories of cross-ply laminated shallow shells. *Composite Structures*, 59(3), pp.313-340.

[72] Zenkour, A.M., 2004. Analytical solution for bending of cross-ply laminated plates under thermo-mechanical loading. *Composite Structures*, 65(3-4), pp.367-379.

[73] Mechab, B., Mechab, I. and Benaissa, S., 2012. Analysis of thick orthotropic laminated composite plates based on higher order shear deformation theory by the new function under thermo-mechanical loading. *Composites Part B: Engineering*, 43(3), pp.1453-1458.

[74] Cetkovic, M., 2015. Thermo-mechanical bending of laminated composite and sandwich plates using layerwise displacement model. *Composite Structures*, 125, pp.388-399.

[75] Biswal, M., Sahu, S.K. and Asha, A.V., 2015. Experimental and numerical studies on free vibration of laminated composite shallow shells in hygrothermal environment. *Composite Structures*, 127, pp.165-174.

[76] Shen, H.S., 2012. Thermal buckling and postbuckling behavior of functionally graded carbon nanotube-reinforced composite cylindrical shells. *Composites Part B: Engineering*, 43(3), pp.1030-*1038*.

[77] Wang, J.F., Cao, S.H. and Zhang, W., 2021. Thermal vibration and buckling analysis of functionally graded carbon nanotube reinforced composite quadrilateral plate. *European Journal of Mechanics-A/Solids*, 85, pp.104105.

[78] Ansari, R., Torabi, J. and Shojaei, M.F., 2017. Buckling and vibration analysis of embedded functionally graded carbon nanotube-reinforced composite annular sector plates under thermal loading. *Composites Part B: Engineering*, 109, pp.197-213.

[79] Duc, N.D., Cong, P.H., Tuan, N.D., Tran, P. and Van Thanh, N., 2017. Thermal and mechanical stability of functionally graded carbon nanotubes (FG CNT)-reinforced composite truncated conical shells surrounded by the elastic foundations. *Thin-Walled Structures*, 115, pp.300-310.

[80] Chavan, S.G. and Lal, A., 2017. Dynamic bending response of SWCNT reinforced composite plates subjected to hygro-thermo-mechanical loading. *Computers and Concrete*, 20(2), pp.229-246.

[81] Biswal, M., Sahu, S.K. and Asha, A.V., 2016. Vibration of composite cylindrical shallow shells subjected to hygrothermal loading-experimental and numerical results. *Composites Part B: Engineering*, 98, pp.108-119.

[82] Patel, A., Das, R. and Sahu, S.K., 2020. Experimental and numerical study on free vibration of multiwall carbon nanotube reinforced composite plates. *International Journal of Structural Stability and Dynamics*, 20(12), p.2050129.

[83] Panda, H.S., Sahu, S.K. and Parhi, P.K., 2015. Buckling behavior of bidirectional composite flat panels with delaminations in hygrothermal field. *Acta Mechanica*, 226(6), pp.1971-1992.

[84] Biswal, M., Sahu, S.K., Asha, A.V. and Nanda, N., 2016. Hygrothermal effects on buckling of composite shell-experimental and FEM results. *Steel Compos. Struct*, 22(6), pp.1445-1463.

[85] Panda, H.S., Sahu, S.K. and Parhi, P.K., 2013. Hygrothermal effects on free vibration of delaminated woven fiber composite plates–Numerical and experimental results. *Composite Structures*, 96, pp.502-513.

[86] Rath, M.K. and Sahu, S.K., 2012. Vibration of woven fiber laminated composite plates in hygrothermal environment. *Journal of vibration and control*, 18(13), pp.1957-1970.

[87] Singh, I.V., Mishra, B.K. and Bhattacharya, S., 2011. XFEM simulation of cracks, holes and inclusions in functionally graded materials. *International Journal of Mechanics and Materials in Design*, 7(3), pp.199-218.

[88] Singh, I.V., Mishra, B.K., Bhattacharya, S. and Patil, R.U., 2012. The numerical simulation of fatigue crack growth using extended finite element method. *International Journal of Fatigue*, 36(1), pp.109-119.

[89] Bhattacharya, S., Singh, I.V., Mishra, B.K. and Bui, T.Q., 2013. Fatigue crack growth simulations of interfacial cracks in bi-layered FGMs using XFEM. *Computational Mechanics*, 52(4), pp.799-814.

[90] Bui, T.Q. and Zhang, C., 2013. Analysis of generalized dynamic intensity factors of cracked magnetoelectroelastic solids by X-FEM. *Finite Elements in Analysis and Design*, 69, pp.19-36.

[91] Kumar, S. and Bhardwaj, G., 2018. A new enrichment scheme in XFEM to model crack growth behavior in ductile materials. *Theoretical and Applied Fracture Mechanics*, 96, pp.296-307.

[92] Duhan, N., Patil, R.U., Mishra, B.K., Singh, I.V., and Pak, Y.E. 2021 Thermo-elastic analysis of edge dislocation using extended finite element method. *International Journal of Mechanical Sciences*, 192, pp. 106109.

[93] Nasirmanesh, A. and Mohammadi, S., 2015. XFEM buckling analysis of cracked composite plates. *Composite Structures*, 131, pp.333-343.

[94] Lal, A., Palekar, S.P., Mulani, S.B. and Kapania, R.K., 2017. Stochastic extended finite element implementation for fracture analysis of laminated composite plate with a central crack. *Aerospace Science and Technology*, 60, pp.131-151.

[95] Yu, T. and Bui, T.Q., 2018. Numerical simulation of 2-D weak and strong discontinuities by a novel approach based on XFEM with local mesh refinement. *Computers & Structures*, 196, pp.112-133.

[96] Li, S., Roy, S. and Unnikrishnan, V., 2018. Modeling of fracture behavior in polymer composites using concurrent multi-scale coupling approach. *Mechanics of Advanced Materials and Structures*, 25(15-16), pp.1342-1350.

[97] Sahu, S.K. and Das, P., 2020. Experimental and numerical studies on vibration of laminated composite beam with transverse multiple cracks. *Mechanical Systems and Signal Processing*, 135, p.106398.

[98] Seidel, G.D. and Lagoudas, D.C., 2006. Micromechanical analysis of the effective elastic properties of carbon nanotube reinforced composites. *Mechanics of Materials*, 38(8-10), pp.884-907.

[99] Librescu, L., Oh, S.Y. and Song, O., 2005. Thin-walled beams made of functionally graded materials and operating in a high temperature environment: Vibration and stability. *Journal of Thermal Stresses*, 28(6-7), pp.649-712.

[100] Alibeigloo, A. and Jafarian, H., 2016. Three-dimensional static and free vibration analysis of carbon nano tube reinforced composite cylindrical shell using differential quadrature method. *International Journal of Applied Mechanics*, 8(03), p.1650033.

[101] Mohammadi, S., 2008. Extended finite element method: for fracture analysis of structures. John Wiley & Sons.

[102] Negi, A., Bhardwaj, G., Saini, J.S. and Grover, N., 2019. Crack growth analysis of carbon nanotube reinforced polymer nanocomposite using extended finite element method. *Proceedings of the Institution of Mechanical Engineers, Part C: Journal of Mechanical Engineering Science*, 233(5), pp.1750-1770.

[103] Shen HS, Yang DQ. 2015. Nonlinear vibration of functionally graded fiber-reinforced composite laminated cylindrical shells in hygrothermal environments. *Applied Mathematical Modelling*. 39(5-6), pp.1480-99.

[104] Shen, H.S. and Xiang, Y., 2013. Nonlinear analysis of nanotube-reinforced composite beams resting on elastic foundations in thermal environments. *Engineering Structures*, 56, pp.698-708.

[105] Hajlaoui, A., Chebbi, E. and Dammak, F., 2019. Buckling analysis of carbon nanotube reinforced FG shells using an efficient solid-shell element based on a modified FSDT. *Thin-Walled Structures*, 144, pp.106254.

[106] Malekzadeh, P. and Shojaee, M., 2013. Buckling analysis of quadrilateral laminated plates with carbon nanotubes reinforced composite layers. *Thin-Walled Structures*, 71, pp.108-118.

[107] Zhang, L.W., Lei, Z.X. and Liew, K.M., 2015. An element-free IMLS-Ritz framework for buckling analysis of FG–CNT reinforced composite thick plates resting on Winkler foundations. *Engineering Analysis with Boundary Elements*, 58, pp.7-17.

[108] Singh, A.K. and Bhar, A., 2019. Isogeometric FE analysis of CNT-reinforced composite plates: free vibration. *SN Applied Sciences*, 1(9), pp.1010.